From interstellar matter to protoplanetary disks

古家，健次

(Degree)
博士（理学）

(Date of Degree)
2014-03-25

(Date of Publication)
2015-03-25

(Resource Type)
doctoral thesis

(Report Number)
甲第6129号

(URL)
https://hdl.handle.net/20.500.14094/D1006129

-博士学位論文-

From Interstellar Matter to Protoplanetary Disks
(星間物質から原始惑星系円盤へ)

神戸大学大学院理学研究科 地球惑星科学専攻
古家 健次

2014年1月 提出

Contents

Chapter 1

Introduction

1.1 Star formation: from clouds to disks

Interstellar space is not empty, but filled with gas and dust which are called interstellar matter or ISM. ISM is consisted of several components, distinguished by the gas density, temperature, and whether gas is mainly in ionic, atomic, or molecular form (Field et al., 1969; McKee & Ostriker, 1977; Wolfire et al., 1995). Molecular clouds are the densest ($\gtrsim 10^3$–10^5 cm^{-3}) and coldest ($\sim$10 K) components, and are made of mainly H_2 and various trace molecules. It is well-established that stars are formed in molecular clouds by the gravitational collapse.

Figure 1.1 shows astronomical objects in the sequence of low-mass star formation process. Molecular clouds have irregular and filamentary shapes with the length of $\lesssim$10 pc and the width of $\sim$0.1 pc (Figure 1.1(a)) (e.g., recent review by André et al., 2013). Inside the filaments, small ($\lesssim$0.1 pc) high-density (10^4–10^5 cm^{-3}) cores have been observed, which are probably produced by the fragmentation along filaments. While the cores can be stable against self-gravity, supported by thermal pressure, magnetic fields, and turbulence, some of them become unstable and collapse to form a star. They are called prestellar cores (Figure 1.1(b)). The lifetime of the cores is estimated to be several 10^5 yr from the statistical study (Onishi et al., 2002).

A collapsing core is initially optically thin to the thermal emission of dust grains, and undergoes isothermal run-away collapse as long as the cooling rate overwhelms the compressional heating. The isothermal condition breaks down when the central density reaches $\sim 10^{10}$ cm^{-3}, and the temperature starts rising. Increasing gas pressure decelerates the contraction, and the core comes to the hydrostatic equilibrium, which is called a first hydrostatic core (e.g., Larson, 1969; Masunaga et al., 1998). The first core has a disk-like structure with a size of $\sim$1–10 AU (e.g., Tomida et al., 2010a), since prestellar cores are rotating (e.g., Goodman et al., 1993). The first core contracts as the gas accretes from the envelope. When the temperature reaches $\sim$2000 K and hydrogen molecules start to dissociate, which is the endothermic reaction, the central region of the first core collapses again to form a protostar (e.g., Larson, 1969; Masunaga & Inutsuka, 2000). Although the first core is a transient object, it plays essential roles in determining the physical condition of a protostar; it fragments and forms binaries (Matsumoto & Hanawa, 2003), and drives bipolar molecular outflows (Tomisaka, 2002).

On the other hand, the outer part of the first core, which is supported by centrifugal force, may directly evolve to the circumstellar disk with a Keplerian rotation after the protostar birth (Machida et al., 2010). Recent high-resolution radio observations have shown that young (Class 0 or I) protostars are surrounded by gas with a Keplerian rotation (Figure 1.1(c)) (Tobin et al., 2012; Yen et al., 2013). The forming disk and central protostar evolve via the accretion from the envelope and

from the disk, respectively. The resulting disk is called protoplanetary disks, and is the formation site of planetary systems (Figure 1.1(d)). Eventually, the envelope gas dissipates.

1.2 Chemical evolution

Accompanied by the physical evolution mentioned above, molecular compositions of gas and ice change as star formation proceeds. Figure 1.2 shows schematic view of molecular evolution from molecular clouds to forming disks (Herbst & van Dishoeck, 2009; Visser et al., 2009). In molecular clouds, where the intensity of interstellar UV is low, atomic or ionic species are converted to simple molecules, such as CO and water. CO is mainly formed via gas phase reactions triggered by cosmic-ray ionization of H_2, while water is mainly formed via grain surface reactions and is a main component of ice mantles of dust grains (Herbst & Klemperer, 1973; Tielens & Hagen, 1982; Whittet, 1993; Ioppolo et al., 2008). In prestellar cores with high gas density ($\gtrsim 10^5$ cm^{-3}) and low dust temperature ($\lesssim$10 K), molecules with heavy elements in the gas phase efficiently adsorb onto dust grains. This makes additional CO-rich components to ice mantles (step 0 in Figure 1.2) (Watanabe et al., 2004; Fuchs et al., 2009).

The gravitational collapse of prestellar cores forms protostars. A central protostar warms up the surrounding gases, and icy species desorb to the gas phase at their sublimation radii (e.g., Aikawa et al., 2008). CO is one of the most volatile species, and sublimates at the outer radii where dust temperature is $\sim$20 K. On the other hand, at this lukewarm temperature, formation of complex organic molecules may efficiently occur in the ice (Garrod & Herbst, 2006; Öberg et al., 2009c) (step 1 in Figure 1.2). In the inner envelopes, where dust temperature is greater than $\sim$100 K, the bulk of ice mantles (i.e., water) sublimates (step 2 in Figure 1.2). The sublimation of ices enriches gas compositions with saturated molecules, such as water and complex organic molecules, which has been observed as hot cores/corinos (Nummelin et al., 2000; Cazaux et al., 2003).

Most envelope materials are incorporated into the disk before being accreted onto the central star. In the disk midplane, where temperature is lower than in the envelope, volatile species adsorb onto dust grains again (e.g., Visser et al., 2009). These ices may be building blocks of planets.

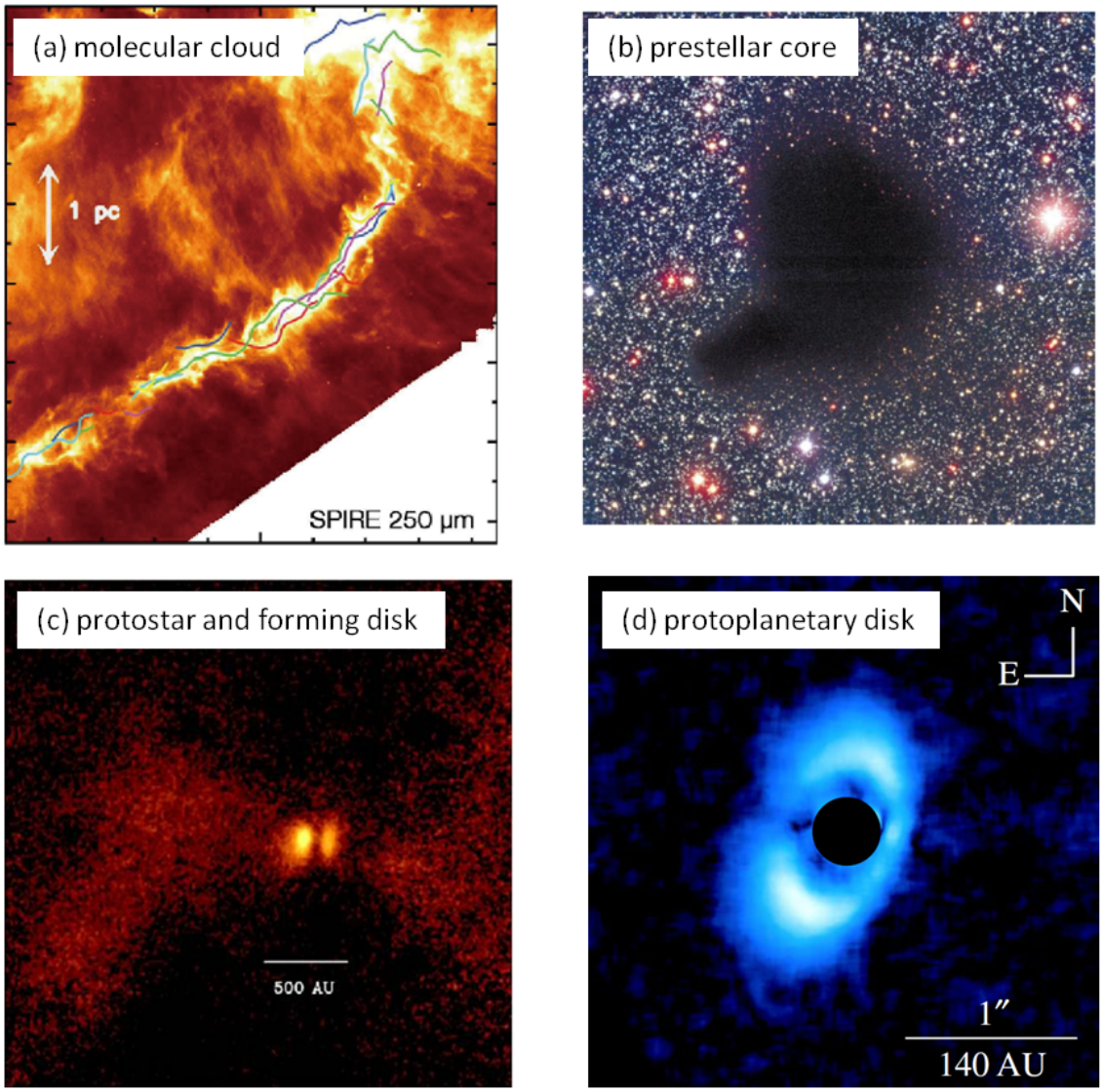

Figure 1.1: Astronomical objects in the sequence of low-mass star formation process. (a) *Herschel*/SPIRE 250 μm image of the B211/B213/L1495 region in Taurus molecular cloud, taken from Palmeirim et al. (2013). (b) Visible and near-infrared view of Barnard 68 isolated prestellar core, taken from Alves et al. (2001). (c) Gemini L'-band image of L1527 low-mass protostar and the forming disk, showing the scattered light from the outflow cavity. The figure is from Tobin et al. (2013). (d) H-band polarized intensity image of the circumstellar disk around the weak-lined T Tauri star PDS 70, using HiCIAO on the Subaru Telescope. The figure is from Hashimoto et al. (2012).

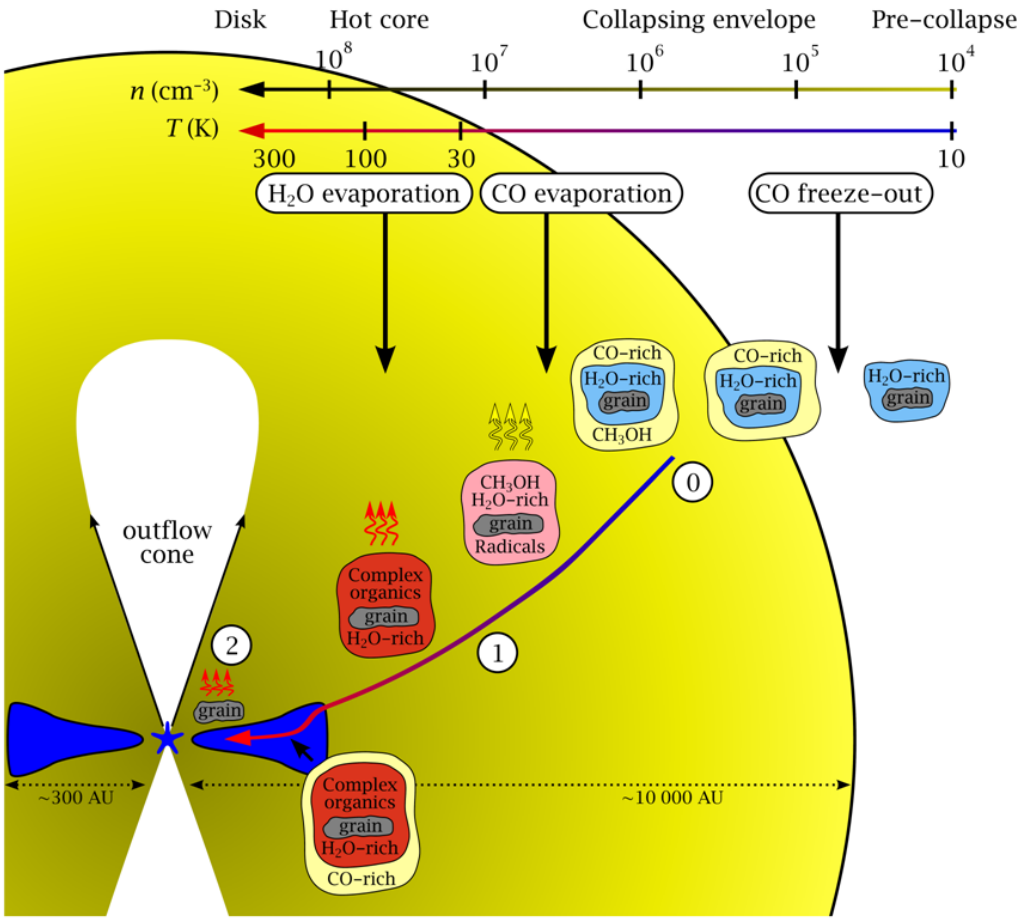

Figure 1.2: Schematic view of molecular evolution from molecular clouds to forming disks. The figure is taken from Herbst & van Dishoeck (2009) and Visser et al. (2009).

1.3 Outline of this thesis

One of the most intriguing questions in the studies of astrochemistry is whether and how much of the pristine materials in the solar nebula were inherited from the parent molecular cloud. Comets are thought to be the most pristine objects of the cold ice-bearing regions in the solar nebula (e.g., Brownlee, 2003). Many molecules have been detected in cometary coma by both ground-based and space-based observations, and their abundances with respect to water have been derived (Mumma & Charnley, 2011, and reference therein). All molecules detected in comets have also been detected in prestellar cores or protostellar envelopes. This similarity of chemical composition suggests that cometary molecules could originate from the cloud/core phase. More quantitative studies, however, shows that comets are depleted in carbon-bearing molecules and nitrogen bearing molecules compared to the median compositions of ices in low-mass protostellar envelopes (e.g., Öberg et al., 2011). It is also known that HDO/H_2O ratio in comets is lower than that in the inner envelopes ($T > 100$ K) of low-mass protostars where interstellar water ice is sublimated (e.g., Taquet et al. 2013, but see also Persson et al. 2013). These differences in abundances and isotope ratios imply that some reprocessing of chemical components could have occurred in the solar nebula.

The central theme of this thesis is twofold:

1. Whether and what fraction of chemical components established in molecular clouds/cores are preserved during the collapse phase (Chapter 2).

2. How the chemical components evolves in turbulent protoplanetary disks (Chapters 3 and 4).

In Chapter 2, we study the chemical evolution from prestellar cores to the first hydrostatic cores. Efficiencies of chemical reactions depend on various physical quantities, especially for temperature. Since the time scale of chemistry is, in general, longer than the dynamical time scale, e.g., free-fall time scale, molecular evolution depends on the past thermal history of the system, as well as on the present physical conditions. Then, coupling of radiation hydrodynamic simulations and astrochemical modelings is essential. We combine a detailed gas-grain chemical reaction network model with the three-dimensional radiation hydrodynamic simulations (Tomida et al., 2010a) of collapsing cores. One of the conclusions of this chapter is that ice compositions established in cold cloud cores are well preserved during the collapse phase.

In Chapters 3 and 4, we study ice chemistry in turbulent protoplanetary disks. Most previous models of disk chemistry have not considered the turbulent mixing.

As shown in these chapters, the combination of upward transport of ices to the disk atmosphere and transport of sublimated photodissociated species back to the deeper disk layers leads to destruction and reformation of ices. This strongly contrasts with disk models without turbulence, where most of the ices survive for $> 10^6$ yr, because they are mainly in the midplane, shielded from stellar UV and X-ray. To mimic turbulent mixing in a vertical direction, we solve chemical rate equations with the diffusion term. Our results suggest that chemical characteristic of comets, the lower HDO/H_2O ratio and the lower abundances of carbon and nitrogen-bearing molecules than the molecular cloud ices, could be established in the solar nebula via the destruction and reformation of the ices. Water chemistry and the HDO/H_2O ratio are investigated in Chapter 3, while carbon and nitrogen chemistry is studied in Chapter 4.

Chapter 2

Chemical evolution from molecular cloud cores to first hydrostatic cores

[1] *The content of this chapter is based on:*
Furuya, K. et al. 2012, ApJ, 758, 86

[1]The content of this chapter is an author-created, un-copyedited version of an article published in The Astronomical Journal. IOP Publishing Ltd is not responsible for any errors or omissions in this version of the manuscript or any version derived from it. The Version of Record is available online at http://iopscience.iop.org/0004-637X/758/2/86.

Abstract

We investigate molecular evolution from a molecular cloud core to a first hydrostatic core in three spatial dimensions. We perform a radiation hydrodynamic simulation in order to trace fluid parcels, in which molecular evolution is investigated, using a gas-phase and grain-surface chemical reaction network. We derive spatial distributions of molecular abundances and column densities in the core harboring the first core. We find that the total of gas and ice abundances of many species in a cold era (10 K) remain unaltered until the temperature reaches $\sim$500 K. The gas abundances in the warm envelope and the outer layer of the first core ($T \lesssim 500$ K) are mainly determined via the sublimation of ice-mantle species. Above 500 K, the abundant molecules, such as H_2CO, start to be destroyed, and simple molecules, such as CO, H_2O and N_2 are reformed. On the other hand, some molecules are effectively formed at high temperature; carbon-chains, such as C_2H_2 and cyanopolyynes, are formed at the temperature of >700 K. We also find that large organic molecules, such as CH_3OH and $HCOOCH_3$, are associated with the first core ($r \lesssim 10$ AU). Although the abundances of these molecules in the first core stage are comparable or less than in the protostellar stage (hot corino), reflecting the lower luminosity of the central object, their column densities in our model are comparable to the observed values toward the prototypical hot corino, IRAS 16293-2422. We propose that these large organic molecules can be good tracers of the first cores.

2.1 Background

Star formation processes include both the structure evolution as mentioned above and molecular evolution. Rates of chemical reactions depend on various physical quantities. Among them, the temperature is crucial; e.g., rates of ice sublimation and reactions with potential barriers are proportional to $\exp(-\Delta E/kT)$, where ΔE represents desorption energy or a height of an energy barrier. In addition, the molecular evolution in star forming regions is a non-equilibrium process. Therefore, accurate temperature determination via radiation hydrodynamic (RHD) simulations is important to investigate molecular evolution in star forming cores.

There are a few previous works which combined a chemical reaction network model with a RHD model of star-forming cores. Aikawa et al. (2008, here after AW08) investigated chemistry from a molecular cloud core to a protostellar core adopting a spherically symmetric RHD model (Masunaga & Inutsuka, 2000), and mainly discussed the molecular evolution that occurs at $r \gtrsim 10$ AU, where $T \lesssim 300$ K. The spherical symmetry, however, should brake down inside the centrifugal radius of $\sim$100 AU, where circumstellar disks will appear. van Weeren et al. (2009) adopted an axis symmetric RHD model (Yorke & Bodenheimer, 1999), and investigated molecular evolution mainly at $T < 100$ K from a collapsing molecular cloud cores to a forming circumstellar disk. The spatial resolution of their physical model is $\sim$3 AU in the central region. So the central first core and/or protostar is not resolved.

In this chapter, we combine a detailed chemical reaction network model of gas-phase and grain-surface chemistry with a three dimensional RHD simulation of a star-forming core for the first time, and investigate molecular evolution at $T = 10$–2000 K. So far, a few groups have succcessfully performed three-dimensional R(M)HD simulations of a low mass star-forming core up to the first core stage (Whitehouse & Bate, 2006; Commerçon et al., 2010; Tomida et al., 2010a,b). On the other hand, evolution beyond first cores in three dimension is more challenging and investigated only very recently by Bate (2010, 2011), Tomida et al. (2013), and Bate et al. (2014). So we focus on chemistry in the first core stage in the present work. Our motivations are twofold.

Firstly, first cores are good targets for Atacama Large Millimeter/submillimeter Array (ALMA). Although over 40 years have passed since Larson (1969) predicted the presence of first cores, they have not yet been detected. Observation of first cores is challenging; they are buried in dense envelopes, and have very compact structure ($\sim$10 AU) and short lifetime (a few 1000 yr). Recently, some candidates have been reported: IRS2E in L1448 (Chen et al., 2010), Per-Bolo 58 (Enoch et al., 2010) and L1541-mm (Pineda et al., 2011). Observational properties of these objects,

low bolometric luminosity $L < 0.1\ L_{\odot}$ and cold spectral energy distribution, are consistent with the theoretical predictions of first cores (e.g., Masunaga et al., 1998; Saigo & Tomisaka, 2011). On the other hand, IRS2E has a high velocity outflow ($\sim$25 km/s), and Per-Bolo 58 is considerably luminous at 24 μm and associated with a well-collimated outflow (Dunham et al., 2011), which contradict the theoretical prediction that the outflow from first cores is slow ($\lesssim$5 km/s) and not well collimated (Machida et al., 2008). Confirmation and further investigations of the candidates require observation of molecular emission lines. Therefore, chemical models of first cores are highly desired.

Secondly, recent hydrodynamic simulations have shown that the outer region of first cores might directly evolve to circumstellar disks, while the central region collapses to form protostars (Saigo et al., 2008; Machida et al., 2010, 2011; Bate, 2010, 2011). In that case, the chemical composition of the first cores would be the initial composition of the circumstellar disks. The Molecular evolution during the formation and evolution of the circumstellar disks is still an open question. Although most chemical models of the circumstellar disks have used abundances of the molecular cloud cores as initial abundances, its validity is questioned (van Weeren et al., 2009; Visser et al., 2011). In other words, there remains a missing link between chemistry in the molecular cloud cores and the circumstellar disks. Our detailed three-dimensional chemical-hydrodynamical model from the molecular cloud cores to the first cores is the first step to fill the gap.

The rest of the chapter is organized as follows. Firstly, we briefly describe our RHD simulations (Section 2.2) and chemical reaction network model (Section 2.3). In Section 2.4, we discuss trajectories of fluid parcels in our RHD simulations. We show molecular evolutions in the assorted fluid parcels, and the spatial distributions of molecular abundances in the first core stage. In Section 2.5, we discuss molecular column densities and uncertainties in our reaction network model. We compare our model with models of hot corinos in terms of physical and chemical properties. We also discuss the effect of accretion shocks on chemistry, and chemistry after the first core stage. We summarize our results in Section 2.6.

2.2 Physical model: a 3 dimensional radiation hydrodynamic simulation

Physical structure of a collapsing molecular cloud core is calculated using a three-dimensional nested-grid self-gravitational radiation magnetohydrodynamics code, which was developed by Tomida et al. (2010a). Here we briefly describe physical parameters and structure of a core.

The self-gravitational magnetohydrodynamics equations are coupled with radiation transfer, which is treated with gray flux-limited diffusion approximation (Levermore & Pomraning, 1981). The gas temperature is set to be equal to the dust temperature. In the present work, the magnetic field is set to zero for simplicity. Idealized equation of state is assumed with the adiabatic index of 5/3. The simulation consists of multiple nested-grids in order to achieve higher resolution in the central region. Each level of the nested grids has 64^3 cubic cells in (x, y, z). At the end of the simulation, 13 levels of nested-grids are generated and the smallest scale corresponds to $\sim$0.05 AU.

We calculate the evolution of a molecular cloud core with the mass of 1 $M_\odot$. The initial density distribution is given by a critical Bonnor-Ebert sphere, and enhanced by a factor of 1.6 so that the sphere becomes gravitationally unstable. Initially, the central number density of the core is $n_c \sim 8.3 \times 10^5$ cm^{-3} ($\rho_c = 3.2 \times 10^{-18}$ g cm^{-3}). The radius of the cloud core is 6300 AU. The initial angular velocity is 2.0×10^{-14} s^{-1}, and the initial temperature is set to 10 K. The simulation is stopped when the maximum temperature reaches 2000 K, at which temperature hydrogen molecules collisionally dissociate, and the second collapse starts.

In this paper, we define the moment when the central gas number density of the core reaches $n_c \sim 2.6 \times 10^{10}$ cm^{-3} ($\rho_c = 10^{-13}$ g cm^{-3}) as $t_{FC} = 0$; the first core is born. Figure 2.1 shows the temporal variations of the central gas number density and temperature of the core at $t_{FC} > 0$. The temperature and the density increase by two and five orders of magnitude in $\sim$3000 yr, respectively, which is the lifetime of the first core in our model. Figure 2.2 shows the core structures at $t_{FC} = 1500$ yr (middle stage) and 2800 yr (late stage). We present molecular distributions in these two stages in Section 2.4. The core is oblate or disk-like because of the rotation. In the panels (c) and (f), the dashed lines depict temperature contours of 25 K and 100 K, which are roughly the sublimation temperature of CO and large organic molecules, respectively. As the core evolves from 1500 yr to 2800 yr, the sublimation radii of CO and large organic molecules expand from $\sim$40 AU to $\sim$100 AU and from $\sim$5 AU to $\sim$10 AU, respectively. We discuss the physical structures of the core in more detail in Section 2.4.

Chemical processes are not included in the hydrodynamic simulation. In this work we calculate molecular abundances as a post process; we trace 10^5 fluid parcels in the hydrodynamic simulation, and calculate a chemical reaction network model along 10^4 selected trajectories. Our approach is similar to AW08 and van Weeren et al. (2009). Initially, the fluid parcels are distributed spherically at $r = 1000$–2500 AU. The parcels follow the local flow at each hydrodynamic time step. Leapfrog integration is used for tracing the parcels, and the physical parameters at the position of the parcels are obtained by the trilinear interpolation. In the calculations of molecular

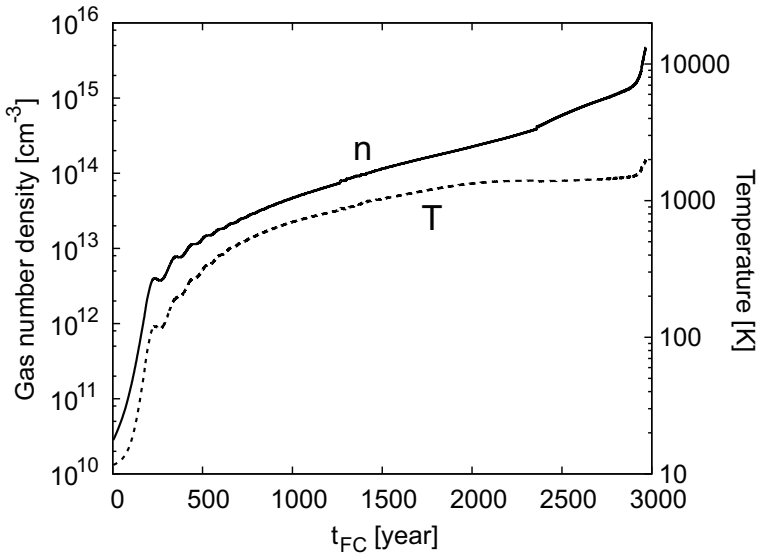

Figure 2.1: Temporal variations of gas number density (solid line) and temperature (dashed line) at the center of the core.

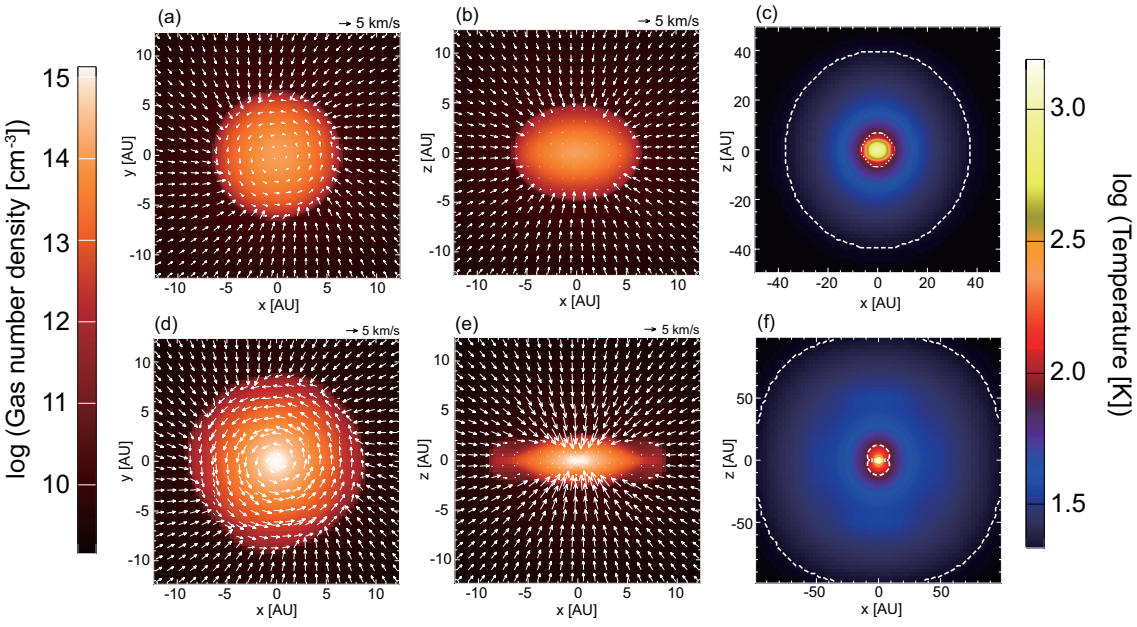

Figure 2.2: Distributions of gas number density (a, b, d, e) and temperature (c, f) at $t_{\rm FC} = 1500$ yr (a–c) and 2800 yr (d–f). The panels (a) and (d) represent the cross sections at $z = 0$, while the other panels represent the cross sections at $y = 0$. The arrows denote the velocity fields. The white dashed lines in the panels (c) and (f) depict isothermal lines of 25 K and 100 K.

evolution in the fluid parcels, the temperature, density, visual extinction, and cosmic-ray ionization rate are updated at each time step along the trajectories (see also Section 2.3.4). We note that the accretion shock heating layer at the first core surface is not spatially resolved in our model, since the thickness of the layer, $\sim 10^{-3}$ AU (Saigo & Tomisaka, 2011), is smaller than the smallest scale of our calculation. Effect of the shock layer on chemistry is discussed in Section 2.5.4.

2.3 Chemical reaction network

The dynamical evolution covers a wide range of temperature and density: 10–2000 K and 10^5–10^{16} cm^{-3} (see Figure 2.1). To calculate the molecular evolution in these physical conditions, we combine two chemical reaction network models, Garrod & Herbst (2006) and Harada et al. (2010), as a base of our model. The former is a gas-grain reaction network model applied to a star-forming core at 10–200 K. The latter is a high temperature gas-phase reaction network model, and originally developed for the temperature of 100–800 K. The major difference between the two network models is that reactions with a high potential energy barrier are included in the latter model. For the neutral-neutral reactions and neutral-ion reactions, we switch the rates from the former network to the latter network when the temperature exceeds 100 K. In the following, we describe modifications to gas phase reactions, treatment of gas-grain interactions, and grain-surface reactions in our model. In total, the reaction network consists of 461 gas-phase species (including dust grains with three different charge states) and 195 grain-surface species, and 11696 reactions. The numerical code for solving rate equations is adapted from Nautilus (Hersant et al., 2009; Semenov et al., 2010).

2.3.1 Modifications to gas phase reactions

Firstly, we modify branching ratios of dissociative recombination reactions. Geppert et al. (2006) suggested that formation of saturated complex molecules by dissociative recombination of their protonated precursors is not efficient. For example, when protonated methanol ($CH_3OH_2^+$) recombines, the branching ratio for CH_3OH + H is only 3%. Recently, Hamberg et al. (2010) also showed that in dissociative recombination of dimethyl ether cation ($CH_3OCH_4^+$), the branching ratio for CH_3OCH_3 + H is only 7%. Referring to these experiments, the network of Garrod et al. (2008), which is an extension of Garrod & Herbst (2006) to more complex species, assumed that two-fragment channels (ex. $X^+ + e^- \rightarrow Y + Z$) represent 5% each, and that the remainder is evenly split between channels with three or more fragments, while in the network of Garrod & Herbst (2006) the branching ratios of dissociative reactions of

protonated complex molecules are equally weighted for most species. We modify the branching ratios in the recombination of protonated precursors of saturated complex molecules following Garrod et al. (2008).

We add some three-body association reactions and collisional dissociation reactions for all neutral species to our network referring to Willacy et al. (1998) (see Appendix A). Collisional dissociation of H_2 is an exception; we use the rates in Harada et al. (2010) instead of Willacy et al. (1998). Since collisional dissociation is endothermic, the rate of the collisional dissociation reactions is proportional to $\exp(-\gamma/T)$. The energy barrier, γ, must be larger than ΔH, which is the difference between the formation enthalpy of products and reactants. In Willacy et al. (1998) the value of γ is set to be lower than ΔH for some reactions. For those reactions, we calculate ΔH at 300 K referring to NIST-JANAF Thermochemical Tables (http://kinetics.nist.gov/janaf/) and KInetic Database for Astrochemistry (KIDA; http://kida.obs.u-bordeaux1.fr; Wakelam et al. 2012), and replace γ with ΔH. For the species which are not listed in the network of Willacy et al. (1998) the collisional dissociation rates are set to be,

$$k_{cd} = 1.0 \times 10^{-10} \exp(-\Delta H/T). \tag{2.1}$$

If the formation enthalpy of reactants or products are not available in the literature, we assume ΔH is 5×10^4 K ($\sim$5 eV). We assume that the collisional dissociation reactions preserve functional groups. Otherwise, we assume that one H atom is extracted via the collisional dissociation. It should be noted that the set of collisional dissociation reactions in our model is likely incomplete because of the lack of experimental data; for many reactions listed in Table A.2, there is no laboratory experiments in which products are confirmed. If the products are different from those listed in Table A.2, the value of γ should also be different. In Section 2.5.2, we discuss how the molecular abundances depend on the assumption on the collisional dissociations.

2.3.2 Gas-grain interactions

In molecular cloud cores, dust grains are negatively charged. But the population of charged particles changes as the gas density increases (Umebayashi, 1983). Grains become the dominant charged particles at high densities ($n \gtrsim 10^{10}$ cm^{-3}), and eventually grain-surface recombination (ion-grain collision) overwhelms gas-phase recombination (recombination of an free electron with an ion). Grain charges should therefore be calculated in the network simultaneously.

We consider neutral and singly charged dust grains. Gaseous species and dust grains interact through electron-grain, ion-grain collisions and adsorption and desorp-

Table 2.1: Generalized reaction scheme of gas-grain interactions. X, Y, and Z are neutral gaseous species whose charges are denoted by their indices, and gr are grain particles. X ice represents the species on grain surfaces.

Grain-grain	gr^-	+	gr^+	$\rightarrow$	gr	+	gr		
Electron-grain	e^-	+	gr	$\rightarrow$	gr^-				
	e^-	+	gr^+	$\rightarrow$	gr				
Cation-grain	X^+	+	gr^-	$\rightarrow$	Y	+	Z	+	gr
	X^+	+	gr	$\rightarrow$	Y	+	Z	+	gr^+
Anion-grain	X^-	+	gr^+	$\rightarrow$	X	+	gr		
Adsorption	X	+	gr^-	$\rightarrow$	X ice	+	gr^-		
	X	+	gr	$\rightarrow$	X ice	+	gr		
	X	+	gr^+	$\rightarrow$	X ice	+	gr^+		
Desorption	X ice			$\rightarrow$	X				

tion of neutral species. Table 2.1 lists the generalized scheme of gas-grain interactions in our model.

A collision between a negatively-charged grain and a positively-charged grain result in two neutral grains. The collision rate of a grain of radius a and charge le with another grain of radius a' and charge $l'e$ is given by

$$k_{gg} = \pi(a+a')^2 \left(\frac{8kT}{\pi\mu_g}\right)^{1/2} \left[1 - \frac{ll'e^2}{(a+a')kT}\right], \tag{2.2}$$

where μ_g is the reduced mass of the colliding grains (Umebayashi, 1983). We simply assume all grains have the same radius of 10^{-5} cm and density of 3 g cm^{-3}. In the case of electron-grain collisions, the rates are given by

$$k_{eg} = S_e \pi a^2 \left(\frac{8kT}{\pi m_e}\right)^{1/2} \tilde{J}\left(\tau = \frac{akT}{e^2}, \nu = -l\right), \tag{2.3}$$

where m_e is the mass of electron. An electron sticks to a grain upon collision with a sticking probability of S_e, which strongly depends on the temperature. We calculate S_e following Umebayashi (1983), assuming a potential depth of the grain equals to 2 eV. $\tilde{J}$ is a dimensionless reduced rate coefficient including the polarization effect of the grains by the electric field of approaching species. We applied the approximate formulas given by Draine & Sutin (1987),

$$\tilde{J}(\tau, \nu = 0) = 1 + \left(\frac{\pi}{2\tau}\right)^{1/2}, \tag{2.4}$$

$$\tilde{J}(\tau, \nu < 0) = \left[1 - \frac{\nu}{\tau}\right] \left[1 + \left(\frac{2}{\tau - 2\nu}\right)^{1/2}\right]. \tag{2.5}$$

The collision of a cation with a negatively charged grain is theoretically discussed in Watson & Salpeter (1972), and summarized by Umebayashi & Nakano (1980). According to these references, there are two possible processes when a cation approaches a negatively charged grain; a free electron tunnels to the cation before it hits the grain, or the recombination occurs on the grain surface. For simplicity, we assume the former case, in which the products and branching ratios of the recombination would be the same as the recombination in the gas phase. In the case of the collision of a cation with a neutral grain, recombination probably occurs on grain surfaces, and the products desorb to the gas phase, using the excess energy (T. Umebayashi 2012, private communication). Again, we assume that the products and branching ratios are the same as the corresponding recombination in the gas phase, for simplicity, although they might be different. For example, if $X^+ + e^- \rightarrow Y + Z$ in gas-phase recombination, corresponding grain-surface recombinations are

$$X^+ + gr^- \rightarrow Y + Z + gr, \tag{2.6}$$

$$X^+ + gr \rightarrow Y + Z + gr^+. \tag{2.7}$$

Our network includes recombination in the gas phase and on grain surfaces for all cations. Since we assume that each branching ratio for two fragment channels is only 5%, our approach tends to produce smaller molecules via the dissociation of large species. If we assume that, for example, the branching ratios for all product channels are equal or the collisions lead to simple charge exchange (ex. $X^+ + gr^- \rightarrow X + gr$), formation rates of large organic species are enhanced. In other words, our model gives the lower limit of the abundances of large organic species. We discuss how much the abundances of large organic molecules are enhanced if we assume the equally weighted branching ratios for grain surface recombination in Section 2.5.2.

Recently, anions have been detected toward both the prestellar core, TMC-1 (Brünken et al., 2007), and the protostellar core, L1527 (Sakai et al., 2007; Agúndez et al., 2008). Our network includes H^-, C^-, O^-, S^-, CN^-, and OH^-. Since interaction between anions and grains are unclear, we assume simple charge exchange,

$$X^- + gr^+ \rightarrow X + gr. \tag{2.8}$$

The rates of grain-ion (both cation and anion) collisions are expressed as

$$k_{jg} = \pi a^2 \left(\frac{8kT}{\pi m_j}\right)^{1/2} \tilde{J}\left(\tau = \frac{akT}{q_j^2}, \nu = \frac{le}{q_j}\right), \tag{2.9}$$

where m_j and q_j are the mass and the charge of ions, respectively.

Gaseous neutral species collide with dust grains and stick to the grain surface. AW08 and van Weeren et al. (2009) assumed sticking probabilities of 0.5 and unity, respectively, independent of the temperature. Since the sticking probability should be lower at higher temperatures, we assume that the sticking probability for neutral species is

$$S_n = [1 + 0.04(T + T_{\rm d})^{0.5} + 2 \times 10^{-3} T + 8 \times 10^{-6} T^2]^{-1}, \tag{2.10}$$

where T and $T_{\rm d}$ are the gas and dust temperatures, respectively. We assume that T and $T_{\rm d}$ are the same. Although Equation (2.10) is originally derived for the sticking probability of a H atom (Hollenbach & Mckee, 1979) by fitting the numerical calculations, we use it for all neutral species. For example, the value of S_n is 0.83 at 10 K and 0.54 at 100 K. We might underestimate S_n, because a loss of kinetic energy would be larger for collisions of heavier species with grains.

After species are adsorbed onto grain surfaces, they can desorb to the gas phase again. We adopt the same desorption energies as Garrod & Herbst (2006), in which grain-surfaces are assumed to be covered with H_2O ice. In addition to the thermal desorption, we consider two non-thermal desorption processes. One is the cosmic-ray induced desorption; grains are heated up to 70 K by the cosmic-ray bombardment, and it allows temporal evaporations of species with low binding energies (Hasegawa & Herbst, 1993). The other is the chemical desorption; energy released by the exothermic grain-surface reactions is used to desorb the products. The efficiency of the desorption is parameterized by $a_{\rm RKK}$, which is the ratio between the surface-molecule bond frequency and the frequency at which the energy is lost to the surface. We assume $a_{\rm RKK} = 0.01$ referring to Garrod et al. (2007); roughly 1% of the products are desorbed into the gas phase.

2.3.3 Grain surface reactions

Calculation of grain-surface chemistry is performed in a similar way to Garrod & Herbst (2006). The diffusion energy barrier is set to be a half of the desorption energy of each species. The diffusion rate is exponentially dependent on the diffusion barrier divided by the grain temperature, and surface reaction rates are determined by the sum of the diffusion rates for two reaction partners (Hasegawa et al., 1992). If surface reactions have activation energy barriers, the barriers are overcome thermally, or via quantum tunneling, whichever is faster. The modified rate method (Caselli et al., 1998) is used only for reactions involving atomic hydrogen. Our model also includes photodissociation on grain surfaces by interstellar and cosmic-ray induced UV photons.

Our model assumes that molecules are physorbed, which is appropriate as long as

grain surfaces are covered with ice. At $T \gtrsim 150$ K, however, ice mantle is sublimated, and chemisorption might become important (e.g., Section 4.2.2 of Tielens, 2005). Since grain-surface reactions via chemisorption is out of the scope of this paper, we switch off adsorption of neutral gas-phase species onto grain surfaces, desorption of ice-mantle species to the gas phase, and grain surface reactions, if the temperature becomes greater than 200 K.

2.3.4 Initial molecular abundances and ionization rates

Table 2.2 lists the initial abundances in our model. The elemental abundances adopted here are called "low metal" values because of their strong depletions of species heavier than oxygen (e.g., Graedel et al., 1982). Species are initially assumed to be atoms or atomic ions except for hydrogen, which is in molecular form. We integrate the initial abundances for 10^5 yr with the typical conditions of dense molecular cores, $T = 10$ K, $n_{\rm H} = 1 \times 10^4$ cm^{-3} and visual extinction of $A_V = 10$ mag, which determine the abundances of our initial Bonnor-Ebert like sphere. Before the collapse begins, we further integrate the updated abundances under the initial hydrostatic conditions during 1.6×10^5 yr (i.e., sound crossing time of our core model), in order to obtain the starting abundances for the collapse, implicitly assuming that the core keeps its initial hydrostatic structure supported by turbulence. Our approach is similar to AW08 and van Weeren et al. (2009).

Table 2.2: Initial abundances relative to hydrogen nuclei.

Species	Abundance
H_2	5.00(-1)
H	5.00(-5)
He	9.75(-2)
C^+	7.86(-5)
N	2.47(-5)
O	1.80(-4)
Si^+	2.74(-9)
S^+	9.14(-8)
Fe^+	2.74(-9)
Na^+	2.25(-9)
Mg^+	1.09(-8)
Cl^+	1.00(-9)
P^+	2.16(-10)

In the hydrodynamic simulation, we calculate column densities of gas in the $x-$, $y-$ and $z-$directions, Σ_x, Σ_y and Σ_z, from the core outer edge to a position of each

fluid parcel. We choose the minimum of Σ_x, Σ_y, Σ_z and convert it to A_V, via the formula $A_V = (f_H \Sigma/\mu m_H) \times (5.34 \times 10^{-22}\ \mathrm{cm}^2)$ mag (Bohlin et al., 1978; Cardelli et al., 1989), where f_H is the mean number of hydrogen nuclei per species (1.67), μ is the mean molecular weight (2.3) and m_H is the mass of a hydrogen atom. For the fluid parcels we follow, the initial values of A_V are greater than 10 mag, and A_V increases as the collapse proceeds. Hence the interstellar UV radiation has little effect on chemistry in our model.

Cosmic rays are the main source of ionization in molecular clouds. The cosmic-ray ionization rate of hydrogen is set to be $1.3 \times 10^{-17}\ \mathrm{s}^{-1}$. The attenuation length of cosmic-ray is 96 g cm^{-2} (Umebayashi & Nakano, 1981), which is much larger than the column density of typical molecular clouds, but can be smaller than the column density, Σ, calculated above. The decay of short-lived radio active isotopes, which releases energetic particles, also ionize the ISM with rates $\xi = (7.6\text{–}11) \times 10^{-19}\ \mathrm{s}^{-1}$ (Umebayashi & Nakano, 2009). Thus for direct cosmic-ray ionization and cosmic-ray-induced photo reactions, we assume that the effective cosmic-ray ionization rate is expressed as

$$\xi_{eff} = 1.3 \times 10^{-17} \exp\left(-\frac{\Sigma}{96\,\mathrm{g\,cm^{-2}}}\right) + 1 \times 10^{-18}. \tag{2.11}$$

In our model, the decay of radio active isotopes is the main source of ionization within the first core, while the cosmic-ray dominates at the surface of the first core and infalling envelopes.

2.4 Result

2.4.1 Physical structure of the core

Figure 2.3 shows the spatial distributions of the gas number density, radial velocity (v_r), and temperature perpendicular to (a–c) and along the rotational axis (d–f). We averaged the distributions perpendicular to the rotational axis in the $z = 0$ plane in the azimuth direction. The solid lines represent the distributions at $t_{FC} = 1500$ yr, while the dashed lines represent the distributions at $t_{FC} = 2800$ yr. We define r and R as $\sqrt{x^2 + y^2 + z^2}$ and $\sqrt{x^2 + y^2}$, respectively. Although the core has the rotation, the core structures are almost spherical at $r \gtrsim 10$ AU both in the middle and late stages. The density has a power law distribution of r^{-2} at $r \gtrsim 100$ AU and $r^{-1.5}$ at 10 AU $\lesssim r \lesssim 100$ AU. The effect of the rotation becomes apparent in the inner region ($r \lesssim 10$ AU) especially in the late stage, in which infalling gases have larger angular momentum. The accretion onto the first core is supersonic, and the

accretion shock occurs at the first core surface. The first core is quasi-hydrostatic, and in the middle stage its radius is ∼6 AU perpendicular to the rotational axis and ∼5 AU along the rotational axis, respectively, while it is ∼10 AU and ∼3 AU in the late stage.

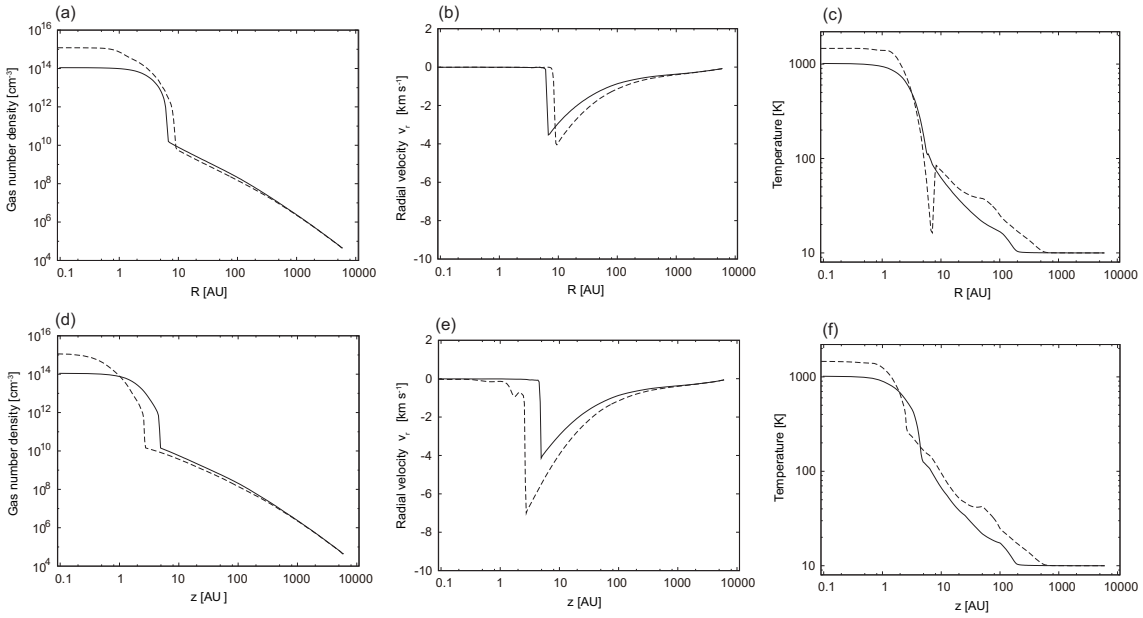

Figure 2.3: Distributions of gas number density, radial velocity (v_r) and temperature perpendicular to (a–c) and along the rotational axis (d–f) at $t_{\rm FC}$ = 1500 yr (solid lines) and 2800 yr (dashed lines). Distributions perpendicular to the rotational axis are in the $z = 0$ plane and averaged in the azimuth direction.

The temperatures both in the envelope and the first core increase with time as the first core grows, except for the low-temperature region in 5 AU $\lesssim R \lesssim$ 10 AU around the equatorial plane. This region experiences strong expansion perpendicular to the rotational axis in a dynamical timescale due to the angular momentum transport. Cooling by the expansion is more efficient than the radiation heating, since the gas is optically thick.

2.4.2 Spatial distribution of fluid parcels

Figure 2.4 shows the spatial distributions of fluid parcels in the middle (left) and late (right) stages. Each parcel is color-coded by its initial distance from the core center (above the equatorial plane) or its initial specific angular momentum (below the equatorial plane). In the middle stage, the first core is composed mainly of the fluid parcels which were initially at $r \sim$ 1150–1450 AU. In the late stage, these parcels have moved to the midplane of inner radii due to contraction, and the outer

layers of the first core is composed of parcels falling from the initial radii of $r \sim$ 1700–1850 AU. It indicates that the accretion of the envelope onto the first core is active, and the gas inside the first core is continuously compress into the center. Parcels closer to the rotational axis have smaller initial angular momentum. While parcels fall almost radially in the envelope, they move in the z direction in the first core rather than radially until they reach the equatorial plane. Near the equatorial plane, parcels move inward in the direction perpendicular to the rotational axis by losing the angular momentum.

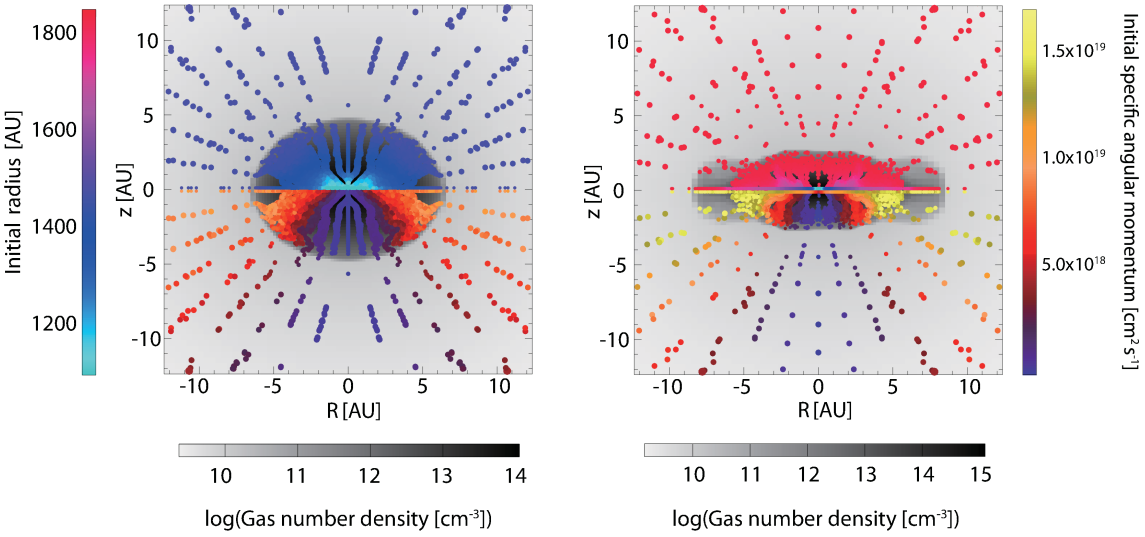

Figure 2.4: Spatial distributions of fluid parcels in the middle stage (left) and the late stage (right). The parcels are color-coded according to their initial radius (above the equatorial plane) and initial specific angular momentum (below the equatorial plane). Gray scale shows the distributions of gas number density averaged in the azimuth direction. A parcel is plotted at $(R, z) = (\sqrt{x_p^2 + y_p^2}, z_p)$, when the position of the parcel is (x_p, y_p, z_p). $R < 0$ regions are simply copied from $R > 0$ regions.

2.4.3 Molecular evolution in a single fluid parcel

Here, we show the thermal and chemical histories of a single fluid parcel, which are helpful to understand the spatial distributions of molecules presented in Section 2.4.4. Figure 2.5 shows the trajectory of the parcel, which is initially at $r = 1300$ AU and 70° degrees from the rotational axis. The first core surface (white dashed line) is defined as the isoline of the minimum gas density in the region where the local sound speed is greater than the radial velocity. Figure 2.6(a) shows the temporal variations of the position of the parcel in r, R, z. The horizontal axes is set to be $t_{\rm final} - t$, where $t_{\rm final}$ represents the final stage of our model; $t_{\rm FC} = 0$ corresponds

$t_{\rm final} - t \sim 3000$ yr. The vertical dotted lines in Figure 2.6 represent the time when the parcel passes the accretion shock at the first core surface ($t_{\rm final} - t = 1930$ yr). The parcel initially infalls almost spherically. The effect of the rotation becomes apparent inside the first core, and the trajectory becomes helical. The parcel falls to the equatorial plane within 10^2 yrs after entering the first core, while it moves inward in the direction perpendicular to the rotational axis over 10^3 yrs by losing its angular momentum.

Figure 2.6(b) shows the temporal variations of the temperature in the parcel. We classify the history of the parcel into three phases in terms of the temperature; cold phase (10–20 K), warm-up phase (20–200 K) and hot phase (>200 K). Dominant chemical processes vary among the three phases. In the cold phase, adsorption onto and hydrogenation on grain surfaces are dominant, while in the warm-up phase, the molecular evolution is caused by grain-surface reactions among species with heavy elements and evaporation of ice mantle species. In the hot phase, the molecular evolution is caused by gas phase reactions. This classification has been used in the chemistry in protostellar stage (e.g., Herbst & van Dishoeck, 2009). It should be noted, however, that in the first core stage the density is higher and the duration of the warm-up and hot phases are shorter than in protostellar stage. Table 2.3 summarizes the physical conditions and duration of the three phases in the parcel.

Table 2.3: Temperature, number density of hydrogen nuclei, position in r, and duration of the cold, warm-up, and hot phases in the fluid parcel. t_{ff} is the free-fall time of the initial central density.

	Temperature (K)	$n_{\rm H}$ (cm^{-3})	Position in r (AU)	Duration (yr)
Cold phase	10–20	1×10^6–2×10^9	1500–40	7×10^4 ($\sim 3t_{ff}$)
Warm-up phase	20–200	2×10^9–8×10^{12}	40–5	120
Hot phase	200–2000	8×10^{12}–8×10^{15}	5–<0.1	1900

In the following, we show the molecular evolution in these three phases. However, the temporal variations at 20 K $\lesssim T \lesssim$ 1000 K is difficult to see because the temperature rises in a short time scale ($\sim 10^3$ yrs). In order to zoom-up the evolution at that temperature range, each panel in Figures 2.6(c–h) is divided into three phases based on the above classification. The panels (c), (d) and (e–h) show the number density of H nuclei, temperature, and molecular abundances relative to H nuclei in the parcel, respectively. The physical conditions as well as the molecular abundances look discontinuous at the boundaries of the phases, which is due to the different scaling of the horizontal axis. We assume that the parcels stay for 1.6×10^5 yr in its initial position, as mentioned in Section 2.3.4, but this pre-collapse phase is omitted

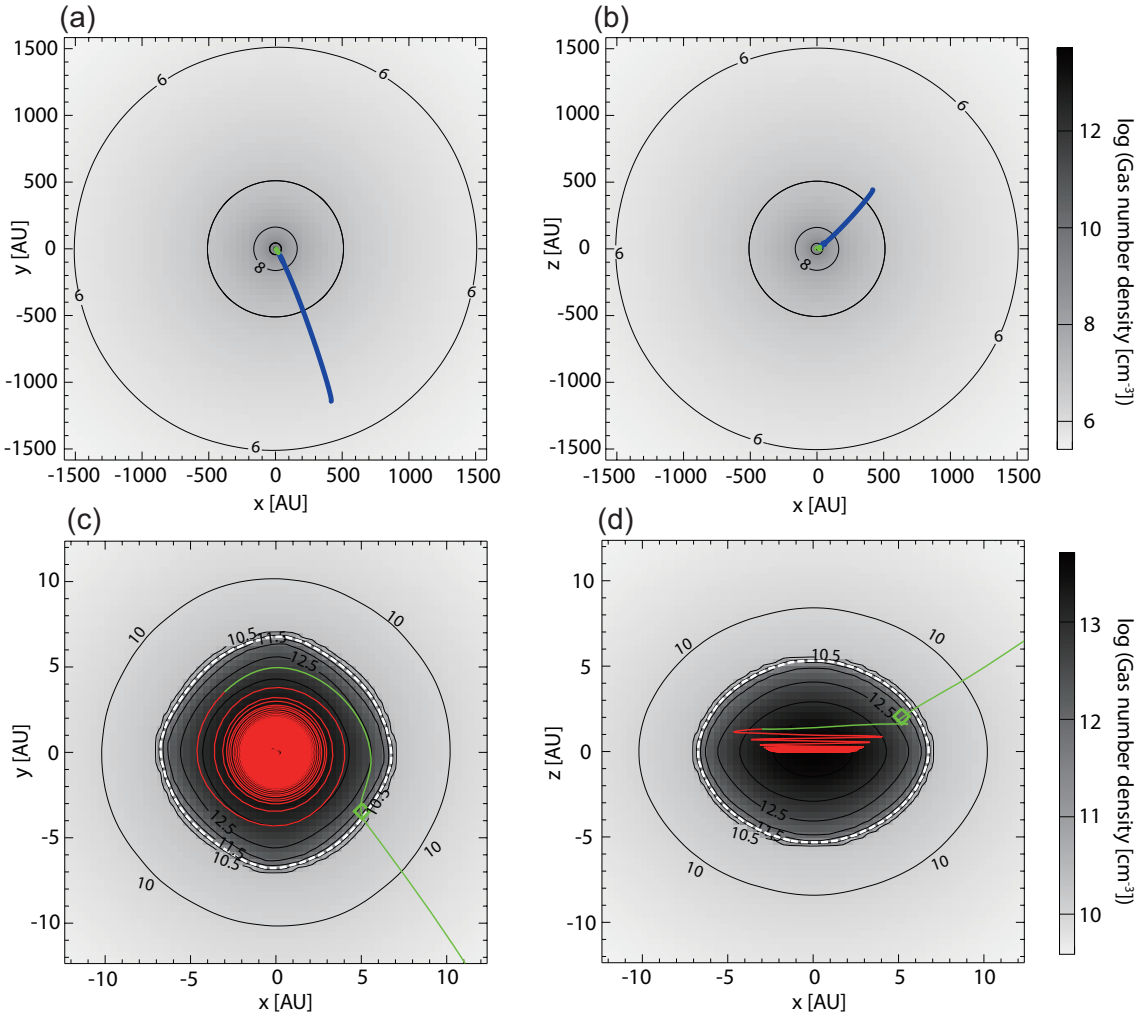

Figure 2.5: Trajectory of the fluid parcel, which is initially at 1300 AU from the center and 70° degrees from the rotational axis, plotted over the distribution of the gas number density when the parcel enters the first core (gray scales and contour lines). The values on the contour lines are number density in logarithm scale. The panels (a) and (b) show the whole trajectory, while the panels (c) and (d) are the closeup views. The trajectory is projected to the $z = 0$ plane in the panels (a) and (c), and to the $y = 0$ plane in the panels (b) and (d). The trajectory is color-coded according to the temperature in the parcel; the cold phase (10–20 K, blue), the warm-up phase (20–200 K, green) and the hot phase (>200 K, red). In the panels (c) and (d), the white dashed lines depict the first core surface, and the diamonds depict where the parcel passes the accretion shock at the first core surface.

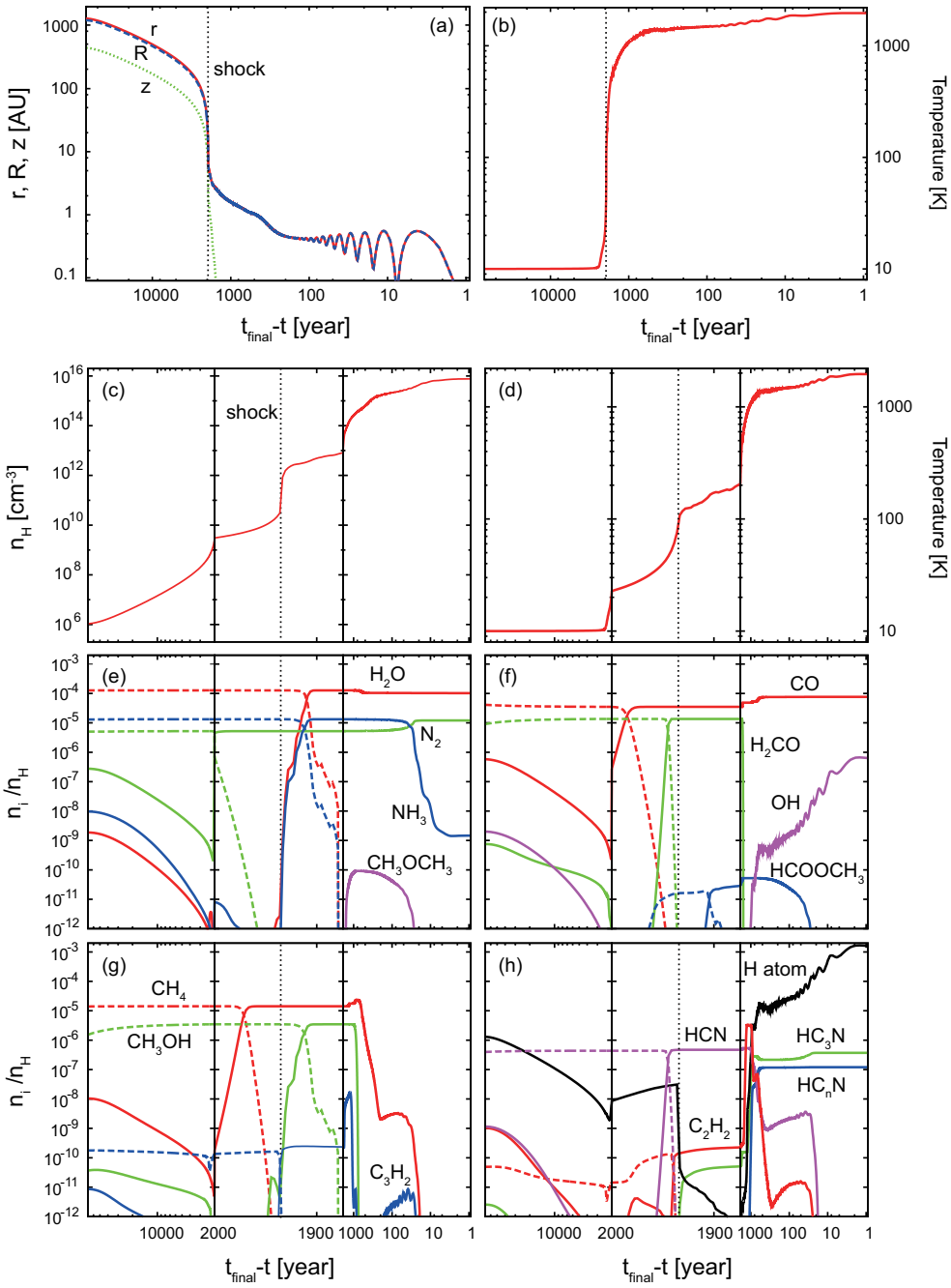

Figure 2.6: Temporal variations of the position of the parcel in r, R, z (a), temperature (b, d), number density of H nuclei (c), and molecular abundances (e–h) in the fluid parcel. The horizontal axis is the logarithm of $t_{\rm final} - t$. In order to zoom-up the warm-up phase, the panels (c–h) are divided into three phases; the cold phase ($T < 20$ K), the warm-up phase (20 K $< T <$ 200 K) and the hot phase ($T >$ 200 K). Note that the scale of the horizontal axis is different among the phases. The vertical dotted lines represent the time when the parcel passes the accretion shock at the first core surface. In the panels (c–h), the solid lines represent gas-phase species, while the dashed lines represent ice-mantle species. HC_nN indicates total molecular abundances of HC_5N, HC_7N and HC_9N.

in Figure 2.6.

Cold phase

When the core begins to contract ($t_{\rm final} - t = 7 \times 10^4$ yr), molecules with heavy elements are mostly exists on grain surfaces. The main carbon reservoirs are CO, CH_4 and H_2CO in order of high to low abundances. Water, which is formed by hydrogenation of oxygen atoms on grain surfaces, is as abundant as $\sim 10^{-4}$. The nitrogen mainly exists as N_2 and NH_3. All these molecules mostly exist on grain surfaces.

At the beginning of the contraction, the parcel migrates inward almost spherically and isothermally. As the parcel falls to inner denser regions, the abundances of gaseous molecules decrease due to freeze-out. Hydrogenation on grain surfaces occur subsequently, and the abundances of formaldehyde (H_2CO) and methanol (CH_3OH) slightly increase. At the end of the cold phase, the abundances of CH_3OH and H_2CO are 3×10^{-6} and 1×10^{-5}, respectively.

Warm-up phase

After the first core is formed, the parcel continues to infall, and the temperature in the parcel starts to rise. The parcel passes the accretion shock at the first core surface at $t_{\rm final} - t = 1930$ yr, when the number density of H nuclei is 3×10^{10} cm^{-3} and the temperature is 80 K (vertical dotted lines in Figure 2.6). Since the shock heating layer is not spatially resolved in our hydrodynamic simulation, our chemical model neglect this shock heating. We discuss the effect of the accretion shock on chemistry in Section 2.5.4.

During the warm-up phase, species are desorbed into the gas phase when the temperature reaches their sublimation temperatures. CO is desorbed to the gas phase when the temperature reaches 25 K, which is slightly higher than the typical interstellar value of 20 K, because of the higher density ($\sim 10^9$ cm^{-3}) of the envelope in the first core stage. On the other hand, species with the higher binding energies are not desorbed yet; they migrate on grain surfaces and react with each other at the lukewarm temperature of $T \sim$ several 10 K. AW08 found that large organic molecules, such as $HCOOCH_3$ and CH_3OCH_3 are efficiently formed at $T = 20$–40 K, and reach the terminal abundances of $\sim 10^{-9}$ in the protostellar core. In our model, $HCOOCH_3$ is formed at $T = 30$–50 K, but reaches abundances of only 2×10^{-11}. The abundances of formic acid (6×10^{-11}) and CH_3CN (6×10^{-9}) change little in the warm-up phase. The formation of large organic species in the warm-up phase is inefficient in our model because of the short time scale spent in the lukewarm region, which is determined by the size of the lukewarm region divided by the infalling

velocity: it is only $\sim 10^2$ yrs in our model, while it continues $\sim 10^4$ yrs in AW08 (see also Garrod & Herbst, 2006). These large organic molecules start to be desorbed at $T > 100$ K.

Hot phase

In the hot phase, ice mantles of grains are completely evaporated, and gas phase reactions determine the molecular abundances. The temperature and density of H nuclei reach 2000 K and 8×10^{15} cm^{-3}, respectively at the final step. The duration of the hot phase is $\sim 2 \times 10^3$ yrs.

At the temperature of 200–500 K, the composition stays almost the same as in the warm-up phase. At $T \gtrsim 500$ K, most molecules are destroyed, and simple molecules are reformed. For example, H_2CO starts to be destroyed by collisional dissociation when the temperature reaches $\sim$500 K. CH_3OH is also collisionally dissociate at $T \sim 1200$ K. Methane, which is the second carbon reservoir, is converted to CO by neutral-neutral reactions in several hundred yrs. As a result, the abundance of CO increases by a factor of 2. The abundance of H_2O, which is the main oxygen reservoir, remains the almost constant value of $\sim 10^{-4}$, which is mostly determined in the precollapse phase. The dominant reservoirs of the nitrogen are N_2 and NH_3. At $T \gtrsim 1600$ K, NH_3 is converted to N_2 through the reactions of $NH_3 + H \rightarrow NH_2 + H_2$, and $NH_2 + NO \rightarrow N_2 + H_2O$ on the time scale of $\sim$10 yrs. The former reaction has the potential energy barrier of 5.2×10^3 K. The abundance of hydrogen atom increases with time mainly by collisional dissociation of H_2. When the temperature reaches $\sim$2000 K, $\sim$0.1% of hydrogen nuclei is in hydrogen atom. As the abundance of hydrogen atom increases, OH is formed through the reaction, $H_2O + H \rightarrow OH + H_2$, which has the potential energy barrier of 9.7×10^3 K.

Some larger molecules are temporary formed in the gas phase. Methyl formate and CH_3OCH_3 are formed by the grain-surface recombination of $HCOOCH_4^+$ and $CH_3OCH_4^+$, respectively, despite the small branching ratio of 5%. These formation paths are efficient until CH_3OH, which is the precursor of $HCOOCH_4^+$ and $CH_3OCH_4^+$, is destroyed by collisional dissociation. The peak abundances of $HCOOCH_3$ and CH_3OCH_3 are 5×10^{-11} and 9×10^{-11}, respectively. At the temperature of $\sim$700 K, acetylene (C_2H_2) is formed by the reaction of H_2 and C_3H_4, which is formed on grain surfaces during the cold phase. The reaction has the potential barrier of 2.3×10^4 K. The abundance of C_2H_2 reaches $\sim 10^{-6}$ at the maximum. C_2H_2 is destroyed through the reactions of $C_2H_2 + OH \rightarrow CH_2CO + H$, and $CH_2CO + M \rightarrow CH_2 + CO$, where M represents the third body (mainly H_2). These reactions have the potential energy barrier of 5.0×10^3 K and 3.9×10^4 K. Other unsaturated carbon-chain molecules, C_xH_y, are temporally formed via the neutral-neutral

reactions, $C_xH_{y+1} + H \rightarrow C_xH_y + H_2$, which have the potential energy barrier of several 10^3 K. HCN is converted to HC_3N through the reactions of HCN + H $\rightarrow$ CN + H_2, and C_2H_2 + CN $\rightarrow$ HC_3N + H. The former reaction has the potential energy barrier of 1.2×10^4 K. Larger cyanopolyynes (HC_nN, $n = 5, 7, 9$) are also formed by the subsequent neutral-neutral reactions of HC_3N + C_2H, HC_5N + C_2H and HC_7N + C_2H. The terminal abundances of HC_nN ($n = 3, 5, 7, 9$) are 4×10^{-7}, 1×10^{-7}, 2×10^{-8} and 4×10^{-9}, respectively. These cyanopolyynes survive until the end of the simulation, because the neutral-neutral reactions, $C_nN + H_2 \rightarrow HC_nN + H$, which have the potential barriers of 2000 K, are compensated by the formation via the collisional dissociation reactions, $HC_nN + M \rightarrow C_nN + H + M$. Therefore, the abundances of cyanopolyynes depend on the products of the collisional dissociation reactions assumed in our model.

In summary, the total molecular abundances (gas and ice combined) of many species in the cold phase mostly remain unaltered until the temperature reaches 500 K. Above 500 K, the molecules with high abundances start to be destroyed, and are reformed to simple molecules, such as CO, H_2O and N_2. Some molecules are formed in the warm-up phase and the hot phase; $HCOOCH_3$ is formed on grain surfaces during the warm-up phase, while it is formed in the gas phase during the hot phase. Carbon-chains, such as C_2H_2 and cyanopolyynes, are effectively formed in the gas phase in the hot phase.

2.4.4 Spatial distribution of molecular abundances

In order to derive the spatial distributions of molecular abundances, we calculate molecular evolution in 10^4 parcels, which are selected from the 10^5 parcels traced in our RHD simulations. Figure 2.7 shows the distributions of the parcels, which are color-coded according to the fractional abundances of gaseous CH_3OH. The contour lines and gray scales depict the temperature and number density, respectively, in logarithm scale. The abundance of CH_3OH jumps at $r \sim 5$ AU in the middle stage and $r \lesssim 10$ AU in the late stage, where the temperature reaches its sublimation temperature ($\sim$100 K). At the outer radii, CH_3OH exists on grain surfaces. The spatial distributions of other many molecules are similar, while sublimation radii vary among species. In the late stage, the abundance of CH_3OH drops in the central region ($r \lesssim 1$ AU), because CH_3OH is collisionally dissociated.

Figure 2.7 indicates that the distributions of CH_3OH abundance follows the local temperature. To confirm this, we plot the abundance of CH_3OH as a function of temperature in the middle stage (gray square) and the late stage (black cross) in Figure 2.8. It clearly shows that the CH_3OH abundances follow the local temperatures. Note, however, the plots in the middle stage and the late stage are not identical. It

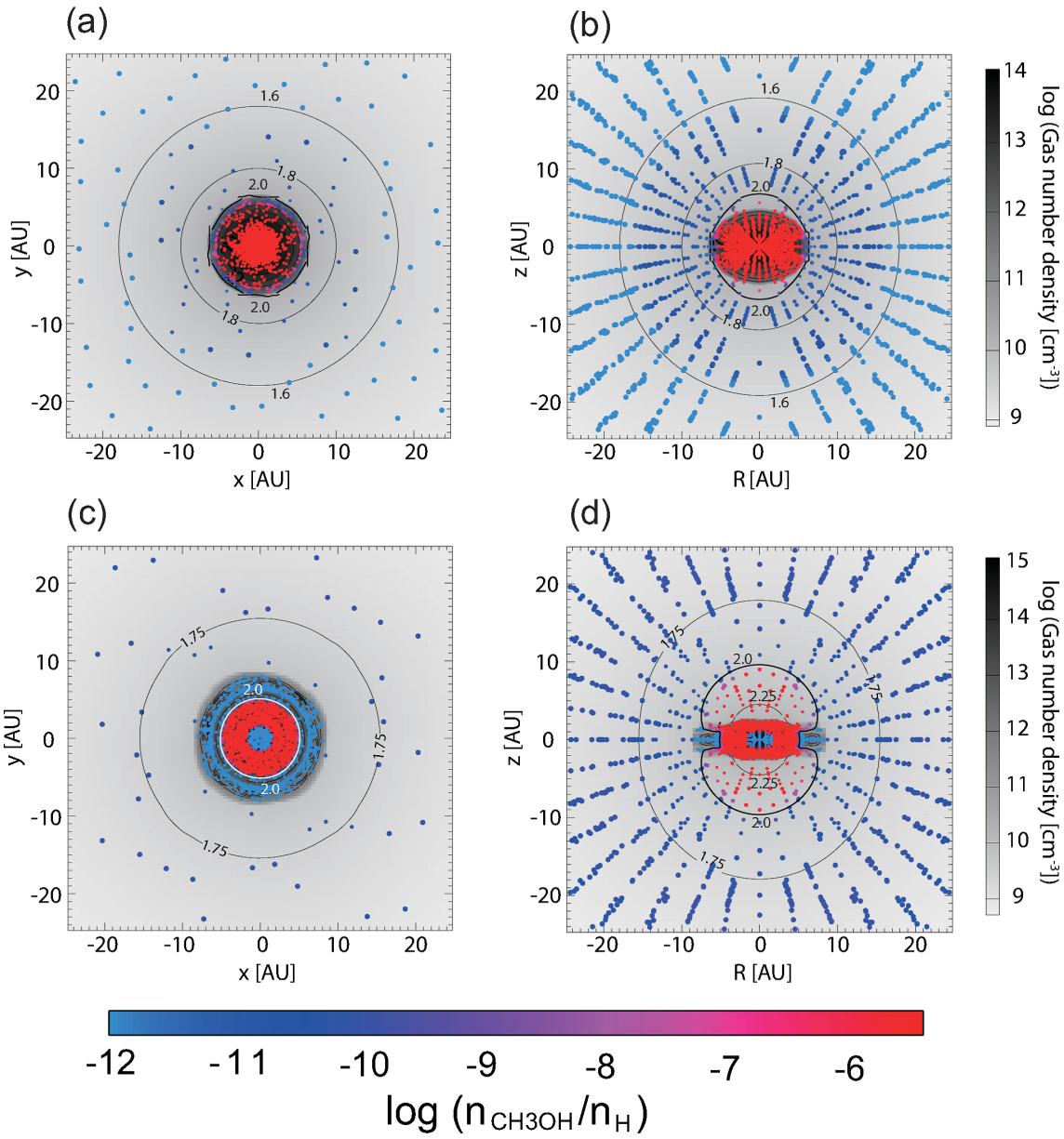

Figure 2.7: Spatial distributions of fluid parcels, which are color-coded according to abundance of gaseous CH_3OH, in the middle stage (a, b) and the late stage (c, d). The panels (a) and (c) represent the cross sections at $z = 0$, while (b) and (d) represent the R-z plane. In the panels (a) and (c), the parcels with $|z_p| < 0.5$ AU are plotted. The gray scales and the contour lines represent the gas number density and temperature distributions, respectively in logarithmic scale.

indicates that the fluid parcels with the similar temperature *at each evolutionary stage* have experienced similar thermal histories and molecular evolutions. At the temperature of around 100 K and 1200 K, the CH_3OH abundances are scattered. The CH_3OH abundances are determined by the sublimation at ∼100 K and collisional dissociation at ∼1200 K. The rates of these processes have the exponential dependence on the temperature, and a little difference of the thermal histories may make the scattering. In the late stage, there are two branches at the temperature below ∼100 K. The lower branch represents the CH_3OH abundances in the local low-temperature region inside the first core, which is mentioned in Section 2.4.1, while the upper branch represents the abundances in the envelope. Since the density is much higher in the first core than in the envelope, the degree of the depletion is much sever in the first core.

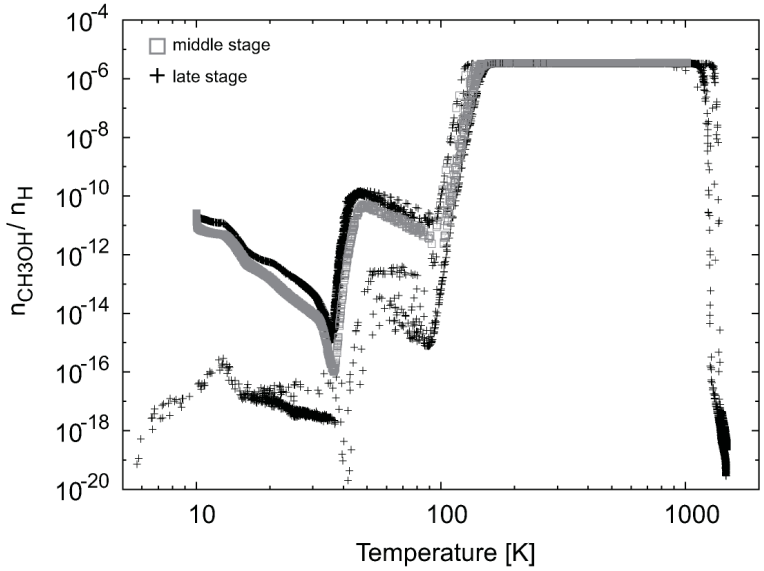

Figure 2.8: Abundance of gaseous CH_3OH as a function of temperature in the middle stage (gray square) and the late stage (black cross).

The spatial positions of the parcels at each snapshot constitute an irregular grid for which the molecular abundances, the density and the temperature are known. We have interpolated the molecular abundances in the density-temperature space with the nearest neighbors method, and obtained the table of the molecular abundances as the function of the density and the temperature at each snap shot. These tables are used to derive the molecular abundances at each evolutionary stage at the points of three-dimensional regular Cartesian-grids for which the temperature and the density are known from our hydrodynamic simulation. We use these data to derive the profiles of molecular abundances and column densities. Since the molecular evolution

in the star-forming regions is a non-equilibrium process, in general, the abundances are not given as a function of only the local physical conditions, but also depend on the past physical conditions. But in our case, the abundances can be given as a function of the local temperature and density *at each evolutionary stage*, because the flow pattern in our hydrodynamic simulation is simple, and again the fluid parcels with the similar physical conditions at each evolutionary stage have experienced the similar thermal histories and molecular evolutions.

Figure 2.9 shows the radial distributions of the physical parameters (a, b) and molecular abundances (c–h) in the $z = 0$ plane in the middle stage (a, c, e, g) and the late stage (b, d, f, h). The distributions along the rotational axis are shown in Figure 2.10, which is available in the online version of this paper. Since the temperature distributions are almost spherical (Figures 2.2(c) and 2.2(f)), and since the molecular abundances depend mainly on temperature, the molecular distributions are similar in Figure 2.9 and Figure 2.10, except near the first core ($r \lesssim 10$ AU). In the remainder of this subsection, we discuss the abundance profiles in detail.

Simple molecules

Simple molecules are often observed both in prestellar and protostellar cores, and are used to probe the physical conditions. Among the neutral species observable in radio, CO has the lowest binding energy, and thus its sublimation radius is relatively large; $r \sim 40$ AU in the middle stage and $r \sim 100$ AU in the late stage. It could be observed as a CO emission spot inside the heavy CO depletion zone. Sublimation radii of H_2CO and HCN are also relatively large; $r \sim 15$ AU in the middle stage and $r \sim 30$ AU in the late stage. In the late stage, there is the low-temperature region ($T \sim 10$ K) inside the first core on the equatorial plane (Section 2.4.1). All gaseous species including CO are on grain surfaces there, because of the low temperature and high density. The freeze-out time scale is estimated to be only hours. Sublimation radii in the equatorial plane of the polar species, such as H_2O and NH_3 are small: $R \sim 5$ AU. Since the temperature distribution deviates from the spherical system in the small scale ($r \lesssim 10$ AU), the sublimation radii of the polar species are slightly larger along the rotational axis; $z \sim 8$ AU. In the middle stage the abundance of CH_4 is constant, but in the late stage the abundance drops at $r \sim 1$ AU. The peak abundances of species mentioned above do not change much with time.

The dominant positive ion is H_3^+ outside the sublimation radius of CO. At the inner radii, the dominant positive ion varies in accordance with proton affinity; HCO^+ dominates inside the CO sublimation radius, but it is replaced by H_3CO^+ and then NH_4^+, as H_2CO and NH_3 sublimate subsequently. The ionization degree drops toward the first core, due to increasing density. Dominant charge carrier is the charged grains

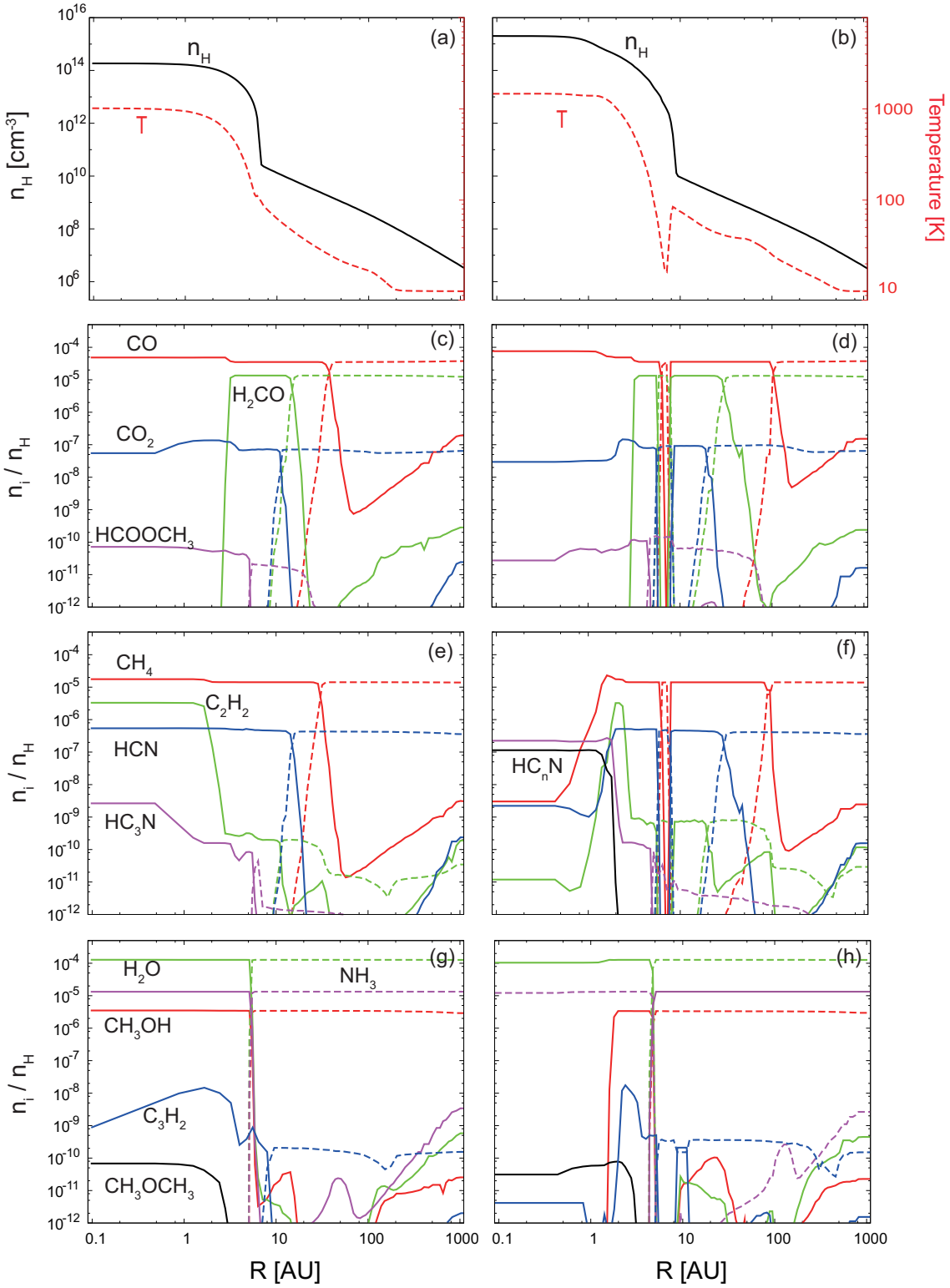

Figure 2.9: Radial distributions of physical parameters (a, b) and molecular abundances (c–h) in the $z = 0$ plane in the middle stage (a, c, e, g) and the late stage (b, d, f, h). In the panels (c–h), the solid lines represent gas-phase species, while the dashed lines represent ice-mantle species. HC_nN indicates total molecular abundances of HC_5N, HC_7N and HC_9N.

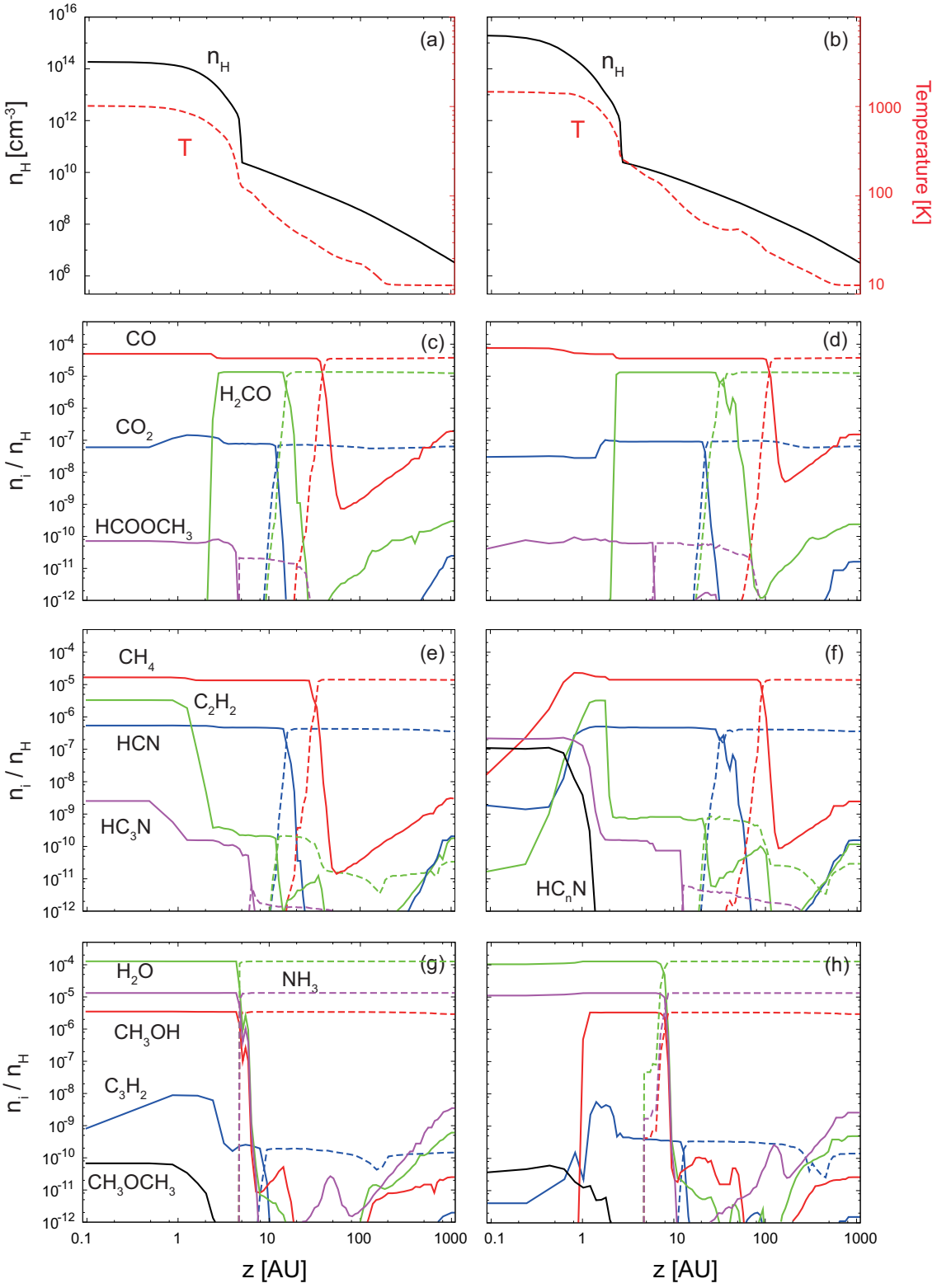

Figure 2.10: Distributions of physical parameters (a, b) and molecular abundances (c–h) along the rotational axis. Other details are the same as in Figure 2.9.

at $n \gtrsim 10^{10}$ cm^{-3}.

Carbon-chain molecules

Unsaturated carbon-chain molecules are typically associated with cold dense cloud cores, but have also been detected toward the Class-0/I sources, L1527 (Sakai et al., 2008) and IRAS 15398-3359 (Sakai et al., 2009). Sakai et al. (2008) suggested that carbon chains in the protostellar cores are formed from the sublimated CH_4 in the lukewarm region near the protostar. CH_4 reacts with carbon ion to form $C_2H_3^+$, which is a precursor of larger unsaturated carbon-chains. This formation scenario of carbon chains in the protostellar cores was named warm carbon-chain chemistry (WCCC) by Sakai et al. (2008), and confirmed by AW08 and Hassel et al. (2008).

We found WCCC does not efficiently occur in the first core stage; unsaturated carbon-chains do not increase at sublimation radii of CH_4, $r \sim 90$ AU and 30 AU in the middle and late stages. The abundance of carbon ion is lower due to the higher density of the envelope than in protostellar stages. Instead high temperature chemistry produces C_2H_2 and cyanopolyynes at $r <$ several AU. In the late stage, the abundance of C_2H_2 drops at $r \lesssim 1$ AU, where longer cyanopolyynes, HC_nN (n = 5, 7, 9), increase.

Large organic molecules

Large organic molecules sublimate at several AU. The total of gas and ice abundances of each species are almost constant throughout the core and envelope except for $HCOOCH_3$ and CH_3OCH_3. $HCOOCH_3$ is partly formed on grain surfaces at the lukewarm region, which expands from several tens AU (middle stage) to ~ 100 AU (late stage). CH_3OCH_3 is mainly formed in the gas phase at $r \lesssim 2$ AU. In the central region, the abundances of CH_3OH, $HCOOCH_3$ and CH_3OCH_3 drop in the late stage.

2.5 Discussion

2.5.1 Molecular column densities

Detection and observation of first cores is one of the most important challenges in ALMA era. First cores are characterized by a AU-size hydrostatic core and low-velocity outflow with a wide opening angle. While size of the core can be measured by high angular resolution dust continuum observation, molecular line observations are also necessary to confirm the kinetic structure. Molecular abundances obtained in our model are useful to predict where the various molecular lines would arise. We especially focus on large organic species, which are abundant at the vicinity and the

surface of the first core. Since detailed radiation transfer modeling (e.g., Tomisaka & Tomida, 2011) is out of the scope of this work, here we compare the column densities of assorted species in our model with those estimated from the observations towards a prototypical hot corino, IRAS 16293-2422, to evaluate if our model column densities of large organic species are high enough to produce lines.

Figure 2.11 (solid black line) shows the cumulative column densities of gases along the rotational axis from the outer edge of the core to a height z above the midplane, $N_z(z) = \int_z^\infty n dz'$. The vertical solid lines represent the first core surface. The vertical dashed and dotted lines represent the heights where the optical depths of dust continuum reach unity at the wavelength of 100 μm and 1 mm, respectively. The optical depth of dust continuum, τ, is estimated as

$$\tau = 1 \left(\frac{N_z}{8 \times 10^{25}\,\mathrm{cm}^{-2}} \right) \left(\frac{\lambda}{1\,\mathrm{mm}} \right)^{-2}, \tag{2.12}$$

referring to Hildebrand (1983). At 100 μm the optical depth reaches unity in the envelope. At 1 mm, on the other hand, we can look into the envelope and the surface of the first core, although the optical depth exceeds unity at deeper layers of the first core (see also Saigo & Tomisaka, 2011). The gases in front of the $\tau_{1\mathrm{mm}} \sim 1$ plane can be probed by absorption lines, since the gas in front is cooler than the $\tau_{1\mathrm{mm}} \sim 1$ plane. In the line of sight offset from the rotational axis where dust continuum is optically thin ($R \gtrsim 6$ AU), the line could be emission (Figure 2.12). We calculate the molecular column density in front of the $\tau_{1\mathrm{mm}} = 1$ plane in the face-on system,

$$N_{z_{\tau=1},i}(x,y) = \int_{z_{\tau=1}(x,y)}^{\infty} n_i(x,y,z')dz', \tag{2.13}$$

where $z_{\tau=1}$ represents the height z where the optical depth reaches unity at 1 mm, and n_i represents the number density of species i. Figure 2.12 shows $N_{z_{\tau=1},i}$ of assorted molecules as a function of R in the middle stage (upper panel) and the late stage (lower panel).

At $R \lesssim 6$ AU the first core is optically thick for 1 mm dust continuum, and $N_{z_{\tau=1},i}$ is almost constant. $N_{z_{\tau=1},\mathrm{CO}}$ sharply increases inwards at its sublimation radius (several tens AU) and at the first core surface (several AU). $N_{z_{\tau=1},i}$ of large organic molecules sharply increases at their sublimation radii which is close to the first core surface. The peak value of $N_{z_{\tau=1},i}$ for each species are not much different between the middle and late stages. CH_3OCH_3 is an exception; its peak value of $N_{z_{\tau=1},\mathrm{CH_3OCH_3}}$ increases with time.

The emission of these complex organic molecules have been detected towards several low mass protostars (e.g., Cazaux et al., 2003; Bottinelli et al., 2004; Maret et

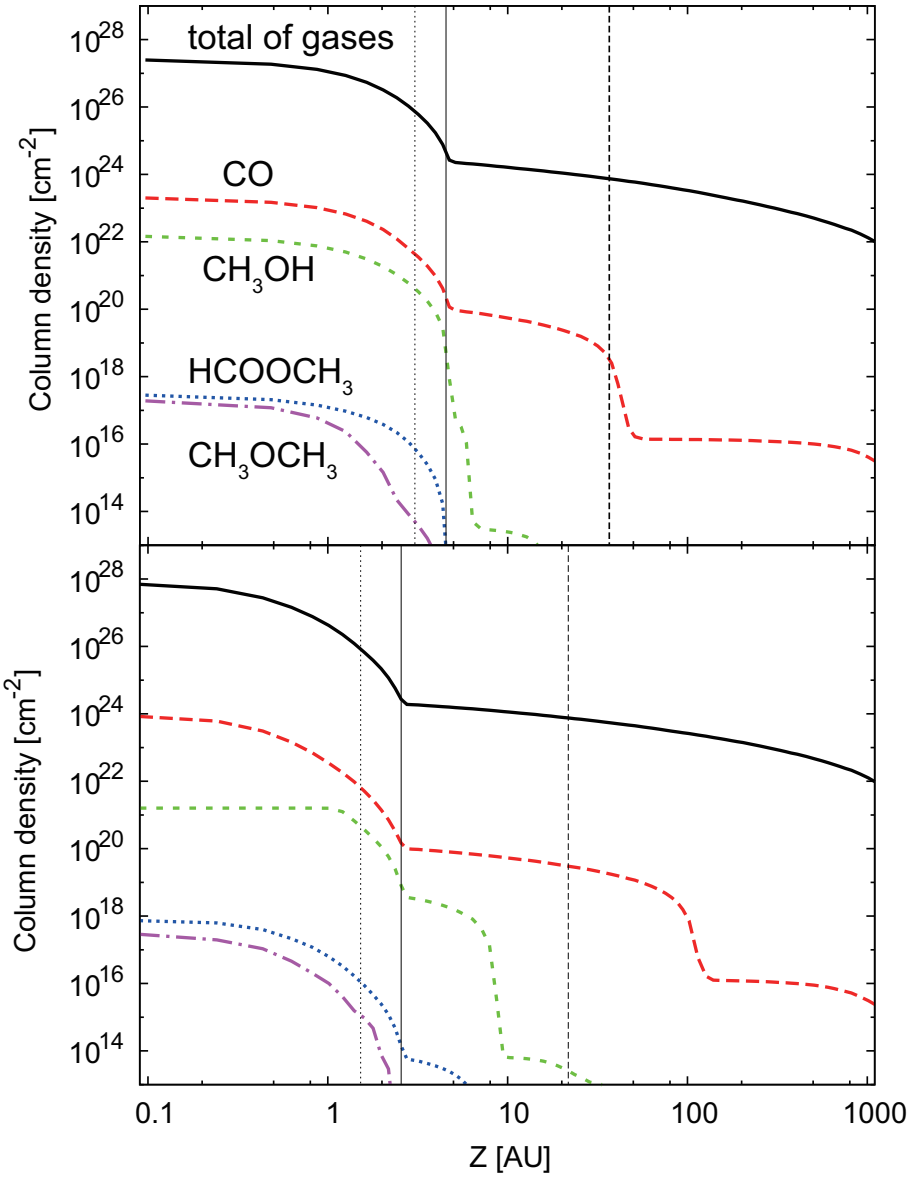

Figure 2.11: Column densities along the rotational axis integrated from the outer edge of the envelope to z, $N_{z,i}(z) = \int_z^\infty n_i dz'$, in the middle stage (upper panel) and the late stage (lower panel). The vertical solid lines represent the first core surface. The vertical dashed and dotted lines represent the heights from the midplane, where the optical depths of dust continuum reach unity with the wave length of 100 μm and 1 mm, respectively.

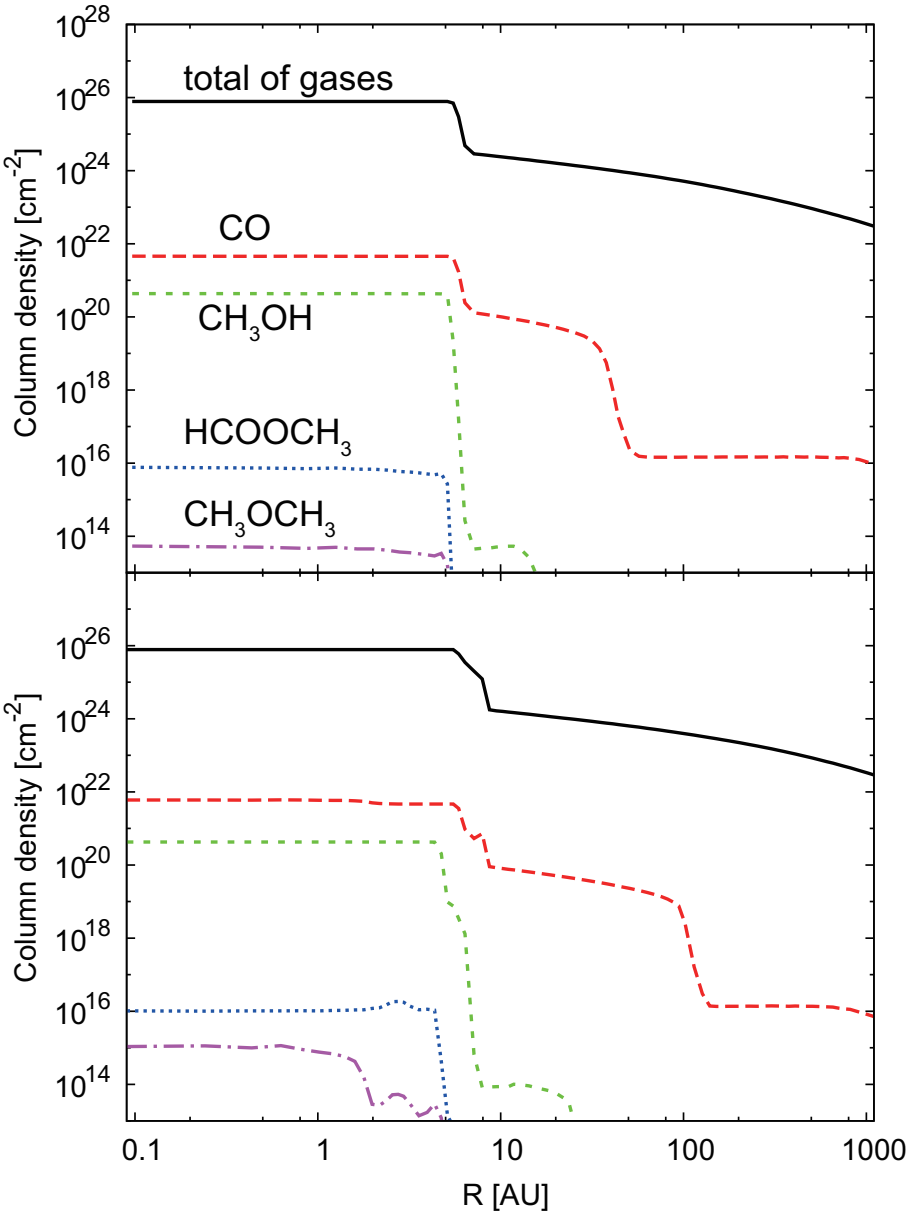

Figure 2.12: Gaseous molecular column densities in front of the $\tau_{1\mathrm{mm}} = 1$ plane in the face-on object.

al., 2005). The beam-averaged column densities derived from interferometric observations toward IRAS 16293-2422 are $N_{\rm CH_3OH} = 1.1 \times 10^{18}$ cm^{-2}, $N_{\rm HCOOCH_3} = 6.8 \times 10^{15}$ cm^{-2} (Kuan et al., 2004), and $N_{\rm CH_3OCH_3} = 6.4 \times 10^{15}$ cm^{-2} (Chandler et al., 2005). Kuan et al. (2004) also derived $N_{^{13}\rm CH_3OH} = 8.1 \times 10^{16}$ cm^{-2}. It indicates that the ^{12}CH$_3$OH emission is optically thick, since the carbon isotope ratio of CH$_3$OH, $N_{^{12}\rm CH_3OH}/N_{^{13}\rm CH_3OH} \sim 14$, is much smaller than the elemental abundance ratio, [^{12}C/^{13}C] ~ 60, in ISM (e.g., Langer & Penzias, 1993; Lucas & Liszt, 1998). Our model column densities of CH$_3$OH and HCOOCH$_3$ in the middle and late stages at $R \lesssim 6$ AU are comparable or larger than those values. Hence it would be reasonable to expect that the column densities of CH$_3$OH (and HCOOCH$_3$) at $R \lesssim 6$ AU in our model are high enough to be $\tau_l \sim 1$ at least in some transitions. Since the gas in the first core surface and the envelope is cooler than the first core, we expect absorption lines, if we observe the object from the pole-on angle. Assuming the lines and continuum are thermalized, the expected difference of brightness is

$$\Delta T_b = |T_{bg} - T_{fg}|[1 - \exp(-\tau_l)], \tag{2.14}$$

where T_{bg} and T_{fg} are the temperatures at $\tau_{\rm 1mm} = 1$ and $\tau_l = 1$, respectively. We assume that τ_l for CH$_3$OH reaches unity at the height where the model column density of CH$_3$OH reaches 1.1×10^{18} cm^{-2}. In the middle stage for CH$_3$OH, ΔT_b is $\gtrsim$40 K at $R \lesssim 6$ AU, which is detectable in 1.6 hours toward the distance of 120 pc with S/N $\gtrsim 10$ and velocity resolution of 0.1 km/s in the extended configuration ($\sim$0.1") of ALMA at Band 7 (345 GHz). More integration time would be required to detect HCOOCH$_3$, because the $\tau_l = 1$ plane for HCOOCH$_3$ is closer to the $\tau_{\rm 1mm} = 1$ plane than that for CH$_3$OH is (i.e., ΔT_b for HCOOCH$_3$ is smaller) (see Figure 2.11). We found that the column densities of HCOOH and CH$_3$CN in our model are also comparable to the observed values in the hot corinos. Although, detailed radiation transfer calculation is needed to confirm these estimates.

On the other hand, the column density of CH$_3$OCH$_3$ in our model is much less than the observed toward IRAS 16293-2422 both in the middle and late stages, and thus would not be high enough to produce observable lines. Our results show that first cores and the surrounding warm envelopes could be observed as very compact hot corinos without stellar signatures, and the large organic molecules can be good tracers of first cores. In the rest of this paper, we call the warm gases with the large organic molecules a prestellar hot corino.

2.5.2 Uncertainties in the reaction network model

There are several caveats to our model abundances and column densities of large organic molecules presented above. As mentioned in Section 2.4, H_2CO is collisionally dissociated at lower temperatures ($\sim$500 K) than other large organic molecules, since the value of γ (1.75×10^4 K) is small for the collisional dissociation, $H_2CO + M \rightarrow H_2 + CO + M$, compared with those of other large organic molecules. It should be noted that the value of γ in the collisional dissociations listed in Table A.2 are basically determined by the difference between the formation enthalpy of reactants and products, but the products and branching ratios for various possible sets of products are not well constrained by laboratory experiments. If there exists the channels with lower γ for the destruction of other large organic molecules, the abundances of these molecules at $T \gtrsim 500$ K could decrease by several orders of magnitude relative to our results. The column densities of the large organic molecules in the middle stage (Figure 2.12, upper panel), however, would not change, since the temperature is lower than 500 K at $\tau_{1\mathrm{mm}} \lesssim 1$. The column densities in the late stage (Figure 2.12, lower panel) would decrease by about one order of magnitude.

The abundances of $HCOOCH_3$ and CH_3OCH_3 in our model depend on the branching ratios of grain surface recombination, which contributes to their formation in the hot phase. We recalculate the molecular abundances in the representative fluid parcel discussed in Section 2.4.3, assuming all the product channels of grain surface recombination (both with a negatively charged grain and with a neutral grain) are equally weighted. Then, the peak abundances of $HCOOCH_3$ and CH_3OCH_3 are enhanced by a factor of 8 and 12, respectively. The column densities would be enhanced almost by the same factor, since grain surface recombination is effective around/in the dense first core. In contrast, the abundance of CH_3OH does not strongly depend on the assumed branching ratio of the recombination, since CH_3OH is mostly formed by hydrogenation on grain surfaces in the cold phase.

While the cosmic ionization rate is set to be 1.3×10^{-17} s^{-1} in our model, a larger value of 5×10^{-17} s^{-1} is suggested by recent work (Dalgarno, 2006). We recalculate the molecular abundances in the representative fluid parcel with the cosmic-ray ionization rate of 5×10^{-17} s^{-1}. The peak abundances of large organic molecules are enhanced by a factor of 2–5 compared to our original model with the cosmic-ray ionization rate of 1.3×10^{-17} s^{-1}.

In summary, our model might underestimate the abundances of large organic molecules at $T \lesssim 500$ K by one order of magnitude, while our model might overestimate them at $T \gtrsim 500$ K by several orders of magnitude. The model column densities might be underestimated in the middle stage by one order of magnitude, while those in the late stage could be higher or lower by one order of magnitude.

Table 2.4: Comparison between the protostellar and prestellar hot corino models.

	Protostellar hot corino	Prestellar hot corino
Radius ($T = 100$ K)	120 AU[1]	<10 AU
Gas density ($T = 100$ K)	10^7 cm^{-3}[1]	10^{10} cm^{-3}
H_2CO	2.5(-5)	2.6(-5)
CH_3OH	1.0(-5)	6.4(-6)
$HCOOCH_3$	3.3(-9)	4.8(-11)
CH_3OCH_3	6.0(-11)	2.2(-13)
HCOOH	3.0(-9)	1.3(-10)

2.5.3 Comparison with protostellar hot corinos

Here, we compare the physical structures and chemical compositions of the prestellar hot corino (prestellar HC) with those of a protostellar hot corino (protostellar HC). We refer to the spherical RHD model of a star-forming core by Masunaga & Inutsuka (2000), and AW08 for the protostellar hot corino model. Such comparison is useful to unveil differences between prestellar and protostellar HCs. It should be noted, however, that the physical structures of the cores are different; e.g., while the models of Masunaga & Inutsuka (2000) and AW08 are non-rotating cores of 3.9 $M_\odot$, our model is the rotating core of 1 $M_\odot$.

The top two columns of Table 2.4 show the mean radius and the gas number density of $T = 100$ K region. It is clear that the prestellar HC is more compact and denser than the protostellar HC by an order of magnitude; the protostar is more luminous and their envelopes are more sparse than in the first core stage.

We compare the abundances of the large organic molecules in the central region ($r \sim 5$ AU) of our model with those of the protostellar HC model. While AW08 traced 13 parcels in the RHD simulation of Masunaga & Inutsuka (2000) to calculate the molecular abundances, the reaction network used in AW08 is different from our network. In order to make comparisons easy, we revisit the calculation of AW08 with some modifications; we calculate the temporal variations of the molecular abundances using our network model in the parcel which reaches $r = 15$ AU at the protostellar age of 9.3×10^4 yr. We adopt this parcel, because the abundances are mostly constant at $r \lesssim 100$ AU according to AW08. While AW08 used the initial temperature of 6 K, we set it at 10 K when the temperature is lower than 10 K in the original model. Table 4 shows the abundances of the large organic molecules at 15 AU in the protostellar HC model and 5 AU in the prestellar HC model. Comparing the second row of Table 4 with Table 3 of AW08, our modifications in the network and temperature lead to order-of-magnitude changes in the abundances of listed species except for

[1]Masunaga & Inutsuka (2000)

$HCOOCH_3$. Among the listed species, the abundances of H_2CO and CH_3OH are similar in the prestellar HC model and the protostellar HC model. These species are formed during the cold phase by the subsequent hydrogenation reactions of CO on grain surfaces. The other species are less abundant in the prestellar HC model. In the protostellar HC model, they are efficiently formed in the lukewarm region. On the other hand, in the prestellar HC model the lukewarm region is small, and the time to form these species is limited. It indicates that the abundances of these molecules are sensitive to the luminosity of the central object.

2.5.4 Accretion shock heating layers

The supersonic accretion of the envelope material to the first core causes the shock wave. This accretion shock is isothermal, because the radiation from post-shock gas heats up pre-shock gas, and the temperature in the pre-shock and post-shock gases become equal (e.g., Omukai, 2007; Saigo & Tomisaka, 2011; Commerçon et al., 2011). Between the pre- and post-shock gases, the shock heating layer is formed, in which the gas temperature reaches $\sim$2000 K at the maximum. In contrast, the grain temperature increases to only $\sim$200 K. The thickness of this layer is $\sim 10^{-3}$ AU, and the cooling time scale of the gas is $\sim$1 hour after crossing the shock front (see Fig. 3 of Saigo & Tomisaka, 2011). In our hydrodynamic simulation the shock heating layer is not spatially resolved, and thus our chemical calculations neglect the temperature rise in the shock heating layer. In order to evaluate the effect of shock heating on chemistry, we recalculate the molecular abundances in the parcel discussed in Section 2.4.3 by adding 1 hour integration at the constant temperature when the parcel reaches the first core surface. Since the temperature of the shock heating layer should vary depending on the mass of the first core and the radius where the shock occurs, we calculate two cases: the gas temperature of 1000 K and 2000 K. The density is assumed to be the same as the post-shock gas along the trajectory, $n_{\rm H} = 8.5 \times 10^{11}$ cm^{-3}. The grain temperature is assumed to be 200 K, at which temperature ice-mantle species are almost evaporated. In the pre-shock and post-shock regions, on the other hand, the species with the high binding energies, such as CH_3OH, is mostly freeze-out on grain surfaces, since the grain temperature is about 80 K. To focus on high temperature chemical processes, we discuss changes of the total (gas and ice combined) abundances in this subsection.

In the case of the gas temperature of 1000 K, the shock heating does not affect the chemistry. Even in the case of the gas temperature of 2000 K, the heating has a limited effect on the chemistry; among abundant species ($n_i/n_{\rm H} > 10^{-12}$), only 23 species increase or decrease by a factor of >2 in the shock heating layer. Figure 2.13 shows the spatial variation of the temperature (upper panel) and molecular

abundances (lower panel) along the trajectory after the parcel experience the shock heating of 2000 K at $r \sim 7$ AU and $t_{\rm final} - t = 1930$ yr (see Figure 2.6). The horizontal axis in Figure 2.13 is the position of the parcel in r. In the lower panel, the solid lines show the molecular abundances with shock heating, while the dashed lines show our original model without the shock heating. The abundances of HCN and CH_3OH are almost the same between the two models. H_2CO is the most sensitive to the shock heating; it decreases approximately five orders of magnitude by collisional dissociation to form CO and H_2. Since the abundances of CO and H_2 are higher than that of H_2CO, the effect of H_2CO dissociation to other molecules is insignificant. The difference between the two models diminishes when the temperature reaches $\sim$500 K, at which collisional dissociation of H_2CO becomes efficient in the original model. Carbon species, such as C_2H_2, are also sensitive to the shock heating; their abundances are temporally enhanced by approximately four orders of magnitude by the reaction of C_3H_4 and H_2 with the potential barrier of 2.3×10^4 K. The difference in the C_2H_2 abundance diminishes when the temperature reaches $\sim$800 K. Therefore our results in Section 2.4 might overestimate the abundance of H_2CO, while underestimate the abundance of C_2H_2 in the first core except for the hot central region ($r \lesssim 3$ AU).

While our simple calculation shows that the shock heating affects abundances of some molecules, the effect is limited and the shock heating does not lead to a significant change in our results presented in Section 2.4.

2.5.5 Toward the chemistry in circumstellar disks

The first core is a transient object formed prior to the protostar. Here, we briefly discuss what happens after the formation of the protostar and the circumstellar disk in terms of chemistry.

There are several studies which investigate the formation and evolution of the circumstellar disk using three-dimensional hydrodynamic simulations. We refer to Machida et al. (2010, 2011), which investigated a longest-term evolution of the circumstellar disk, starting from the gravitational collapse of the molecular cloud core. While the central part ($r \lesssim 1$ AU) of the first core collapses to form a protostar, the outer part directly evolves to the cicumstellar disk with a Keplerian rotation. In that case, the chemical composition of the first core corresponds to the initial composition of the circumstellar disk; the total of gas and ice abundances at $r \gtrsim 3$ AU ($T \lesssim 500$ K) in the first core is mostly the same as those in the cold molecular cloud core, while the inner part ($T \gtrsim 500$ K) is dominated by the simple molecules, such as CO, H_2O and N_2.

When the protostar is born, the mass of the circumstellar disk ($\sim$0.01–0.1 $M_\odot$)

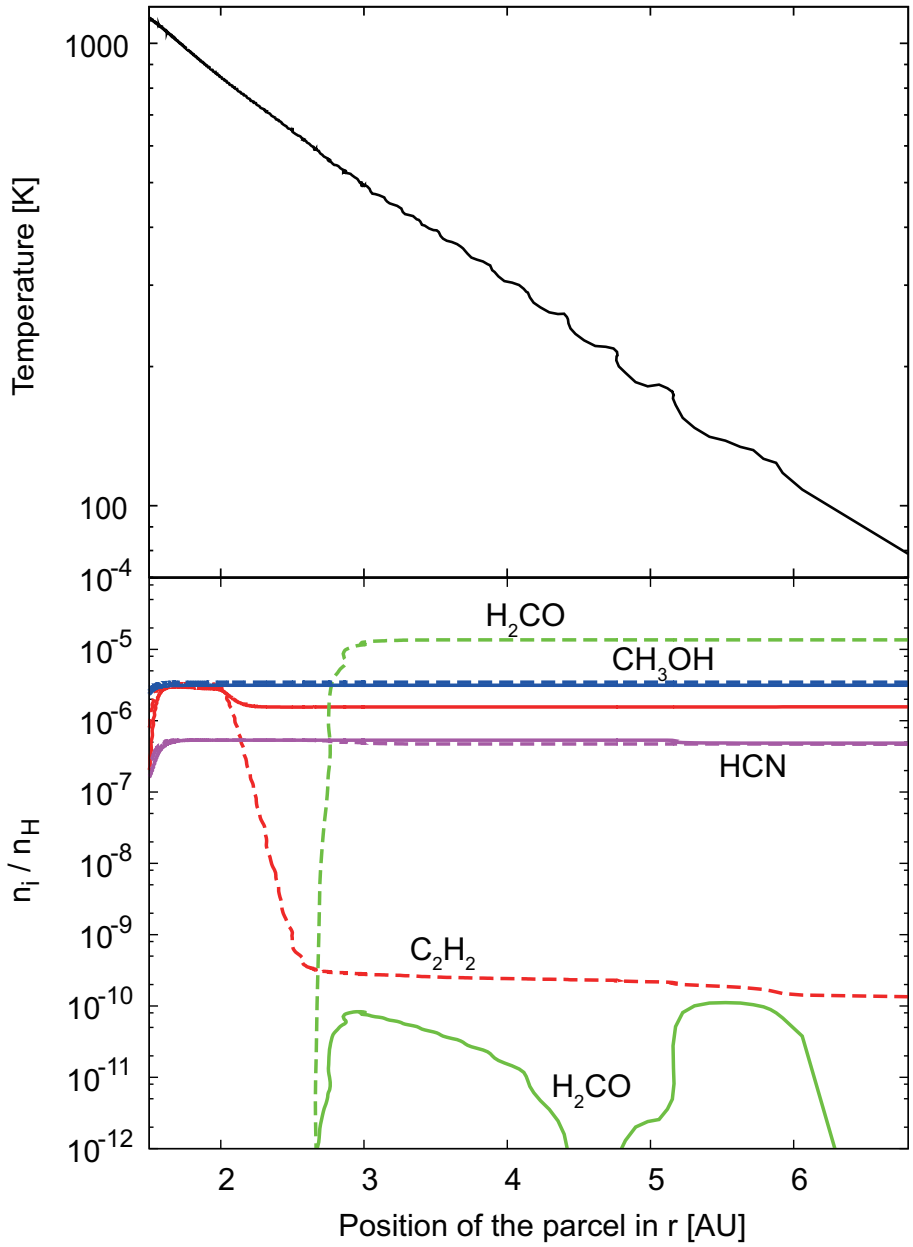

Figure 2.13: Temperature (upper panel) and total (gas and ice) molecular abundances of selected species (lower panel) along the trajectory discussed in Section 2.4.3 after the parcel enter the first core at $r \sim 7$ AU. The solid and dashed lines in the lower panel represent the abundances with and without the shock heating, respectively.

overwhelms that of the protostar ($\sim 10^{-3}\ M_\odot$). It causes the gravitational instability, and angular momentum is efficiently transported via spiral arms. The mass of the protostar and circumstellar disk increase with time via the accretion from the circumstellar disk and infalling envelope, respectively. Therefore most of the material constituting the first core would accrete to the protostar, and be replaced by the newly accreted envelope material during the disk evolution, although a small fraction of the first core material may have been transported to outer region of the disk carrying angular momentum. Since the envelope material in the protostellar stage is more abundant in large organic molecules than in the first core stage (Section 2.5.3), the circumstellar disk would be enriched with the large organic molecule. The large organic molecules also might be formed in the circumstellar disk via gas-phase and/or grain-surface reactions if the fluid parcels stay in the disk long enough (10^4–10^5 yrs) (e.g., Charnley et al., 1992; Garrod & Herbst, 2006; Aikawa et al., 2012). On the other hand, increasing UV radiation and decreasing attenuation in the envelope cause the photodissociation of molecules, such as H_2O and CO, at the surfaces of the disk and the wall of the outflow cavity (e.g., Visser et al., 2011).

2.6 Conclusion

We have investigated molecular evolution in the first hydrostatic core stage. We performed the three-dimensional radiation hydrodynamic simulation from the molecular cloud core to the first core. We traced the fluid parcels, which follow the local flow of the gas, and solved molecular evolution along the trajectories, coupling gas-phase and grain-surface chemistry. We derived the spatial distributions of molecular abundances and column densities in the molecular cloud core harboring the first core. Our conclusions are as follows.

1. We found that the total molecular abundances of gas and ice of many species in the cold era (10 K) remain unaltered until the temperature reaches $\sim$500 K. The gas abundances in the warm envelope and outer layers of the first core ($T \lesssim 500$ K) are mainly determined via the sublimation of ice-mantle species. Above 500 K, the abundant molecules, such as H_2CO, start to be destroyed mainly via collisional dissociation or reactions with H atom, and converted to the simple molecules, such as CO, H_2O and N_2. On the other hand, some molecules are effectively formed; carbon-chains, such as C_2H_2 and cyanopolyynes, are formed at the temperature of >700 K.

2. Gaseous large organic molecules are associated with the first core ($r < 10$ AU). Although the abundances of large organic molecules in the first core stage are

comparable or smaller than in the protostellar hot corino, their column densities in our model are comparable to the observed values toward the prototypical hot corino, IRAS 16293-2422. We propose that large organic molecules can be good tracers of the first cores.

3. The shock wave occurs when the envelope material accretes onto the first core. We found that the shock heating has little effect on chemistry, if the maximum temperature in the shock heating layer is below 1000 K. Even if the gas temperature reaches 2000 K, the heating has a limited effect on chemistry. While it significantly decreases the H_2CO abundance and increases the C_2H_2 abundance in the outer parts of the first core ($r \lesssim 3$ AU), it has little effect on other species.

4. Recent hydrodynamic simulations have shown that outer region of the first core could directly evolve to the circumstellar disk. In that case, the chemical composition of the first core corresponds to the initial composition of the circumstellar disk; the total abundances of gas and ice at $r \gtrsim 3$ AU ($T \lesssim 500$ K) are mostly determined in the cold molecular cloud cores, while inner parts ($T \gtrsim 500$ K) are dominated by simple molecules, such as CO, H_2O and N_2.

Chapter 3

Water in protoplanetary disks: deuteration and turbulent mixing

[1] *The content of this chapter is based on:*
Furuya, K. et al. 2013, ApJ, 779, 11

[1]The content of this chapter is an author-created, un-copyedited version of an article published in The Astronomical Journal. IOP Publishing Ltd is not responsible for any errors or omissions in this version of the manuscript or any version derived from it. The Version of Record is available online at http://iopscience.iop.org/0004-637X/779/1/11.

Abstract

We investigate water and deuterated water chemistry in turbulent protoplanetary disks. Chemical rate equations are solved with the diffusion term, mimicking turbulent mixing in vertical direction. Water near the midplane is transported to the disk atmosphere by turbulence and destroyed by photoreactions to produce atomic oxygen, while the atomic oxygen is transported to the midplane and reforms water and/or other molecules. We find that this cycle significantly decreases column densities of water ice at $r \lesssim 30$ AU, where dust temperatures are too high to reform water ice effectively. The radial extent of such region depends on the desorption energy of atomic hydrogen. Our model indicates that water ice could be deficient even outside the sublimation radius. Outside this radius, the cycle decreases the D/H ratio of water ice from $\sim 2 \times 10^{-2}$, which is set by the collapsing core model, to 10^{-4}–10^{-2} in 10^6 yr, without significantly decreasing the water ice column density. The resultant D/H ratios depend on the strength of mixing and the radial distance from the central star. Our finding suggests that the D/H ratio of cometary water ($\sim 10^{-4}$) could be established (i.e. cometary water could be formed) in the solar nebula, even if the D/H ratio of water ice delivered to the disk was very high ($\sim 10^{-2}$).

3.1 Background

Water is one of the most important molecules in star and planet forming regions from the perspective of the oxygen reservoir and the origin of Earth's ocean. It is well established that water ice forms on grain surfaces and is already abundant ($\sim 10^{-4}$ per hydrogen nucleus) in molecular clouds at visual extinctions $A_{\rm V} \gtrsim 3$ magnitude (e.g., Whittet, 1993). Water has also been detected toward star and planet forming regions, such as prestellar cores (Caselli et al., 2012), protostellar envelopes (e.g., Ceccarelli et al., 2000; Boogert et al., 2008), and Class II protoplanetary disks (PPDs; Terada et al., 2007; Honda et al., 2009; Carr & Najita, 2008; Hogerheijde et al., 2011). Although there is no doubt that water exists in all the phases of star formation, the evolution of water from molecular clouds to PPDs remains unclear.

D/H ratio can be a useful tool to probe the evolution of water. Comets are preserved samples of the cold ice-bearing regions in the solar nebula (Brownlee, 2003). So far, the HDO/H_2O abundance ratio has been measured in nine comets; seven from the Oort cloud ($\sim$(4–10) $\times 10^{-4}$; e.g., Villanueva et al., 2009; Bockelée-Morvan et al., 2012), and two from the Kuiper belt ((3–<4) $\times 10^{-4}$; Hartogh et al., 2011; Lis et al., 2013). In all sources, the HDO/H_2O ratio is higher by about one order of magnitude than the elemental abundance of deuterium in the interstellar medium ($\sim 1.5 \times 10^{-5}$; Linsky, 2003). On the other hand, to the best of our knowledge, there has been no detection of HDO toward PPDs in the Class II phase except for Ceccarelli et al. (2005). Although they claimed a 4σ detection of HDO vapor toward DM Tau, it has been questioned by Guilloteau et al. (2006).

Recently, the HDO/H_2O ratio in the gas phase has been measured toward four Class 0–I low-mass protostars, which are summarized in Table 3.1. We distinguish between the single dish and interferometer observations. The single dish observations, on the other hand, provide the integrated emission from larger scales. The interferometer observations provide model-independent estimates of the HDO/H_2O ratio in the most inner regions of hot corinos, where ice is sublimated (Jørgensen & van Dishoeck, 2010). The HDO/H_2O ratio derived by using interferometers varies greatly among sources. The ratios observed towards IRAS 16293-2422 and NGC 1333-IRAS4B are slightly higher than the cometary values (Jørgensen & van Dishoeck, 2010; Persson et al., 2013), whereas the other two sources (NGC 1333-IRAS2A and NGC 1333-IRAS4A) show much higher ratios (Taquet et al., 2013a). The difference between the HDO/H_2O ratio observed toward comets and protostar envelopes may indicate that water formed in the cloud/core phase was reprocessed in the solar nebula.

Table 3.1: Observed HDO/H_2O Ratios Toward Class 0–I Sources.

Source	HDO/H_2O	
	Single Dish	Interferometer
IRAS 16293-2422	$(1.4–5.8)\times10^{-2}$[a]	$(0.66–1.2)\times10^{-3}$[b]
NGC 1333-IRAS2A	$\geq10^{-2}$[c]	$(0.3–8)\times10^{-2}$[d]
NGC 1333-IRAS4A	–	$(0.5–3)\times10^{-2}$[d]
NGC 1333-IRAS4B	–	$\lesssim6\times10^{-4}$[e]

We briefly outline the evolution of HDO/H_2O ratio during star and disk formation referring to previous theoretical models. Visser et al. (2011) investigated molecular evolution from the collapse of dense cloud cores to the formation of circumstellar disks in two spatial dimensions. They showed that the majority of water is delivered from the core to the disk as ice. Although they did not include isotopes, their results indicate that D/H ratio of water delivered to the disk is determined in the parent cloud core. In the hot inner regions of disks, where gas temperature is higher than 500 K, isotopic exchange between HDO and H_2 occurs, and the HDO/H_2O ratio can decrease to $\sim10^{-5}$ (Lécluse & Robert, 1994). Such reprocessed water could be mixed with unprocessed water via radial mixing and accretion (Drouart et al., 1999; Hersant et al., 2001; Yang et al., 2013). The resultant HDO/H_2O ratio depends on the thermal history of the disk and efficiency of radial mixing, i.e. how much material diffuse from the inner hot region (>500 K) to outer radii. If we assume the disk formation model of Visser et al. (2011), the HDO/H_2O ratio decreases by a factor of <2 on average from the initial cloud value, since only ∼30 % of the disk mass experiences high temperatures of several 100 K until envelope accretion onto the protostellar system halts.

The primary motivation of this work is to investigate the impact of turbulent mixing in the vertical direction on the HDO/H_2O ratio in the Class II PPDs. Deuterium fractionation in Class II PPDs has been studied numerically by several authors without mixing (e.g., Aikawa & Herbst, 2001; Aikawa et al., 2002; Ceccarelli & Dominik, 2005; Willacy, 2007; Willacy & Woods, 2009). Willacy & Woods (2009) investigated deuterium chemistry in inner disks ($\leq$ 30 AU) considering the accretion flow. In the Class II phase, the disk surface is irradiated by stellar ultraviolet (UV) photons and X-rays. Then, oxygen is mainly in atomic form at the disk surface, while it is in water

[a]Coutens et al. (2012); the value at $T > 100$ K in their modeling.
[b]Persson et al. (2013); Source A.
[c]Liu et al. (2011); the value at $T > 100$ K in their modeling.
[d]Taquet et al. (2013a).
[e]Jørgensen & van Dishoeck (2010).

near the midplane (e.g., Bergin et al., 2007, and references therein). They found that the HDO/H_2O ratio at the midplane retains their initial value ($\sim 2 \times 10^{-2}$, which is set by their dense cloud core model) for 10^6 yr, probably because water is not destroyed efficiently in the regions where UV photons and X-rays are attenuated. However, turbulent mixing could change the situation drastically. If turbulence exists, water would be transported to the disk atmosphere and destroyed by photoreactions, while atomic oxygen would be transported to the disk midplane and reforms water and/or other molecules. Such destruction and reformation processes are of potential importance for the HDO/H_2O ratio in disks; the HDO/H_2O ratio could be significantly changed from that in molecular clouds/cores.

The plan of this chapter is as follows. We describe our physical model and chemical model with vertical mixing in Section 3.2 and 3.3, respectively. In Section 3.4, we present how the vertical mixing affects water and deuterated water chemistry. In Section 3.5, we discuss the effect of initial HDO/H_2O ratio, radial mass transport, and dead zone on our results presented in Section 3.4. We also discuss the uncertainties of grain surface chemistry and the implication of our model results for the D/H ratio of cometary water. We summarize our conclusions in Section 3.6.

3.2 Disk structure

We adopt the disk model of Nomura & Millar (2005) with the addition of X-ray heating by Nomura et al. (2007). Similar models have been used to study the chemical evolution without deuterium in protoplanetary disks (Walsh et al., 2010, 2012; Heinzeller et al., 2011). Here we briefly describe the disk model. More details can be found in the original papers (Nomura & Millar, 2005; Nomura et al., 2007).

The model describes the structure of a steady, axisymmetric Keplerian disk surrounding a typical T Tauri star with the mass $M_* = 0.5\ M_\odot$, radius $R_* = 2\ R_\odot$, and effective temperature $T_* = 4000$ K. The α-disk model (Shakura & Sunyaev, 1973) is adopted to determine the radial distribution of the surface density, assuming the viscous parameter $\alpha = 10^{-2}$, and accretion rate $\dot{M} = 10^{-8}\ M_\odot\ \mathrm{yr}^{-1}$. The gas temperature, dust temperature and density distributions of the disk are calculated self-consistently (see Section 2 of Nomura & Millar, 2005, for details). The stellar UV luminosity is set to be $\sim 10^{31}$ erg s^{-1} in the range of 6–13.6 eV, while the X-ray luminosity is set to be $\sim 10^{30}$ erg s^{-1} in the range of 0.1–10 keV based on the spectrum observations of TW Hydra (e.g., Herczeg et al., 2002; Kastner et al., 2002). In the model, the dust-to-gas mass ratio is assumed to be 10^{-2} with the dust-size distribution model for dense clouds (Weingartner & Draine, 2001). The resultant (a) gas temperature, (b) dust temperature, (c) number density of gases,

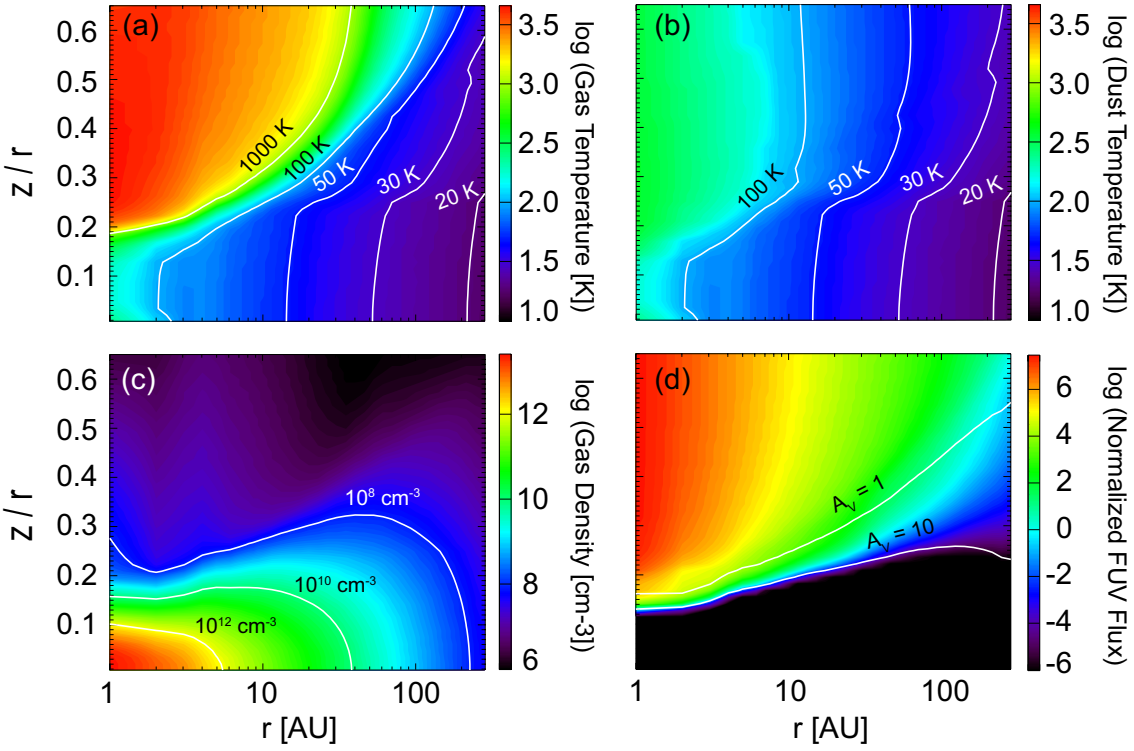

Figure 3.1: Spatial distributions of the (a) gas temperature, (b) dust temperature, (c) number density of gases, and (d) wavelength-integrated FUV flux normalized by Draine field (1.6×10^{-3} erg cm^{-2} s^{-1}; Draine, 1978). In panel (d), the solid lines indicate the height at which the vertical visual extinction of interstellar radiation field reaches unity and ten.

and (d) wavelength-integrated FUV flux normalized by Draine field (Draine, 1978) are shown in Figure 3.1.

3.3 Chemical model

We use a two-phase (gas and grain surface) model to compute disk chemistry (Hasegawa et al., 1992). Our chemical reaction network is based on Aikawa et al. (2012), who investigated deuterium fractionation in the star formation from a prestellar core to a protostellar core. They extended the network of Garrod & Herbst (2006) to include multi deuterated species and isotope exchange reactions from Millar et al. (1989) and Roberts et al. (2004). More detailed explanation can be found in Aikawa et al. (2012). To reduce the computational time, we exclude the species with chlorine and phosphorus, molecules with more than four carbon atoms, and relevant reactions. We also make several modifications to make the network model applicable to disk

Table 3.2: Formation Reactions of Water and Its Isotopologues at High Temperatures.

Reaction							α	β	γ	Reference
O	+	H_2	$\rightarrow$	OH	+	H	3.44(-13)	2.67	3.16(3)	1
O	+	HD	$\rightarrow$	OH	+	D	9.01(-13)	1.90	3.73(3)	2
			$\rightarrow$	OD	+	H	1.57(-12)	1.70	4.64(3)	2
O	+	D_2	$\rightarrow$	OD	+	D	1.57(-12)	1.70	4.64(3)	3
OH	+	H_2	$\rightarrow$	H_2O	+	H	2.05(-12)	1.52	1.74(3)	1
OH	+	HD	$\rightarrow$	H_2O	+	D	2.12(-13)	2.70	1.26(3)	4
			$\rightarrow$	HDO	+	H	6.00(-14)	1.90	1.26(3)	4
OH	+	D_2	$\rightarrow$	HDO	+	D	3.24(-13)	2.73	1.58(3)	5
OD	+	H_2	$\rightarrow$	HDO	+	H	2.05(-12)	1.52	1.74(3)	3
OD	+	HD	$\rightarrow$	HDO	+	D	2.12(-13)	2.70	1.26(3)	3
			$\rightarrow$	D_2O	+	H	6.00(-14)	1.90	1.26(3)	3
OD	+	D_2	$\rightarrow$	D_2O	+	D	3.24(-13)	2.73	1.58(3)	3

chemistry, which are described below.

In the regions where the gas temperature exceeds 100 K, we use the reaction set based on Harada et al. (2010) instead of those of Garrod & Herbst (2006) for the neutral-neutral and neutral-ion reactions. The network of Harada et al. (2010) was designed for modeling high-temperature gas phase chemistry (100–800 K). This switching method of the reaction sets was also used in Furuya et al. (2012) to simulate the chemical evolution in collapsing molecular cloud cores. For high temperature reactions of water and its isotopologues, we adopt the rates in Talukdar et al. (1996), Bergin et al. (1999), and the UMIST database (Woodall et al., 2007). They are summarized in Table 3.2. We include some three-body association reactions and the reverse reactions (i.e. collisional dissociation) based on Willacy et al. (1998) and Furuya et al. (2012). We also modify or include the following reactions, which are important for disk chemistry: (i) X-ray chemistry (Section 3.3.1 and 3.3.2), (ii) photoreactions by stellar and interstellar UV (Section 3.3.2), (iii) chemistry of vibrationally excited H_2 and its isotopologues (Section 3.3.3). The treatment of gas-grain interactions and grain surface reactions is described in Section 3.3.4. In total, our reaction network consists of 726 gaseous species, 303 grain-surface species, dust grains with three different charge states (±1, 0), and 34,997 (38,162) reactions for gas temperatures $\leq$100 K (>100 K).

3.3.1 Ionization rate

Interstellar cosmic-rays and X-rays from a central star are the main ionization sources of protoplanetary disks. The cosmic-ray ionization rate of hydrogen molecules is expressed as

$$\xi_{\rm CR}(r,z) = \frac{\xi^0_{\rm CR}}{2}\left[\exp\left(-\frac{\Sigma_1(r,z)}{96\,{\rm g\,cm^{-2}}}\right) + \exp\left(-\frac{\Sigma_2(r,z)}{96\,{\rm g\,cm^{-2}}}\right)\right], \tag{3.1}$$

where $\Sigma_1(r,z)$ and $\Sigma_2(r,z)$ are the vertical column density of gas measured from the upper and lower boundary of the disk to the height z, respectively (e.g., Semenov et al., 2004). Unattenuated cosmic-ray ionization rate, $\xi^0_{\rm CR}$, is set to be 5×10^{-17} s^{-1} (Dalgarno, 2006). The attenuation length of cosmic-ray is 96 g cm^{-2} (Umebayashi & Nakano, 1981), which is larger than our disk column density only at $r \lesssim 1$ AU. We also take into account the ionization by short-lived radio active isotopes with the rate of 1×10^{-18} s^{-1} (Umebayashi & Nakano, 2009).

The primary ionization rate of species i by X-rays is given by

$$\xi_{{\rm prim},i}(r,z) = \int F_{\rm X}(E,r,z)\sigma_{{\rm pi},i}(E)dE, \tag{3.2}$$

where $F_{\rm X}$ is the photon number flux from the central star. The photoionization cross sections, $\sigma_{{\rm pi},i}$, are taken from Verner & Yakovlev (1995). We consider the primary ionization of atoms, singly ions, and diatomic molecules. Considering the Auger effect, it is assumed that ionization of atoms leads to doubly charged ions, while ionization of diatomic molecules produces a pair of singly charged ions, following Maloney et al. (1996). The cross sections of the molecules are calculated by adding the atomic cross sections. We use the same cross sections for deuterated species as normal isotopes. Electron recombination and charge transfer reactions for doubly ionized species are taken from Stäuber et al. (2005). We neglect doubly ionized states of Na and Mg, since the elemental abundances of Na (2.25×10^{-9}) and Mg (1.09×10^{-10}) are low in our model. We also neglect doubly ionized state of Si, since its abundance is much lower than that of Si^+ in PPDs (e.g., Ádámkovics et al., 2011).

Part of the kinetic energy of photoelectrons produced by primary ionization is lost by ionizations of H, H_2, and He. These secondary ionizations are far more important for the ionization degree of gas than the primary ionization. Assuming that the kinetic energy of Auger electrons is equal to the photoionisation threshold energy (Voit, 1991), the overall secondary ionization rate per hydrogen nucleus is

$$\xi_{\rm sec}(r,z) = \sum_i \int F_{\rm X}\sigma_{\rm eff}(E)\frac{E}{W_i(E)}dE, \tag{3.3}$$

where $\sigma_{\rm eff}$ ($= \sum_i x_i^{\rm cosmic} \sigma_{{\rm pi},i}$) is the effective photoionization cross section per hydrogen nucleus evaluated assuming a cosmic abundance for elements ($x_i^{\rm cosmic}$). Dalgarno et al. (1999) derived the mean energy required per secondary ionization of species i, W_i, for the H-H_2-He mixtures as a function of the ionization degree and the abundance ratio of H and H_2. We use Equations (9), (10), (13) and (15) of Dalgarno et al. (1999) with the parameter applicable to a 1 keV electron to calculate W in our models (e.g., Meijerink & Spaans, 2005). Although secondary ionizations of other species have no significance for the ionization degree of gas, it could be important for chemistry (Maloney et al., 1996). The secondary ionization rate of other species i per hydrogen nucleus is estimated by

$$\xi_{{\rm sec},i} = \xi_{\rm sec} \frac{x_i \sigma_{{\rm ei},i}}{x_{\rm H}\sigma_{\rm ei,H} + x_{\rm H_2}\sigma_{\rm ei,H_2} + x_{\rm He}\sigma_{\rm ei,He}}, \tag{3.4}$$

where x_i represent the abundance of species i relative to hydrogen nuclei. The electron impact cross sections, $\sigma_{\rm ei}$, are taken from the NIST database (http://www.nist.gov/pml/data/ion
and Lennon et al. (1988). We include secondary ionization of CO, singly charged atomic ions, and atoms except for H and He in our network using Equation (3.4). In our disk models, the secondary ionization by X-rays is the dominant ionization source except for the midplane (e.g., $N_{\rm H} \gtrsim 10^{24}$ cm^{-2} at 5 AU, where $N_{\rm H}$ is the vertical column density of hydrogen nucleus from the disk surface.), where cosmic ray ionization is dominant.

3.3.2 Photochemistry

Protoplanetary disks are irradiated by UV photons from interstellar radiation and central stars. While the former has a continuous spectral energy distribution, the latter is the combination of continuum and Lyα radiation. Furthermore, cosmic-rays and X-rays induce UV photons through energetic photoelectrons. The UV spectrum at each point in the disk is given as a combination of them. Because of the different origins and wavelength dependence, photochemistry by these photons is considered separately. In this subsection, rate coefficients (s^{-1}) are denoted by k, while photorates (cm^{-3} s^{-1}) are denoted by R.

UV continuum

Spectral energy distribution of UV continuum is given at each point in the disk (Section 3.2). To calculate photorates, we convolve the UV spectrum with absorption cross sections. Referring to van Dishoeck (1988), the rate coefficients of photodisso-

ciation and photoionization in the gas phase (s^{-1}) are calculated as

$$k_{\mathrm{phg},i}(r,z) = \int 4\pi J(\lambda,r,z)\sigma_i(\lambda)d\lambda, \tag{3.5}$$

where $J(\lambda)$ is the the mean intensity of the radiation field measured in photons cm^{-2} s^{-1} $Å^{-1}$ str^{-1} at the wavelength of λ. The cross sections, $\sigma(\lambda)$, are given by van Dishoeck (1988), and updated by Jansen et al. (1995a,b) and van Dishoeck et al. (2006). The data is downloadable from http://www.strw.leidenuniv.nl/~ewine/photo/. For deuterated species, we use the same cross sections as normal species. For species which are not in the database, we use the cross sections of a similar type of species (e.g., van Zadelhoff et al., 2003).

H_2, HD, and CO are dissociated by absorption lines. Because of their high abundances, self-shielding and mutual shielding of HD and CO by H_2 are important. The self-shielding factor of H_2 is given as a function of H_2 column density referring to Equation (37) of Draine & Bertoldi (1998). Since the self-shielding behavior of HD is almost identical to that of H_2 (Wolcott-Green & Haaiman, 2011), we also use Equation (37) of Draine & Bertoldi (1998) for self-shielding factor of HD by replacing H_2 column density with that of HD. The shielding factor of HD by H_2 is given by Equation (12) of Wolcott-Green & Haaiman (2011). For CO, the self-shielding and mutual shielding factors are calculated following Lee et al. (1996).

Then, the photodissociation rate coefficient of CO, for example, is calculated as follows:

$$k_{\mathrm{phg}}(r,z) = k^0_{\mathrm{phg},r} f_{\mathrm{sh}}(N_{r,\mathrm{CO}}, N_{r,\mathrm{H_2}}) + k^0_{\mathrm{phg},z} f_{\mathrm{sh}}(N_{z,\mathrm{CO}}, N_{z,\mathrm{H_2}}), \tag{3.6}$$

where $k^0_{\mathrm{phg},r}$ and $k^0_{\mathrm{phg},z}$ are non-shielding photodissociation rates of CO, which are calculated at each point using Equation (3.5), by the UV radiation in the radial and vertical directions, respectively. The shielding factor, f_{sh}, is a function of the column densities of CO and H_2, N_{CO} and $N_{\mathrm{H_2}}$, along the ray. In the vertical direction, we obtain the shielding factor at each vertical position z by integrating the number density of CO and H_2 at $>z$,

$$N_{z,i}(r,z) = \int_z^\infty n_i dz', \tag{3.7}$$

where n_i represents the number density of species i. In the radial direction, on the other hand, molecular column densities are assumed to be the overall column density along the ray multiplied by the local molecular abundances:

$$N_{r,i}(r,z) = x_i(r,z) \int_{R_*}^r n_{\mathrm{H}} dr', \tag{3.8}$$

where $n_{\rm H}$ represent the number density of hydrogen nuclei. Equation (3.8) could overestimate the column densities (i.e. shielding factors), since the radiation field decays and the abundances of CO and H_2 would increase along the ray.

Grain surface species are also photodissociated and photodesorbed by UV photons (e.g., Gerakines et al., 1996; Westley et al., 1995). The photoabsorption cross sections of H_2O ice and CO_2 ice are taken from Mason et al. (2006). It is worth noting that the cross sections of ices are different from those in the gas phase (see Figure 1 of Andersson & van Dishoeck, 2008, for water). For the other species, we use the same cross section for corresponding gaseous species, because data is not available in the literature. We confirmed that our results are not sensitive to this assumption. We performed a calulation using the ten times smaller cross sections for ice molecules except for water and CO_2 ices, and found that the results are not significantly different from those in Section 3.4. The photodissociation rates on grain surfaces ($\rm cm^{-3}\ s^{-1}$) are calculated as

$$R_{{\rm phs},i}(r,z) = \pi a^2 n_{\rm d} \theta_i \int 4\pi J(\lambda, r, z) P_i(\lambda) d\lambda, \tag{3.9}$$

$$\theta_i = \frac{n_i}{\max(n_{\rm ice}, n_{\rm d} N_{\rm site})}, \tag{3.10}$$

$$P_i(\lambda) = \min\left(1, \frac{N_{\rm p}\sigma_i(\lambda)}{\sigma_{\rm site}}\right), \tag{3.11}$$

where $n_{\rm d}$, $n_{\rm ice}$, θ_i, and, $N_{\rm site}$ are the number density of the grain, the total number density of grain surface species, the coverage of species i on a grain, and the number of adsorption sites on a grain ($N_{\rm site} \sim 10^6$), respectively. The grain radius, a, is set to be 0.1 μm in our chemical model for simplicity. The ratio of the geometrical and absorption cross sections of dust grains for FUV photons is assumed to be unity (e.g., Tielens, 2005). $P_i(\lambda)$ and $\sigma_{\rm site}$ are the probability for an incident photon with the wavelength of λ on a site to be absorbed by an adsorbed species and the site size ($4\pi a^2/N_{\rm site}$), respectively.

Every photoabsorption does not necessarily result in photodissociation. Andersson et al. (2006) and Andersson & van Dishoeck (2008) carried out molecular dynamics simulations to study photodissociation of water ice in the top six monolayers. They found that photolytic effect is more significant in the uppermost few monolayers; although photons can penetrate into deeper layers and dissociate embedded molecules, the photoproducts recombine with a higher probability than in uppermost layers. In this study, we assume that the upper most one monolayer can be dissociated as the outcome of photoabsorption, and that the photoproducts immediately recombine in deeper layers. For considering surface roughness, parameter $N_{\rm p}$ in Equation (3.9) is set to be two monolayers for all species. We discuss the effect of

this assumptions on our results in Section 3.5.2.

In this study, we adopt a two-phase model, in which a layered structure of ice mantles is not considered and the bulk of ices is chemically active. More sophisticated ice mantle modeling, which distinguish a chemically active surface layer from an inactive inert bulk, has been developed (Hasegawa & Herbst, 1993; Taquet et al., 2013b). Since the calculation of the rate equations combined with turbulent mixing is time consuming, we postpone the inclusion of such layered ice structure to future works. The combination of the two-phase model and photodissociation of HDO ice could, however, introduce artificial decrease of the D/H ratio of water ice as follows. Photodissociation of HDO ice has two branches, producing OH ice or OD ice. While OH ice is able to cycle back to HDO ice via the grain surface reactions, e.g., OH_{ice} + D_{ice}, it is also converted to H_2O ice. If photodissociation of ices is efficient only in the uppermost several layers, this cycle could decrease the D/H ratio of water ice on the surface, but not the ratio in the bulk water ice. In the two phase model, on the other hand, this cycle could decrease the D/H ratio in the bulk water ice; we do not distinguish between D/H ratios in the surface layers and the deeper layers, although we calculate the photodissociation rate of ice assuming that only the uppermost one layer can be dissociated. To keep the consistency in our model, we switch off the branch to produce OH ice in photodissociation of HDO ice.

The photodesorption rates are calculated as (e.g., Visser et al., 2011)

$$R_{\mathrm{pd},i}(r,z) = \pi a^2 n_{\mathrm{d}} \theta_i F_{\mathrm{FUV}}(r,z) Y_i, \tag{3.12}$$

where F_{FUV} and Y_i are the FUV photon number flux integrated in the range of 912–2000 Å and the photodesorption yield per incident FUV photon, respectively. Some experiments into the photodesorption of UV-irradiated ices have been conducted (e.g., Westley et al., 1995; Öberg et al., 2007). Recently, Öberg et al. (2009a,b) measured the yield of CO_2 and H_2O ices by photons with the wavelength of 1180–1770 Å. Fayolle et al. (2011, 2013) measured wavelength-dependent photodesorption yields of CO, O_2, and N_2 ices, and calculated the yields adequate for astrophysical environments. For the above species, we use the yields obtained by the experimental works. The yield for the other species is assumed to be 10^{-3}. We confirmed that the results presented in this paper does not change, if we use the yield of 10^{-4} for species without laboratory data.

Lyα photons

Lyα radiation could dominate the UV field in protoplanetary disks (Herczeg et al., 2004). We include photoreactions by Lyα photons for a limited number of gaseous species, for which photodissociation cross section at Lyα wavelength ($\sim$1216 Å) is

available in van Dishoeck et al. (2006), and corresponding species in the solid phase. The cross sections for H_2O ice and CO_2 ice are taken from Mason et al. (2006), while we use the cross section of the gaseous species for the other ice-mantle species. Considering that the photodissociation of ice-mantle species causes photodesorption (Andersson & van Dishoeck, 2008), the photodesorption yields per incident Lyα photon, $Y_{\mathrm{Ly}\alpha}$, are estimated by

$$\frac{Y_{\mathrm{Ly}\alpha,i}}{Y_i} = \frac{\sigma_i(\lambda_{\mathrm{Ly}\alpha})}{\tilde{\sigma}_i}, \tag{3.13}$$

where $\sigma_i(\lambda_{\mathrm{Ly}\alpha})$ and $\tilde{\sigma}_i$ are the photodissociation cross section at Lyα wavelength and the averaged cross section in the wavelength of 1180–1770 Å, respectively.

Recently, Bethell & Bergin (2011) showed that the Lyα/FUV-continuum photon density ratio is smaller in the regions near the photodissociation layers for hydrogen ($N_{\mathrm{H}} \lesssim 5 \times 10^{20}$ cm^{-2} at 1 AU if the dust is well mixed with gas), but larger in the deeper regions than the intrinsic ratio in the incident FUV radiation from the central star, due to resonant scattering of Lyα by atomic hydrogen. Since the intensity of Lyα radiation is calculated without considering resonant scattering in the physical model used here, it would be overestimated in the upper layers of the disk, and underestimated near the midplane.

Cosmic-ray and X-ray induced UV photons

UV photons are generated by the decay of electronically excited hydrogen molecules and atoms produced by collisions with energetic photoelectrons following cosmic-ray ionization. In dense regions where the stellar and interstellar UV photons are heavily attenuated, cosmic-ray induced photons dominate the UV fields (Prasad & Tarafdar, 1983). X-ray ionization also induces UV photons in a similar manner. Our model includes photochemistry by cosmic-ray and X-ray induced UV photons both in the gas phase and on grain surfaces. The rates are described by the local competition of photon absorption by gaseous species and dust grains. Referring to Gredel et al. (1989), the rate coefficients of photodissociation and photoionization of species i in the gas phase (s^{-1}) are expressed as

$$k_{\mathrm{crphg},i}(r,z) = x_{\mathrm{H_2}} \xi_{\mathrm{T}} \int \frac{\sigma_i(\lambda)}{\sigma_{\mathrm{tot}}} \psi(\lambda) d\lambda, \tag{3.14}$$

$$\sigma_{\mathrm{tot}} = x_{\mathrm{d}} \pi a^2, \tag{3.15}$$

$$\xi_{\mathrm{T}} = \xi_{\mathrm{CR}} + \xi_{\mathrm{sec}}/x_{\mathrm{H_2}}, \tag{3.16}$$

where $\psi(\lambda)$, and $x_{\rm d}$ are the number of photons with the wavelength of λ produced per ionization, and the relative abundance of dust grains to hydrogen nucleus ($\sim 2 \times 10^{-12}$), respectively. Again, the ratio of the geometrical and absorption cross sections of dust grains for FUV photons is assumed to be unity (e.g., Tielens, 2005). For simplicity, we ignore photons produced by the de-excitation of atomic hydrogen and assume $x_{\rm H_2} = 0.5$ in Equation (3.14). It is an acceptable assumption, since the regions dominated by atomic hydrogen do not contain many molecules (Aikawa & Herbst, 1999). We also ignore the gas opacity in Equation (3.15). If all oxygen is in gaseous water, the latter assumption overestimates the rate coefficients by a factor of about two at maximum, since $x_{\rm H_2O}\tilde{\sigma}_{\rm H_2O}$ is $\sim 7 \times 10^{-22}$ cm^{-2} and $x_{\rm d}\pi a^2$ is $\sim 6 \times 10^{-22}$ cm^{-2}. However, it is also acceptable, since induced UV photons are more important than stellar UV photons only near the midplane, and dust temperatures near the midplane in our disk models are lower than the sublimation temperature of water ice except for $r \lesssim 1$ AU.

The rates (cm^{-3} s^{-1}) of photodissociation on grain surfaces and photodesorption are calculated by

$$R_{{\rm crphs},i}(r,z) = n_{\rm H_2}\xi_{\rm T}\theta_i \int \psi(\lambda) P_i(\lambda) d\lambda, \tag{3.17}$$

$$R_{{\rm crpd},i}(r,z) = n_{\rm H_2}\xi_{\rm T}\theta_i Y_i \int \psi(\lambda) d\lambda. \tag{3.18}$$

Photoreaction timescales in the disk

Figure 3.2 shows the timescales of photoreactions of water ice and water vapor as a function of vertical column density in our disk model at $r = 10$ AU. Here, the photoreaction timescales of water ice are defined as the timescales in which one monolayer of pure water ice is photodissociated (photodesorbed), $n_{\rm d}N_{\rm site}/R(\theta_{\rm H_2O_{ice}} = 1)$, while those of water vapor are defined as an inverse of the rate coefficients, k^{-1}. It is clear that the photoreactions by Lyα photons are most efficient in the disk atmosphere, while the photoreactions by X-ray and cosmic-ray induced UV photons are the most efficient at $N_{\rm H} \gtrsim 2 \times 10^{22}$ cm^{-2} at 10 AU. It should be noted, however, that these timescales are larger than the typical age of T Tauri stars ($\sim 10^6$ yr) at $N_{\rm H} \gtrsim 10^{23}$ cm^{-2}.

3.3.3 Vibrationally excited hydrogen molecule

Hydrogen molecules can be electronically excited by absorbing FUV photons. Subsequent fluorescence leads to dissociation or to the population of various rotation-vibration levels in the ground electronic state. The branching ratio of the former and

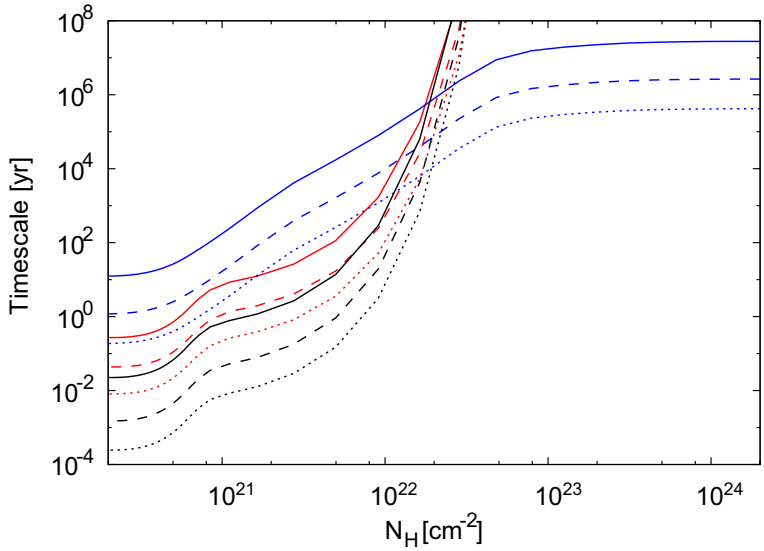

Figure 3.2: Timescales of photoreactions of water ice and water vapor as functions of vertical column density in our disk model at $r = 10$ AU. The solid, dashed, and dotted lines indicate timescales of photodesorption, photodissociation on grain surfaces, and photodissociation in the gas phase, respectively. The black, red, and blue lines indicate photoreactions by Lyα photons, FUV continuum, and X-ray and cosmic-ray induced photons, respectively.

latter are 10 % and 90 %, respectively (Black & Dalgarno, 1976). Following Tielens & Hollenbach (1985), we consider only two states of H_2, the ground vibrational state and a single vibrationally excited state (H_2^*). They are treated as different species in our chemical model. The effective quantum number of this pseudolevel is $v = 6$, and the effective energy is 2.6 eV ($\sim 3 \times 10^4$ K, London, 1978). The FUV pumping rate is set to be 9 times the photodissociation rate of H_2. H_2^* can be destroyed by photodissociation, radiative decay, collisional de-excitation, or collisional dissociation. These rates are calculated following Tielens & Hollenbach (1985). As an inverse reaction of the collisional de-excitation, we consider collisional excitation following Woitke et al. (2009a).

H_2^* reacts with other species using internal energy to overcome activation barriers. It should be noted, however, that whether the internal energy of H_2^* is effectively used or not is quite specific for each reaction and difficult to predict as discussed by Agúndez et al. (2010). Therefore, it would be problematic to simply assume that all the internal energy of H_2^* is used to overcome activation barriers in any reactions. To be conservative, we include a limiting number of reactions between H_2^* and other species (He^+, C^+, O, OH, and CN), rate coefficients of which are experimentally or/and theoretically determined (see Table 1 of Agúndez et al., 2010). Vibrationally

Table 3.3: Desorption Energy of Selected Species.

Species	$E_{\rm des}$ [K] [1]	Species	$E_{\rm des}$ [K]
H_2	430	NO	1600
H	450	HNO	2050
H_2O	5700	CO	1150
OH	2850	CO_2	2650
O	800	H_2CO	2050
O_2	1000		

excited HD and D_2 are treated in the same way as H_2^*.

3.3.4 Gas grain interactions and surface reactions

Calculations of gas-grain interactions and grain-surface reactions except for H_2 formation are performed in a similar way to Garrod & Herbst (2006) and Furuya et al. (2012). A brief summary is provided below.

The sticking probability of neutral species onto dust grains is assumed to be unity except for atomic hydrogen and deuterium; their sticking probabilities are calculated as a function of gas and dust temperatures following Hollenbach & Mckee (1979). Interactions between ions and dust grains are calculated in the same way as Furuya et al. (2012). We adopt the same desorption energies ($E_{\rm des}$) of atoms and molecules as Garrod & Herbst (2006), in which grain-surfaces are assumed to be covered with non-porous water ice, and thus only physisorption sites are considered, unless stated otherwise. For deuterated species, we use the same desorption energies as normal species except for atomic deuterium, whose adsorption energy is set 21 K higher than that of atomic hydrogen, following Caselli et al. (2002). $E_{\rm des}$ of selected species are listed in Table 3.3. In addition to the thermal desorption and photodesorption (see Section 3.3.2), we consider sublimation via stochastic heating by cosmic-ray (Hasegawa & Herbst, 1993) and X-ray, and the chemical desorption. We assume that roughly 1% of species formed by surface reactions are desorbed following Garrod et al. (2007).

Grain surface reactions are assumed to occur by the Langmuir-Hinshelwood (LH) mechanism between physisorbed species; adsorbed species diffuse by thermal hopping and react with each other when they meet (e.g., Hasegawa et al., 1992). The energy barrier against diffusion is set to be a half of the desorption energy. If surface reactions have activation energy barriers, they are overcome thermally, or via quantum tunneling, whichever is faster (Garrod & Herbst, 2006). We use the modified rate method (Caselli et al., 1998) for surface reactions which include atomic hydrogen or

deuterium as reactants.

In our disk models, H_2 formation by association of physisorbed H atoms does not efficiently occur by the LH mechanism, since the dust temperatures are $\gtrsim$20 K except for the midplane at $r \gtrsim 250$ AU (e.g., Hollenbach & Salpeter, 1971). Cazaux & Tielens (2004, 2010) and Cazaux et al. (2008) studied formation of H_2 and its isotopologues on *bare* grain surfaces, considering both physisorbed and chemisorbed sites and both the LH and Eley-Rideal mechanisms. They showed that H_2 and HD can be formed with the efficiency of several tens of percent until quite high temperatures (several hundreds K). Since the abundance of water in disk atmospheres is highly dependent on the abundance of H_2 (e.g., Glassgold et al., 2009), H_2 formation on bare grain surfaces should be considered. The precise efficiency is, however, highly dependent on the width and height of the barrier between the adsorption sites, which is not well constrained; we adopt a constant efficiency of 0.2 for H_2 and HD independent of dust temperature. We ignore D_2 formation on bare grain surfaces, since it is not as efficient as that of H_2 and HD (Cazaux et al., 2008). Considering the accretion rate of a pair of atomic hydrogen onto bare grain surfaces, the formation rate of H_2 is expressed as

$$R_{\mathrm{H_2}} = \frac{1}{2}\pi a^2 n_{\mathrm{d}} n_{\mathrm{H}} S \varepsilon_{\mathrm{H_2}} (1 - \theta_{\mathrm{ice}}) \sqrt{\frac{8kT_{\mathrm{g}}}{\pi m_{\mathrm{H}}}}, \tag{3.19}$$

where $\varepsilon_{\mathrm{H_2}}$ is the formation efficiency. The coverage of ice mantle species, θ_{ice}, is given by substituting n_{ice} into n_i in Equation (3.10). The rate is set to zero when dust grains are covered by more than one monolayer of ice (i.e. $n_{\mathrm{ice}} \geq n_{\mathrm{d}} N_{\mathrm{site}}$).

3.3.5 Initial abundances for disk chemistry

We adopt the so-called low metal values as the elemental abundances (see Table 1 of Aikawa & Herbst, 2001). The elemental abundance of deuterium is set to be 1.5×10^{-5} (Linsky, 2003). It is assumed that hydrogen and deuterium are initially in H_2 and HD, respectively. The heavy elements are assumed to be initially in atomic or ionic form, corresponding to their ionization energy. We integrate the rate equation, using our chemical network model, in the collapsing core model of Aikawa et al. (2012), in which fluid parcels are traced from the prestellar core to the protostellar core of age 9.3×10^4 yr. Because the abundances are mostly constant at $r \lesssim 100$ AU in this protostellar core model, we adopt the molecular abundances at $r = 60$ AU as the initial abundance of our disk model (Table 3.4).

Table 3.4: Initial Abundances of Selected Species for Our Disk Models.

Species	Abundance[1]	Species	Abundance
H_2	5.0(-1)	NH_3	1.4(-5)
HD	8.0(-6)	NH_2D	5.1(-7)
D_2	9.6(-7)	H_2CO	1.2(-5)
H	3.9(-5)	HDCO	3.0(-7)
D	9.0(-7)	CO	3.6(-5)
H_2O	1.2(-4)	CO_2	3.5(-6)
HDO	2.3(-6)	O_2	8.3(-9)
CH_4	1.5(-5)	O	1.5(-12)
CH_3D	5.8(-7)		

3.3.6 Turbulent mixing

We compute molecular evolution in the protoplanetary disk with vertical mixing, assuming that the origin of the disk turbulence is the magnetorotational instability (MRI; Balbus & Hawley, 1991). We consider the inhomogeneous one-dimensional diffusion equations at a specific radius (e.g., Xie et al., 1995; Willacy et al., 2006),

$$\frac{\partial n_i}{\partial t} + \frac{\partial \phi_i}{\partial z} = P_i - L_i, \tag{3.20}$$

$$\phi_i = -n_{\rm H} \frac{D_z}{Sc} \frac{\partial}{\partial z} \left(\frac{n_i}{n_{\rm H}} \right), \tag{3.21}$$

where P_i, and L_i represent the production rate and the loss rate, respectively, of species i. The second term in the left-hand side of Equation (3.20) describes diffusion in turbulent disks. The vertical diffusion coefficient for gas and very small dust grains (i.e well-coupled to gas) is assumed to be

$$D_z = \langle \delta v_z^2 \rangle / \Omega, \tag{3.22}$$

where Ω is the Keplerian orbital frequency (Fromang & Papaloizou, 2006; Okuzumi & Hirose, 2011). The vertical velocity dispersion, $\langle \delta v_z^2 \rangle$, is assumed to be

$$\langle \delta v_z^2 \rangle = \alpha_z c_s^2(z), \tag{3.23}$$

where c_s is the local sound speed. The Schmidt number (ratio of gas to dust diffusivity) is

$$Sc \sim 1 + (\Omega \tau_{\rm s})^2, \tag{3.24}$$

where $\tau_{\rm s}$ is the stopping time of dust grains (Youdin & Lithwick, 2007). We adopt $Sc = 1$, since the term $\Omega\tau_{\rm s}$ is much less than unity in the midplane of our disk model (e.g., $\sim 10^{-6}$ at $r = 5$ AU). In other words, gaseous species and dust grains (grain surface species) have the same diffusivity. It is worth noting that in our approach, only the mean composition of ice mantle of grains is obtained at each spatial point in the disk. In reality the ice composition could vary among grains in the same spatial grid at a given time, since the motion of grain is random in turbulent gases, and since grains have different thermal and irradiation history (Ciesla & Sandford, 2012).

The activity of MRI depends on the ionization degree. MRI can be stabilized near the midplane of disks, where the ionization degree is low and magnetic field is decoupled to plasma. It is called dead zone (e.g., Gammie, 1996; Sano et al., 2000). Three-dimensional isothermal MHD simulations in the shearing box approximation show $\langle \delta v_z^2 \rangle$ in the dead zone is smaller than that in the MRI active layer by more than one order of magnitude, depending on the strength of the magnetic field (Okuzumi & Hirose, 2011; Gressel et al., 2012). In our fiducial models, however, we assume that α_z is constant for simplicity. We run three models in which α_z is set to be 0, 10^{-3}, and 10^{-2}. The effect of dead zone is discussed in Section 3.5.4.

Equation (3.20) is integrated for 10^6 yr using implicit finite differencing on a linear grid consist of vertical 60 points at a specific radius. Our code is based on Nautilus code (Hersant et al., 2009), but we improved the treatment of turbulent diffusion to account for the full coupling of mixing with chemistry according to Heinzeller et al. (2011). As boundary conditions, we assume that there is no flux through the midplane and the upper boundary of the disk. We integrate Equation (3.20) at 35 radial points from $r = 1$ AU to $r = 300$ AU. We ignore radial accretion and radial mixing in the present study.

3.4 Result

3.4.1 Effect of vertical mixing on oxygen chemistry

Beyond the snow line ($r \gtrsim 1$ AU in our models), the bulk of water exists as ice on grain surfaces. In this subsection, we describe how the vertical mixing affects abundances of oxygen reservoirs beyond the snow line in the disk. As an example, we look into the results at $r = 10$ AU and 30 AU in the model with $\alpha_z = 10^{-2}$. In the following, species X on grain surfaces are denoted as $\rm X_{ice}$.

Figure 3.3 shows physical parameters (top panels), abundances of assorted O-bearing species in the model with $\alpha_z = 0$ (middle panels), and $\alpha_z = 10^{-2}$ (bottom panels) as functions of vertical column density at $r = 10$ AU (left panels) and 30 AU (right panels), at $t = 10^6$ yr. In the model without mixing, the disk can be

divided into two layers in terms of the main oxygen reservoir; atomic oxygen in the disk surface and water ice near the midplane. Above the O/H_2O_{ice} transition, photoreactions on grain surfaces are efficient, and the water ice abundances are low ($<10^{-6}$). Thermal desorption of water ice is not efficient either at $r = 10$ AU or $r = 30$ AU, since dust temperatures are less than the sublimation temperature of water ice ($\sim$150 K) even at the disk surface.

In the model with mixing, water ice is transported to the surface through the O/H_2O_{ice} transition. Such water ice is destroyed by photoreactions to produce atomic oxygen. On the other hand, atomic oxygen is transported to the deeper layers in the disk, and is mainly converted to O_2 at $r = 10$ AU, and CO_2 ice and water ice at 30 AU. Then, the water ice abundance near the midplane decreases with time; it is less than the canonical value of $\sim 10^{-4}$ at 10^6 yr especially at $r = 10$ AU. At $r \gtrsim 40$ AU, on the other hand, water ice abundance is $\sim 10^{-4}$ even in the model with mixing (see Figure 3.5), since most of atomic oxygen is converted back to water ice. The variation of the major O-bearing species, which are (re)formed from the atomic oxygen, partly depends on dust temperatures near the O/H_2O_{ice} transition (strictly speaking the height z^*; see Section 3.4.2), where the conversion of atomic oxygen to other species mainly takes place. In Figure 3.4 we present main formation paths to (re)form O_2, CO_2 ice, and water ice beyond the snow line in our models. We note here that the formation reactions of these species include OH as the reactant:

$$O + OH \rightarrow O_2 + H, \tag{3.25}$$

$$CO_{ice} + OH_{ice} \rightarrow CO_{2ice} + H_{ice}, \tag{3.26}$$

$$H_{ice} + OH_{ice} \rightarrow H_2O_{ice} + H_{ice}. \tag{3.27}$$

$$H_2CO_{ice} + OH_{ice} \rightarrow H_2O_{ice} + HCO_{ice}. \tag{3.28}$$

Reaction (3.25) is a gas-phase reaction, while the others are grain-surface reactions. In order for water ice to be efficiently reformed, OH should be mainly formed on grain surfaces, and water ice formation should be more efficient than CO_2 ice formation.

At $r = 10$ AU, dust temperatures are too high ($\sim$60 K) to effectively form OH on grain surfaces; adsorbed atomic oxygen is likely to be evaporated before it meets other reactive species. Hence, the main formation route of OH from atomic oxygen is the gas phase reactions: radiative association with atomic hydrogen and/or a sequence of ion-neutral reactions, followed by the recombination of H_3O^+ with an electron. In the recombination of H_3O^+ with an electron, the branch to produce OH accounts for 74 % of the total recombination rate (Jensen et al., 2000). Although the recombination of H_3O^+ also has a branch to produce water vapor, it accounts only for 25 % of the total rate. Once OH is formed in the gas phase, it mostly reacts with

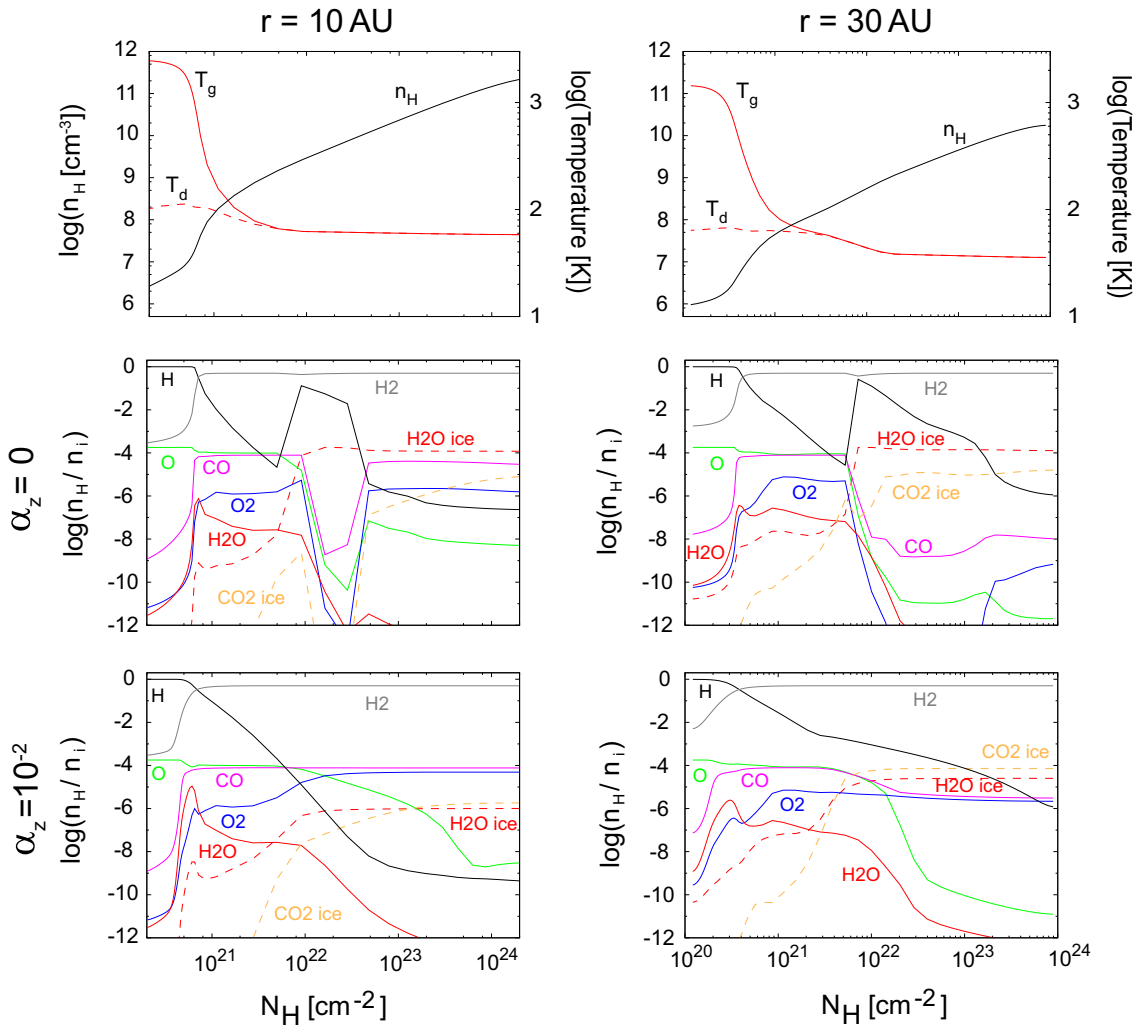

Figure 3.3: Physical parameters (top panels), abundances of selected species in the model with $\alpha_z = 0$ (middle panels), and with $\alpha_z = 10^{-2}$ (bottom panels) as functions of vertical column density at $r = 10$ AU (left panels) and 30 AU (right panels) at $t = 10^6$ yr. The solid lines represent gas-phase species, while the dashed lines represent ice-mantle species.

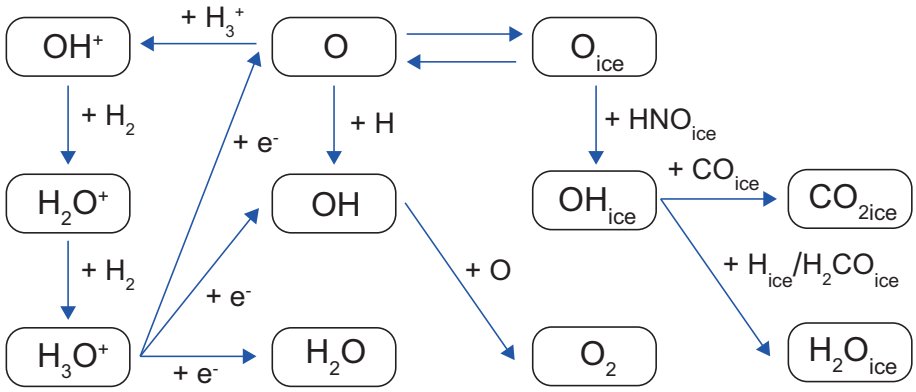

Figure 3.4: Important reaction routes to (re)form water ice, O_2, and CO_2 ice from atomic oxygen beyond the snow line.

atomic oxygen and is converted to O_2 before being adsorbed onto dust grains, due to the high abundance of atomic oxygen ($\gtrsim 10^{-5}$) around the O/H_2O_{ice} transition. The ratio of the O_2 formation rate and adsorption rate of OH is expressed as

$$\frac{k_1 n_O n_{OH}}{\pi a^2 v_{th} n_d n_{OH}} = 400 \left(\frac{x_O}{10^{-5}}\right) \left(\frac{k_1}{4 \times 10^{-11}\ \mathrm{cm^3\ s^{-1}}}\right) \times \left(\frac{a}{0.1\ \mu\mathrm{m}}\right)^{-2} \left(\frac{v_{th}}{10^4\ \mathrm{cm\ s^{-1}}}\right)^{-1} \left(\frac{x_d}{10^{-12}}\right)^{-1}, \tag{3.29}$$

where k_1, the rate coefficient of OH + O, is 4×10^{-11} cm^3 s^{-1} independent of the gas temperature. Then, the conversion to O_2 is dominant. Although the value of k_1 has some uncertainties (2–8$\times 10^{-11}$ cm^3 s^{-1}) according to KIDA (http://kida.obs.u-bordeaux1.fr; see also Wakelam et al., 2012; Hincelin et al., 2011), the ratio exceeds unity even if we use the lowest value. We note that conversion of O_2 to water on grain surfaces ($O_{2ice} \xrightarrow{H_{ice}} HO_{2ice} \xrightarrow{H_{ice}} H_2O_{2ice} \xrightarrow{H_{ice}} H_2O_{ice}$) (Miyauchi et al., 2008) is not efficient due to high dust temperature. Another reason for the high abundance of O_2 is that its destruction rate by UV photons is small compared to that of water ice, since Lyα cross section of O_2 is lower than that of water ice by about two orders of magnitude (van Dishoeck et al., 2006; Mason et al., 2006).

At $r \gtrsim 30$ AU, lower dust temperatures ($\lesssim$40 K) allow OH to mainly form on grain surfaces. Water ice is mainly formed by H_{ice} + OH_{ice} at $r \lesssim 30$–40 AU. CO and atomic hydrogen are mostly in the gas phase at these radii. Since CO has a higher desorption energy than atomic hydrogen (Table 3.3), adsorbed CO stays for a longer time on grain surfaces andCO_{ice} + OH_{ice} proceeds faster than H_{ice} + OH_{ice}. CO_2 ice has a smaller photoabsorption cross section than that of water ice, which further ensures the high abundance of CO_2 ice at $r \sim 30$ AU. H_2CO has a higher

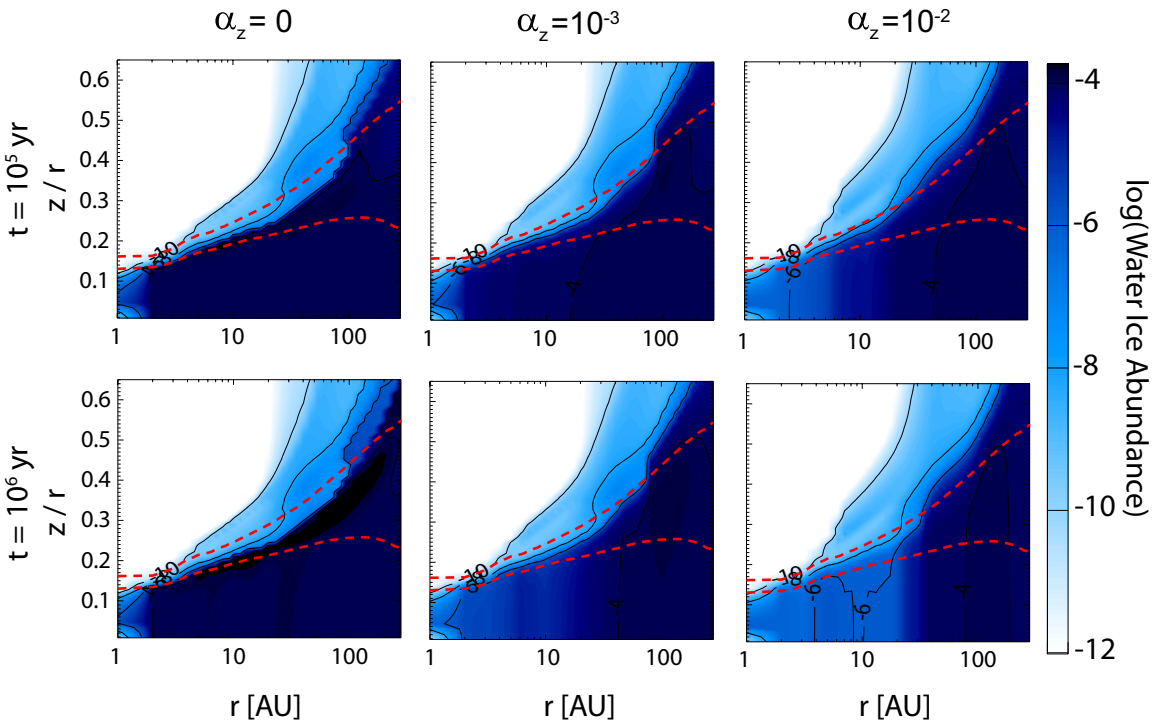

Figure 3.5: Spatial distributions of water ice abundance in the model with $\alpha_z = 0$ (left panels), 10^{-3} (middle panels), and 10^{-2} (right panels) at 10^5 yr (top panels) and 10^6 yr (bottom panels). The vertical axes represent height normalized by the radius. The dashed lines indicate vertical visual extinction of unity and ten.

desorption energy than CO, and mostly exists as ice at $r \gtrsim 30$ AU. At $r \gtrsim 40$ AU, $H_2CO_{ice} + OH_{ice}$ is more efficient than $H_{ice} + OH_{ice}$ and $CO_{ice} + OH_{ice}$, due to high abundance of H_2CO ice near the O/H_2O_{ice} transition ($\gtrsim 10^{-8}$).

Figure 3.5 shows two-dimensional distributions of the abundance of water ice, while Figure 3.6 shows radial distributions of its column density. In the model without mixing, the water ice abundance beyond the snow line stays constant. In the model with mixing, the water ice abundance near the midplane decreases. The tendency is more significant at smaller radius, since reformation of water ice is prohibited by high dust temperatures, and since the timescale of mixing is small (see Section 3.4.2 for quantitative discussions).

Above the O/H_2O_{ice} transition, a fraction of oxygen exists as water vapor, and its abundance reaches a maximum near the H/H_2 transition. In the regions with the gas temperature $T \gtrsim 300$ K, water vapor is formed via the neutral-neutral reaction

$$OH + H_2 \rightarrow H_2O + H, \tag{3.30}$$

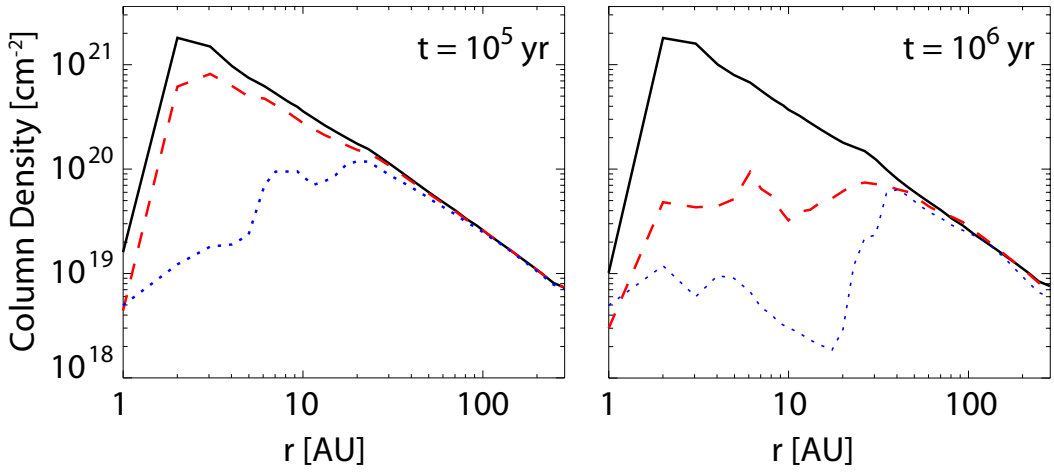

Figure 3.6: Radial distributions of water ice column density at 10^5 yr (left panel) and 10^6 yr (right panel) in the model with $\alpha_z = 0$ (solid lines), 10^{-3} (dashed lines), and 10^{-2} (dotted lines).

which has the potential energy barrier of 1740 K. Water vapor is also formed by a sequence of ion-neutral reactions, followed by the recombination of H_3O^+ with an electron, which is the dominant formation path in the regions with gas temperature $T \lesssim 300$ K.

In the model without mixing, we can see the local bumps of the abundances of atomic hydrogen at $N_H \sim 10^{22}$ cm^{-2}. The positions correspond to where dust grains start to be covered with ice and chemisorption sites become unavailable (i.e. formation rate of hydrogen molecule on grain surfaces decreases). These bumps are smoothed out via mixing. In the model with mixing, peak abundance of water vapor is enhanced in the disk atmosphere, since the H_2 abundance above the H/H_2 transition increases (Reaction 3.30; see also Heinzeller et al., 2011).

3.4.2 Destruction timescale of water ice

When turbulence exists, water ice near the midplane is destroyed via the combination of vertical mixing and photoreactions. This process significantly changes oxygen chemistry as mentioned above. The destruction timescale of water ice would be determined by the timescale of vertical transport via mixing, which in turn, can be estimated from the column density of water ice divided by the upward flux $\phi_{H_2O_{ice}}(z^*)$:

$$\tau^{\rm mix}_{H_2O_{ice}} = \frac{N_{H_2O_{ice}}}{\phi_{H_2O_{ice}}(z^*)}. \tag{3.31}$$

We define z^* as the height where $\partial\phi/\partial z$ reaches a minimum (i.e. where the net upward flux of water ice reaches a maximum). We note that the precise evaluation of the timescale requires the solution of Equation (3.20), since the flux ϕ is proportional to the composition gradient. We evaluate $\tau^{\rm mix}_{\rm H_2O_{ice}}$ using our numerical data at $t = 10^4$ yr in the model with mixing. The upper panel of Figure 3.7 shows temporal variation of water ice abundance in the model with $\alpha_z = 10^{-2}$ at the midplane of $r = 5$ AU and 10 AU. It shows that the water ice abundance at the midplane at $t <$ a few 10^5 yr in the numerical simulations are well reproduced by the exponential decay:

$$x_{\rm H_2O_{ice}}(t) = x_{\rm H_2O_{ice}}(t=0) \exp\left(-\frac{t}{\tau^{\rm mix}_{\rm H_2O_{ice}}}\right). \tag{3.32}$$

It ensures that $\tau^{\rm mix}_{\rm H_2O_{ice}}$ represents the characteristic timescale of destruction of water ice. At $t >$ a few 10^5 yr, the water ice abundance is significantly low compared to the initial value, and destruction and formation almost balance. The lower panel of Figure 3.7 is similar to the upper panel, but shows the results at $r = 30$ AU and 50 AU. At these radii, Equation (3.32) is no more valid, since water ice reformation is not negligible, although Equation (3.31) should be still valid.

We can estimate the destruction timescale of HDO ice from Equation (3.31), but with the subscript replaced by HDO ice. We find that the timescales of HDO ice and H_2O ice are similar, because their chemistry is similar. For example, $\tau^{\rm mix}_{\rm H_2O_{ice}}$ and $\tau^{\rm mix}_{\rm HDO_{ice}}$ are 6.3×10^4 yr and 5.7×10^4 yr, respectively, at $r = 10$ AU. Then we simply denote them as $\tau^{\rm mix}$ in the rest of the paper.

In Figure 3.8, we present radial variations of $\tau^{\rm mix}$. We fit the numerical data at 2 AU $\lesssim r \lesssim$ 100 AU and find that $\tau^{\rm mix}$ depends almost linearly on the radial distance from the central star:

$$\tau^{\rm mix}(r) \sim 6 \times 10^4 \left(\frac{r}{10\,{\rm AU}}\right) \left(\frac{\alpha_z}{10^{-2}}\right)^{-0.8} \ {\rm yr} \quad (2\,{\rm AU} \lesssim r \lesssim 100\,{\rm AU}). \tag{3.33}$$

The timescale is smaller in the inner regions. At $r \gtrsim 100$ AU, destruction timescale is not determined by $\tau^{\rm mix}$, since photoreactions rather than the upward transport of water ice limits the destruction rate, which is clear from the flat distribution of water ice abundance in the vertical direction (Figure 3.5).

3.4.3 Deuteration of water ice

We describe how the vertical mixing affects deuterium chemistry, focusing on the largest deuterium reservoir, HD. In our initial abundance for the disk model, which is set by the collapsing core model, ∼30 % of deuterium is in species other than HD and D_2 (Table 3.4). For example, ∼15 % of deuterium is in water, and its D/H

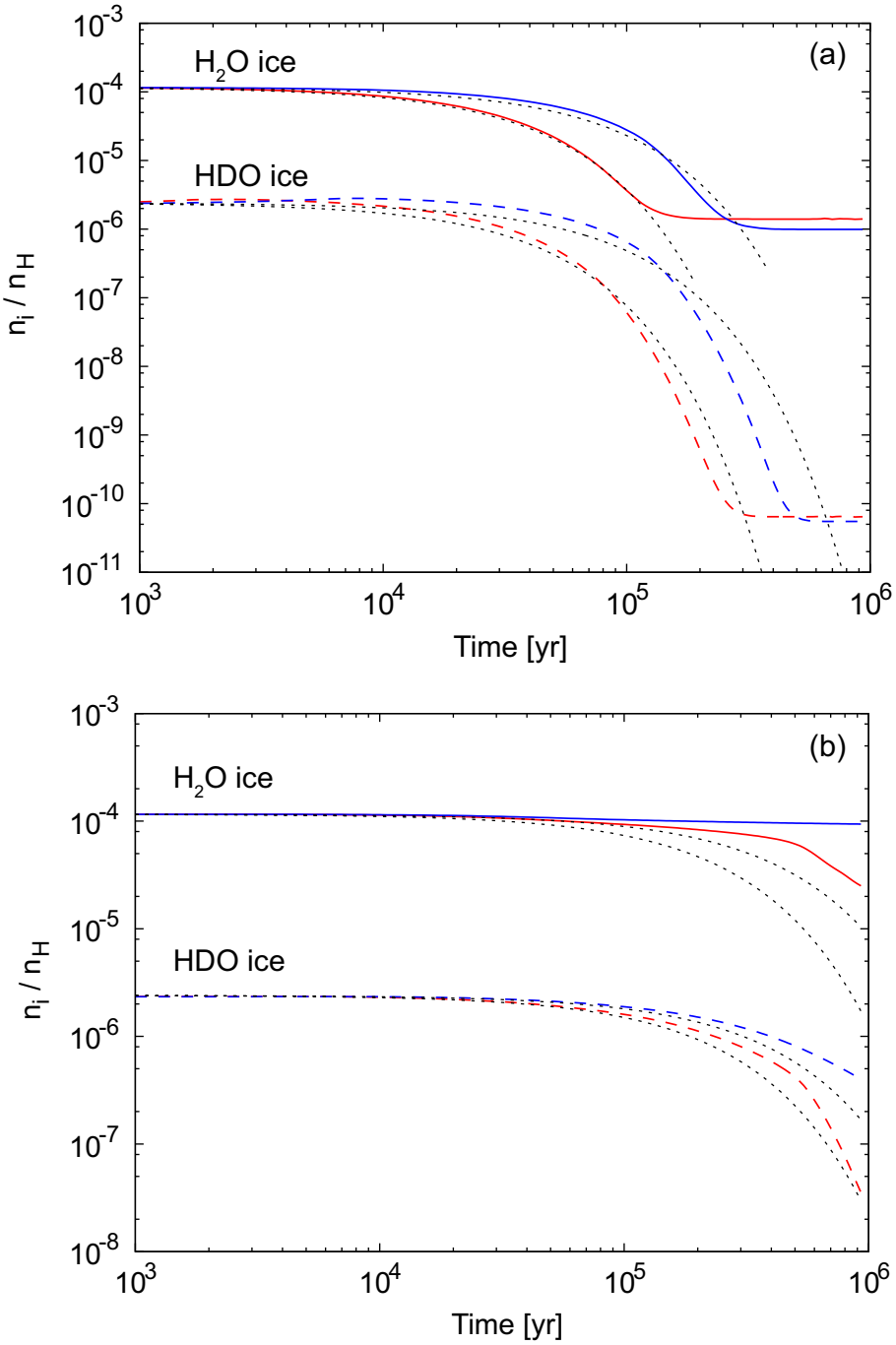

Figure 3.7: Temporal variations of abundances of H_2O ice (solid lines) and HDO ice (dashed lines) in the model with $\alpha_z = 10^{-2}$ at the midplane of (a) $r = 5$ AU (red) and 10 AU (blue), and (b) $r = 30$ AU (red) and 50 AU (blue). The dotted lines depict the temporal variation given by Equation (3.32).

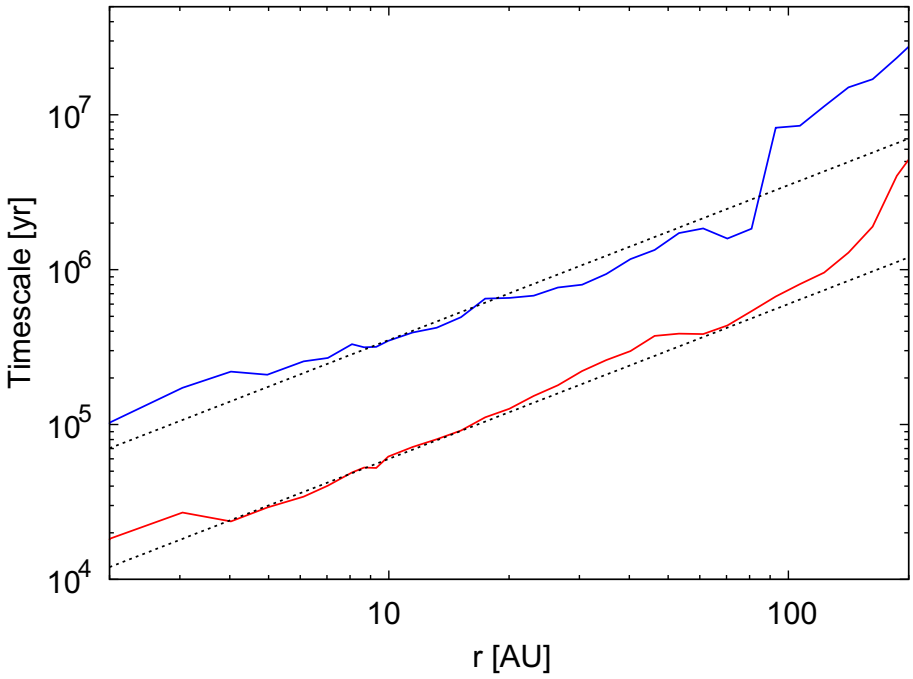

Figure 3.8: Radial variations of the destruction timescale of water ice, $\tau^{\rm mix}$, in the model with $\alpha_z = 10^{-3}$ (blue solid line) and 10^{-2} (red solid line). The dotted lines indicate Equation (3.33).

ratio is $\sim 2 \times 10^{-2}$. In the collapsing core, the species which are mostly formed in a cold era ($\sim$10 K), such as water, are enriched in deuterium through the isotope exchange reactions, such as, $H_3^+ + HD \rightleftharpoons H_2D^+ + H_2 + 230$ K. The backward reaction is endothermic, and is negligible compared to the forward reaction in the low gas temperature. Then, H_3^+ and several other species which are subject to the direct exchange reactions become enriched in deuterium. Chemical reaction network propagates the enrichment to other species, so that a significant amount of deuterium is delivered to the species other than HD and D_2 (e.g., Aikawa et al., 2012).

Figure 3.9 shows vertical profiles of a fraction of elemental deuterium in the form of HD and D_2 (i.e. $(x_{\rm HD} + 2x_{\rm D_2})/1.5 \times 10^{-5}$) in the disk models at $r = 30$ AU. The total fraction in other molecular form than HD and D_2, mainly ice, are also shown in Figure 3.9. At $N_{\rm H} \sim 10^{20}$ cm^{-2}, these fractions are small, since deuterium is mostly in atomic form. In the model without mixing, almost all deuterium is in HD (and D_2) at $N_{\rm H} = 10^{21}$–10^{22} cm^{-2}, since the other major deuterium reservoirs, such as HDO ice, are mostly destroyed by photoreactions. In the deeper regions, on the other hand, those reservoirs survive for 10^6 yr, since the timescales of photoreactions are longer than 10^6 yr there (see Figure 3.2). In the model with mixing, the deuterated ices are transported to the surface to be destroyed by photoreactions, while HD

is transported to the midplane. Note that the total elemental abundances in gas and dust, are not changed by the mixing, as long as dust grains are dynamically well-coupled to the gas. Because of the higher gas temperatures in the disk than that in the cold core, the endothermic exchange reactions, such as $H_2D^+ + H_2$, are not negligible. Therefore, reformation of deuterated ices is not efficient enough to compensate for the destruction. As a result, the HD abundance near the midplane increases with time, while the abundances of the other deuterium reservoirs decrease. For example, $\sim$20 % of deuterium is in the species other than HD at $t = 10^5$ yr in the midplane of $r = 30$ AU, while the fraction decreases to less than 1 % at $t = 10^6$ yr.

As shown in the bottom panel of Figure 3.7, the H_2O ice abundances are almost constant in the midplane at $r = 30$ AU and 50 AU, since reformation of H_2O ice (partly) compensates for the destruction. On the other hand, the HDO ice abundances decrease in a similar timescale to $\tau^{\rm mix}$. Then, the HDO_{ice}/H_2O_{ice} ratio decreases in a similar timescale to $\tau^{\rm mix}$ at these radii. In the inner radii, $r = 5$ AU and 10 AU, reformation of both ices is negligible, due to high dust temperatures. Since the destruction timescales of H_2O and HDO ices are similar, substantial changes of the HDO_{ice}/H_2O_{ice} ratio does not occur until their abundances decrease significantly and reach the steady state ($t >$ a few 10^5 yr; upper panel of Figure 3.7). Therefore, $\tau^{\rm mix}$ gives the approximate timescale of the decline of the HDO_{ice}/H_2O_{ice} ratio at $r \gtrsim 30$ AU in our models, while it gives the timescale of H_2O ice decrease at $r \lesssim 30$ AU.

Figure 3.10 shows radial variations of the HDO_{ice}/H_2O_{ice} column density ratio. While the D/H ratio retains its initial value ($\sim 2 \times 10^{-2}$) for 10^6 yr in the model without mixing, it decreases with time in the model with mixing. Since $\tau^{\rm mix}$ is smaller and the gas temperature is higher in inner radii, the resultant D/H ratio of water ice column density is roughly an increasing function of radius. In the model with $\alpha_z = 10^{-3}$, the HDO_{ice}/H_2O_{ice} ratio decreases by more than one order of magnitude at $r \lesssim 3$ AU within 10^6 yr. In the model with more efficient mixing, $\alpha_z = 10^{-2}$, such a significant decline of the HDO_{ice}/H_2O_{ice} ratio can be seen inside $r = 2$ AU and 30 AU, within 10^5 yr and 10^6 yr, respectively. It should be noted, however, that in these regions with the low HDO_{ice}/H_2O_{ice} ratio, water ice abundance and its column density are also lower than those in the model without mixing by about two orders of magnitude, and water ice is no longer the major oxygen reservoir.

In summary, at $r < 30$ AU, warm gas temperatures lead to low HDO_{ice}/H_2O_{ice} ratio, while warm dust temperatures hamper water ice reformation. At $r \gtrsim 30$ AU, the HDO_{ice}/H_2O_{ice} ratio decreases by up to one order of magnitude within 10^6 yr, without significant decrease of the water ice column density.

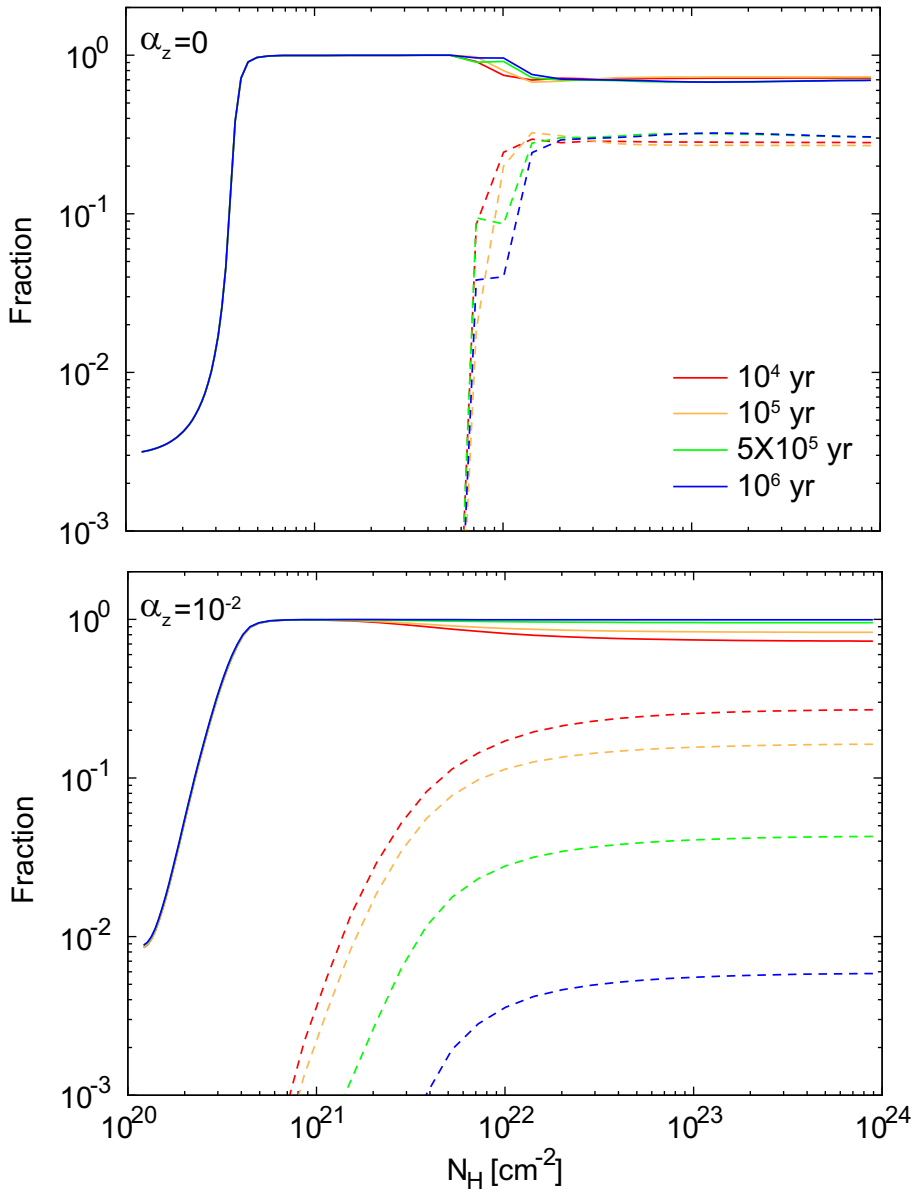

Figure 3.9: Temporal variations of the vertical profile of a fraction of elemental deuterium in the form of HD and D_2 (solid lines) and the total fraction in other molecular form than HD and D_2 (dashed lines) at $r = 30$ AU in the model with $\alpha_z = 0$ (upper panel) and $\alpha_z = 10^{-2}$ (lower panel).

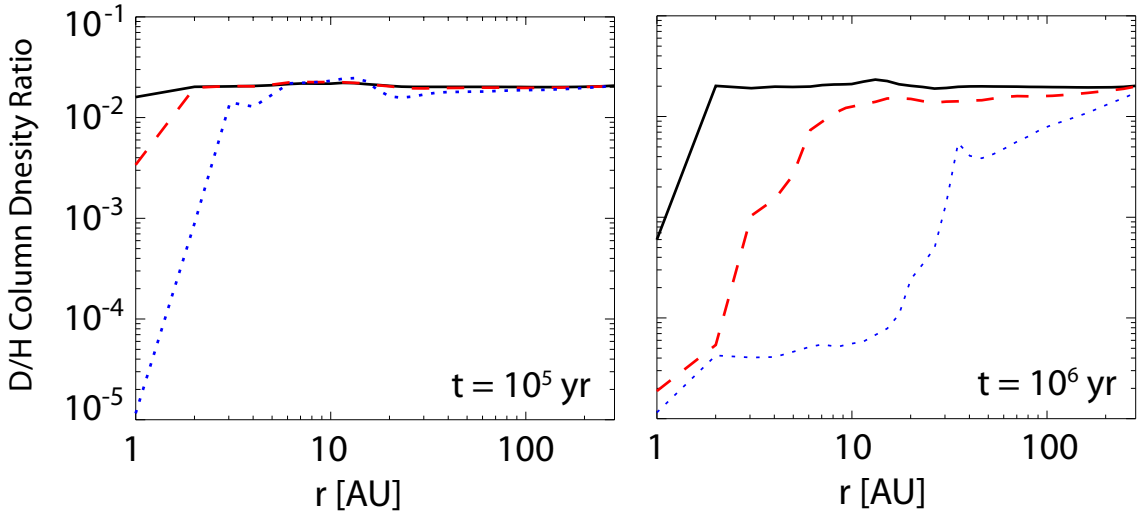

Figure 3.10: Radial distributions of HDO_{ice}/H_2O_{ice} column density ratio at 10^5 yr (left panel) and 10^6 yr (right panel) in the model with $\alpha_z = 0$ (solid lines), 10^{-3} (dashed lines), and 10^{-2} (dotted lines).

3.4.4 Deuteration of water vapor

Figure 3.11 shows spatial distributions of water vapor abundance and the gaseous HDO/H_2O ratio. In our model, water vapor is moderately abundant ($\gtrsim 10^{-8}$) in three regions: (i) the midplane inside the snowline, (ii) the disk surface at $r < 50$ AU, and (iii) the outer disk. They have been identified by previous disk chemical models without mixing (Woitke et al., 2009b; Meijerink et al., 2012). This structure is conserved in the model with vertical mixing. In this subsection, we discuss how the D/H ratio of water vapor is determined in these regions.

(i) The midplane inside the snowline ($T_g \sim T_d \sim 200$ K, $A_V > 10$, and $r \sim 1$ AU).

At $r \sim 1$ AU, the bulk of water exists in the gas phase near the midplane, since dust temperatures are higher than the sublimation temperature of water. Since FUV photons and X-rays are strongly attenuated, H_2O and HDO are mainly destroyed by reactions with ions and photons induced by cosmic-rays in a timescale of a few 10^5 yr. We note that cosmic-ray is also slightly attenuated; while the unattenuated cosmic ray ionization rate is 5×10^{-17} s^{-1}, the ionization rate is $\sim1\times10^{-17}$ s^{-1} in the midplane of $r = 1$ AU. H_2O and HDO reform via proton (deuteron) transfer (e.g., $H_3O^+ + NH_3$) and/or neutral-neutral reactions ($OH + H_2$ and $OD + H_2$; see Table 3.2). This cycle reduces the HDO/H_2O ratio, since the products of HDO destruction, such as H_2DO^+, are converted not only to HDO, but also to H_2O. The HDO/H_2O ratio decreases from the initial value in a similar timescale to the destruction timescale,

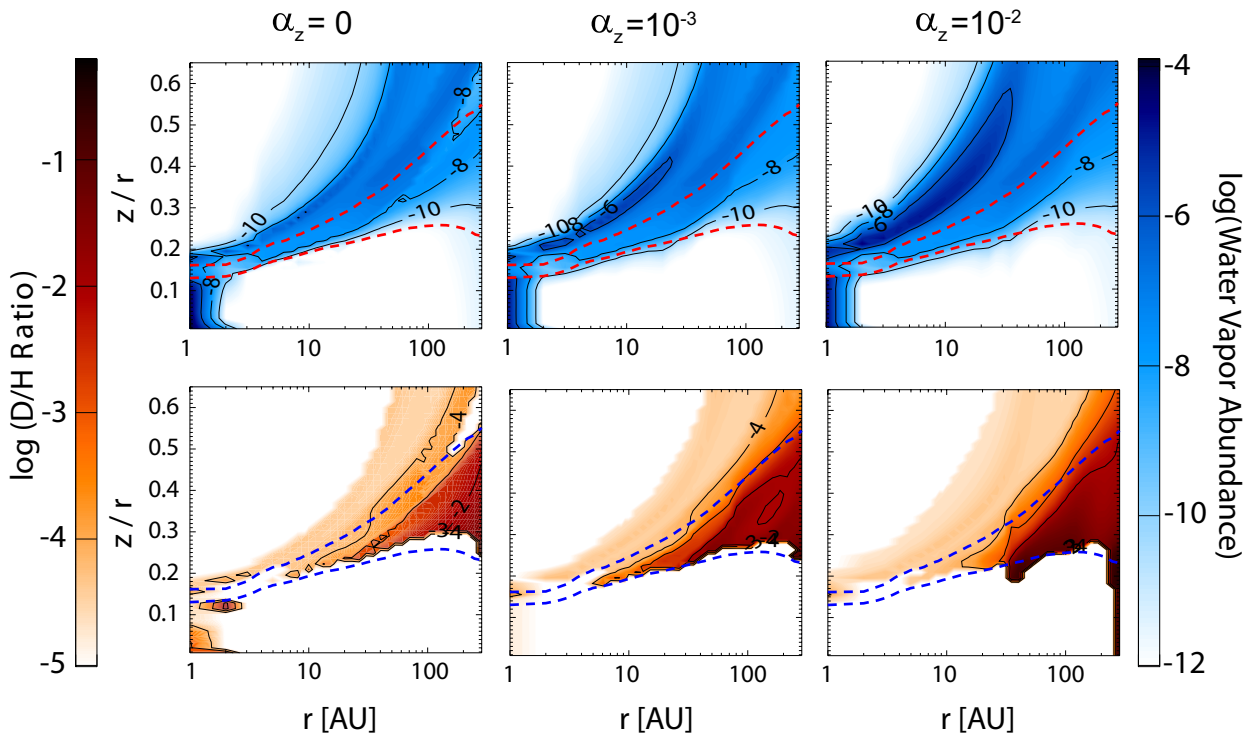

Figure 3.11: Spatial distributions of water vapor abundance (blue colors) and its D/H ratio (orange colors) in the model with $\alpha_z = 0$ (left panels), 10^{-3} (middle panels), and 10^{-2} (right panels) at 10^6 yr. The dashed lines indicate vertical visual extinction of unity and ten. The D/H ratios are only shown in regions where the water vapor abundance is higher than 10^{-12}.

and reaches $\sim 10^{-3}$ at 10^6 yr in the model without mixing. In the model with mixing, their destruction timescales are shortened by a combination of the upward transport and photoreactions at the disk surface. The HDO/H_2O ratio decreases in a timescale of 1×10^4 yr (7×10^4 yr) in the model with $\alpha_z = 10^{-2}$ (10^{-3}), and finally reaches $\sim 10^{-5}$.

(ii) The inner disk surface ($T_g \gtrsim$ 300 K, $A_V < 1$, and $r \lesssim$ 50 AU).

The HDO/H_2O ratio is as low as or less than 10^{-4} in this region, where dust and gas temperatures are decoupled. This result agrees with Willacy & Woods (2009). The HDO/H_2O ratio is similar to the OD/OH ratio, since H_2O and HDO is mainly formed via OH + H_2 and OD + H_2, respectively. While the exchange reaction of OH + D deuterates OH, the reverse reaction with the activation barrier of 810 K, OD + H, prevents the significant deuteration of OH (i.e. water) at $T_g \gtrsim 300$ K. Vertical mixing increases the abundance of water vapor in this region by enhancing the H_2 abundance (Section 3.4.1), while it does not strongly affect the HDO/H_2O ratio.

(iii) The outer disk ($T_g \lesssim$ 300 K, $A_V <$ a few, and $r \gtrsim$ 50 AU).

In the region with $T_g < 300$ K, H_2O and HDO mainly forms via a sequence of ion-neutral reactions, followed by the recombination of H_3O^+ and its isotopologues with an electron, while they are mainly destroyed via photodissociation and reactions with ions. It should be noted that the abundance of water in this region depends on the X-ray flux (Meijerink et al., 2012), and that photodesorption of water ice is important to keep a fraction of oxygen in the gas phase (e.g., Dominik et al., 2005). Vertical mixing increases both the abundances of OH and atomic deuterium by a factor of a few. The abundance of OD also increases, since it is mainly formed by the reaction of OH + D. Since H_2DO^+ is formed via a sequence of ion-neutral reactions, initiated by the reactions between OD and ions, the HDO/H_2O ratio in this region also increases in the model with mixing.

In Figure 3.12, we present radial variations of water vapor column density and its D/H ratio. At 3 AU $\lesssim r \lesssim$ 30 AU, the column densities of water vapor increase by up to one order of magnitude via vertical mixing compared to the model without mixing. This is due to the increased abundance of hot water ($T_g \gtrsim 300$ K). The column density at $\sim$1 AU decreases via vertical mixing by a factor of a few, since a fraction of oxygen transported from the surface is converted to O_2. At the inner disks (< 1 AU), where gas temperature near the midplane is higher than 300 K, reformation of water vapor via Reaction (3.30) would be faster than O_2 formation.

Vertical mixing also affects the HDO/H_2O column density ratio. One of the most important effects of the mixing is a substantial decrease of the ratio inside the snow line. Beyond the snow line, on the other hand, vertical mixing decreases or increases the column density ratio, depending on which dominates in the column density, hot water ($T_g \gtrsim 300$ K) or warm water ($T_g \lesssim 300$ K). The ratio at $r = 2$ AU is high

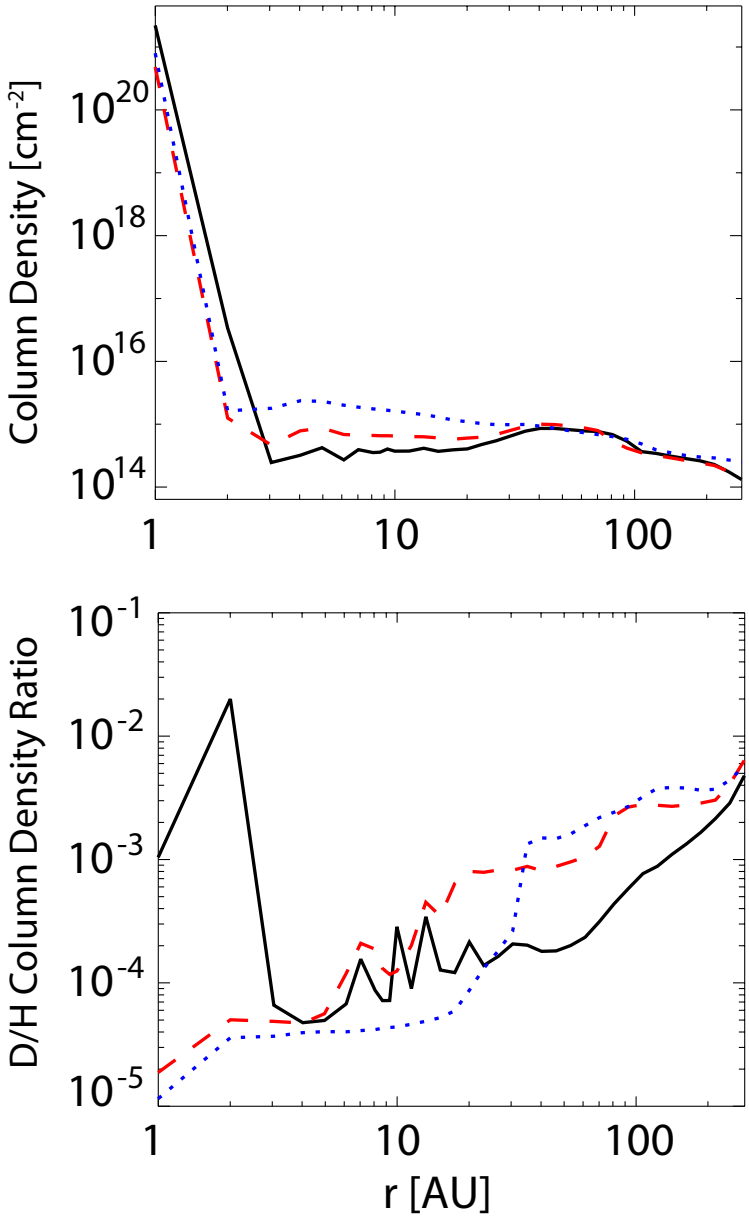

Figure 3.12: Radial variations of water vapor column density (top panel) and HDO/H_2O column density ratio (bottom panel) at 10^6 yr in the model with $\alpha_z = 0$ (solid lines), 10^{-3} (dashed lines), and 10^{-2} (dotted lines).

($\sim 10^{-2}$) in the model without mixing, since a fraction of water exists in the gas phase ($\sim 10^{-6}$) near the midplane via thermal desorption of ice.

Finally, we point out that the D/H ratios of water vapor and ice are different, especially in the inner regions ($r \lesssim 30$ AU), regardless of the strength of vertical mixing. This suggests that it is difficult to constrain the D/H ratios of water ice in the midplane of the inner disks from the observations of D/H ratios of water vapor in protoplanetary disks.

3.4.5 Comparisons to other works

The effect of mixing on water chemistry beyond the snow line ($r > 10$ AU) was studied by Semenov & Wiebe (2011), considering both radial and vertical mixing. Their chemical network is also based on Garrod & Herbst (2006). They found that water ice column densities in the model with and without mixing differ only by a factor of <2–5, which is consistent with our results at $r \gtrsim 30$ AU. However, in the inner disks, column densities of water ice decreases by more than one order of magnitude in our models. The difference seems to mainly come from the higher dust temperatures in our models compared to those in Semenov & Wiebe (2011). Radial mixing may also help maintain the high abundance of water ice.

While there are several studies focusing on deuterium fractionation in PPDs, none of them has considered mixing. Here, we briefly compare our model without mixing to those of Willacy & Woods (2009), which focused on the inner disks ($r \lesssim 30$ AU) considering the radial accretion. They found that both beyond and inside the snow line, the D/H ratio of water in the midplane retains its initial value ($\sim 10^{-2}$) for 10^6 yr. In our models without mixing, the D/H ratio of water ice in the midplane retains the initial value beyond the snow line, while the D/H ratio of water vapor decreases inside the snow line in a timescale of a few 10^5 yr. The different results inside the snow line seem to come from higher unattenuated cosmic-ray ionization rate in our models (5×10^{-17} s^{-1}), than that in Willacy & Woods (2009) (1.3×10^{-17} s^{-1}). The timescale of destruction and reformation of water vapor, and thus the timescale of decline of its D/H ratio is inversely proportional to the cosmic-ray ionization rate. If we adopt the unattenuated cosmic-ray ionization rate of 1.3×10^{-17} s^{-1}, the timescale becomes comparable to or longer than 10^6 yr. The combination of radial accretion and evaporation of water ice at the snow line may also help maintain the initial D/H ratio of water. Willacy & Woods (2009) also found that the HDO/H_2O ratio in the inner disk surface is as low as 10^{-4}, which is consistent with our model.

3.5 Discussion

3.5.1 Initial HDO/H_2O ratio

Some hot corino sources show the HDO/H_2O ratio as high as the initial value in our fiducial models ($\sim 10^{-2}$; Taquet et al., 2013a), while some sources show much lower value (10^{-4}–10^{-3}; Jørgensen & van Dishoeck, 2010; Persson et al., 2013). Here, we discuss the dependence of our results presented in Section 3.4 on the initial HDO/H_2O ratio.

In order to make the molecular composition with the low HDO/H_2O ratio, we artificially decrease the abundances of deuterated species except for HD by a factor of forty compared to the initial abundance used in our fiducial models. We reset the HD abundance so that the elemental deuterium abundance of 1.5×10^{-5} relative to hydrogen. For species without deuterium, we use the same abundances as those in our fiducial models. Then, the elemental abundances used here are slightly different from those in our fiducial models (at most ~ 4 %), except for deuterium. In this initial abundance, the HDO/H_2O ratio is $\sim 5 \times 10^{-4}$, which is similar to the cometary value ($\sim 6 \times 10^{-4}$), and ~ 99 % of deuterium is in HD.

In Figure 3.13, we show temporal variations of HDO_{ice}/H_2O_{ice} ratio in the mid-plane of $r = 50$ AU. The ratio increases with time from 5×10^{-4} to 2×10^{-3} in 10^6 yr in the model with $\alpha_z = 10^{-2}$, while the ratio is nearly constant in the model without mixing. Unlike the fiducial model, transport of deuterium via mixing is not important, since almost all deuterium is in HD from the beginning. Still, transport of oxygen affects water and deuterated water chemistry; atomic oxygen is transported from the surface to the deeper region, and (re)form H_2O and HDO ices. The HDO/H_2O ratio increases, since the D/H ratio of reformed water ice is larger than 5×10^{-4}. After a few 10^6 yr, the HDO_{ice}/H_2O_{ice} ratio reaches the steady-state value of 2×10^{-3}, which is independent of the initial ratio. The steady-state value should correspond to the D/H ratio of reformed water ice in the disk at a given radius (i.e. temperature).

Figure 3.14 shows radial distributions of HDO_{ice}/H_2O_{ice} column density ratio at $t = 10^6$ yr. In the inner region ($r \lesssim 40$ AU), where $\tau^{\rm mix}$ is much smaller than 10^6 yr, the HDO_{ice}/H_2O_{ice} ratio is independent of the initial ratio. In the outer region, on the other hand, the ratio depends on the initial ratio at least for 10^6 yr.

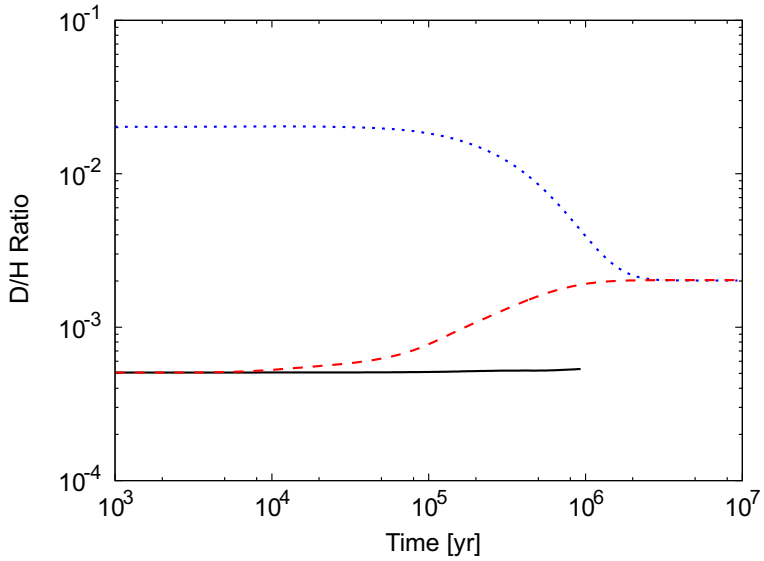

Figure 3.13: Temporal variations of HDO_{ice}/H_2O_{ice} ratio in the midplane of $r = 50$ AU in the model with $\alpha_z = 10^{-2}$ and the intial ratio of $\sim 2 \times 10^{-2}$ (dotted line) and $\sim 5 \times 10^{-4}$ (dashed line). The solid line indicates the HDO_{ice}/H_2O_{ice} ratio in the model without mixing and with the initial ratio of $\sim 5 \times 10^{-4}$.

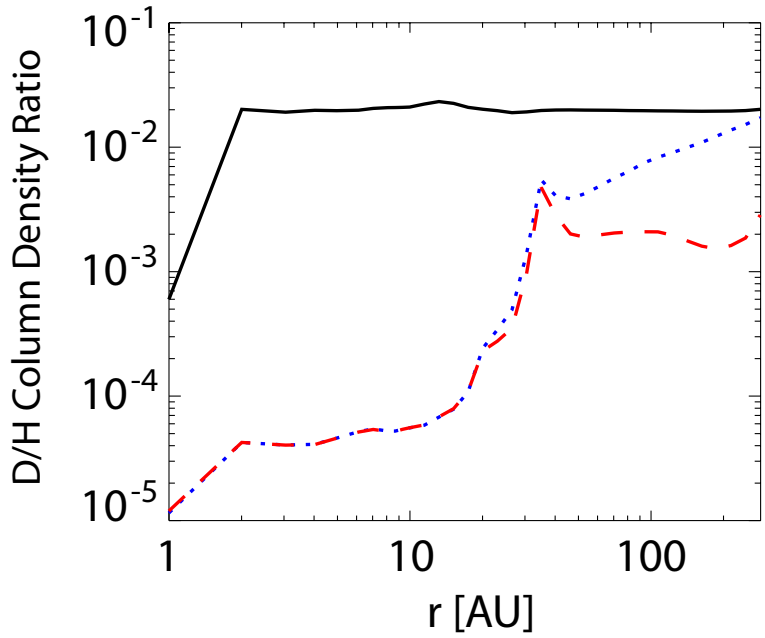

Figure 3.14: Radial distributions of HDO_{ice}/H_2O_{ice} column density ratio at $t = 10^6$ yr in the model with $\alpha_z = 10^{-2}$ and the initial ratio of $\sim 2 \times 10^{-2}$ (dotted line) and $\sim 5 \times 10^{-4}$ (dashed line). The parameter α_z is set to be 10^{-2} in both models. The solid line indicates the HDO_{ice}/H_2O_{ice} ratio in the model without mixing and with the initial ratio of $\sim 2 \times 10^{-2}$.

3.5.2 Uncertainties of chemistry on grain surfaces

Water formation

Recently, Meijerink et al. (2012) investigated water formation on carbonaceous grain surfaces, considering chemisorption of atomic hydrogen. They found that the reaction between physisorbed atomic oxygen and chemisorbed atomic hydrogen is very efficient at $T_{\rm d} < 40$ K, but the efficiency declines rapidly at higher temperatures. It also should be noted that chemisorption sites are unavailable on grain surfaces with ice-mantles (i.e. when $x_{\rm H_2O_{ice}} > N_{\rm site} x_{\rm d} \sim 10^{-6}$). Therefore, the inclusion of water ice formation on chemisorption sites would not significantly change our results.

In our fiducial models, the desorption energy of atomic hydrogen is fixed to be 450 K, following Garrod & Herbst (2006). Watanabe et al. (2010) and Hama et al. (2012) observed various kinds of potential sites (or site distributions) with different depths ($E_{\rm des}$) for atomic hydrogen on amorphous water ice in their experiments. According to molecular dynamics simulations, the site distribution peaks at $E_{\rm des} \sim 400$ K and ∼600 K for crystalline and amorphous water ices, respectively (Al-Halabi & van Dishoeck, 2007). Higher desorption energy of atomic hydrogen would lead to the longer residence time on grain surfaces, and thus a higher (re)formation rate of water ice. In order to check the dependence of $E_{\rm des}$ on our results, we reran our model from $r = 10$ AU to $r = 50$ AU with $E_{\rm des} = 600$ K for atomic hydrogen and deuterium. The resultant radial distribution of water ice column density and its D/H ratio are shown in Figure 3.15. In the model with $E_{\rm des} = 600$ K, the water ice reformation compensates the destruction at $r \gtrsim 20$ AU, while in our fiducial model ($E_{\rm des} = 450$ K), it compensates the destruction only at $r \gtrsim 40$ AU. In the inner region ($r \lesssim 20$ AU), the significant reduction of water ice column density occurs, even with $E_{\rm des} = 600$ K. The radial variations of the $\rm HDO_{ice}/H_2O_{ice}$ column density ratio does not strongly depends on $E_{\rm des}$. If the $E_{\rm des}$ is 600 K, the column density ratio of $\rm HDO_{ice}/H_2O_{ice}$ reaches the cometary value in 10^6 yr, while the $\rm H_2O$ ice abundance is kept high, in the comet forming regions ($r \sim 20$–30 AU)(see Section 3.5.5).

In order to efficiently (re)form water ice, OH should be formed on grain surfaces as discussed in Section 3.4.1. In our model, $\rm OH_{ice}$ is mainly formed via the reaction,

$$\rm O_{ice} + HNO_{ice} \rightarrow OH_{ice} + NO_{ice}. \tag{3.34}$$

The simplest reaction, $\rm O_{ice} + H_{ice}$, is less efficient, because of the lower desorption energy (or shorter residence time on grain surfaces) of atomic hydrogen than that of HNO (Table 3.3). The product $\rm NO_{ice}$ cycles back to $\rm HNO_{ice}$ via the reaction,

$$\rm NO_{ice} + H_{ice} \rightarrow HNO_{ice}, \tag{3.35}$$

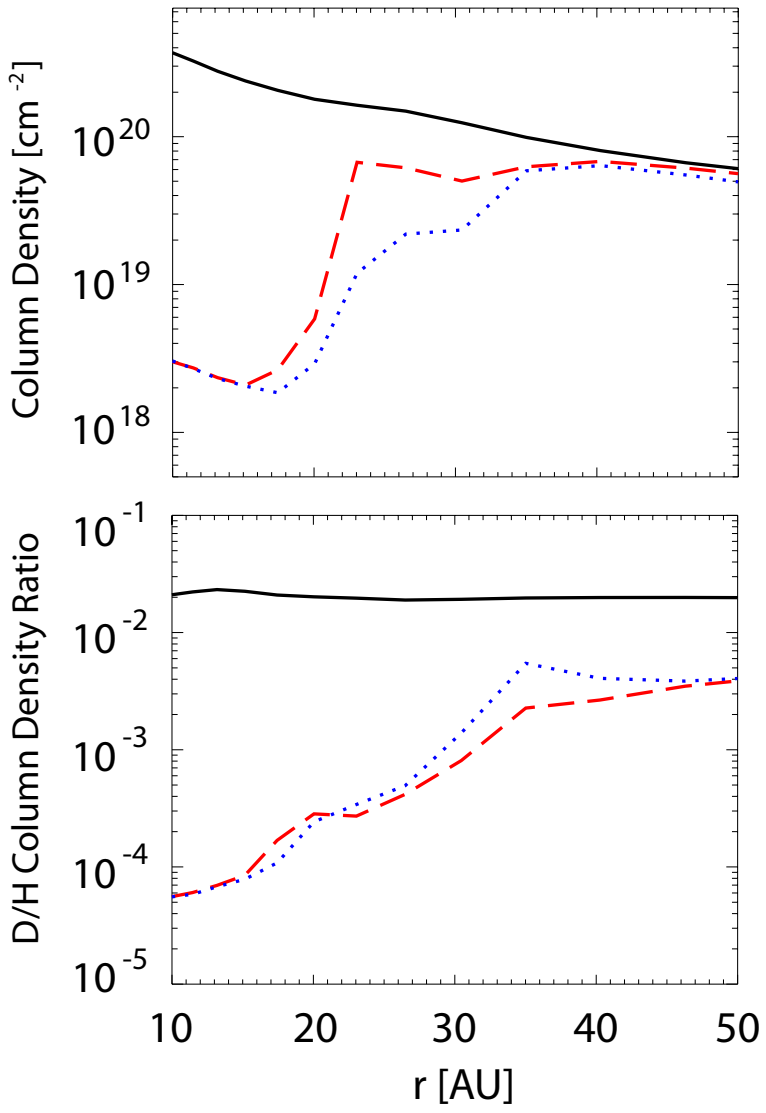

Figure 3.15: Radial distributions of water ice column density (upper panel) and HDO_{ice}/H_2O_{ice} column density ratio at $t = 10^6$ yr in the model with $\alpha_z = 10^{-2}$. The dashed lines indicate the model with $E_{des} = 600$ K for atomic hydrogen, while the dotted lines indicate the model with $E_{des} = 450$ K (our fiducial model). The parameter α_z is set to be 10^{-2} in both models. The solid lines indicate the values in the model without mixing.

which is faster than $O_{ice} + H_{ice}$, because of the longer residence time of NO than that of atomic oxygen. There is a caveat about this loop of NO_{ice}/HNO_{ice} interconversion as pointed out by Garrod et al. (2009). The grain-surface network of Garrod & Herbst (2006), which we employed, has only a limited number of reactions involving NO_{ice} and HNO_{ice}. While the network would be appropriate for cold environments (10 K), where atomic hydrogen is the dominant mobile reactant, NO_{ice} and HNO_{ice} could be subject to various other reactions in warmer environments, where species with heavy elements also become mobile. Garrod et al. (2009) mentioned that a more comprehensive reaction network that allowed NO_{ice} to react with, for example, atomic oxygen and nitrogen (which the current network does not) would make such loop inefficient. However, it is unclear whether the caveat applies to the disk chemistry with mixing. The physical condition of the disk, such as density, is significantly different from those of clouds/cores considered by Garrod et al. (2009). Mixing enhances the abundances of reactive species, such as atomic hydrogen and oxygen. Modeling of surface reaction on warm dust grains with a more comprehensive reaction network, which is currently unavailable, is desirable.

Photodissociation rates of ices

In our fiducial models, we calculate the photodissociation rates of ices (Equation 3.9), assuming that only the upper most one monolayer can be dissociated, while photoproducts immediately recombine in the deeper layers. We may underestimate the photodissociation rates of ices, if the probability of recombination of photofragments in the deeper layers, which would depend on ice temperatures (Öberg et al., 2009c), is much less than unity. To investigate the dependence of our results on the parameter $N_{\rm p}$, we rerun the calculation in which $N_{\rm p}$ is set to be equal to the number of monolayers ($N_{\rm layer}$).

The increased photodissociation rate of water ice enhances the conversion of water ice to CO_2 ice, since OH ice produced by water ice photodissociation are partly converted to CO_2 ice. Then, the region where CO_2 ice becomes the dominant oxygen reservoir is extended to $r \sim 50$ AU in the model with $\alpha_z = 10^{-2}$, while the boundary was $r \sim 40$ AU in the fiducial model. In our model, CO_2 ice is mainly formed by the reaction of $CO_{ice} + OH_{ice}$. The size of the CO_2 ice dominated region would also depend on the value of the activation energy barrier of this reaction. The barrier is assumed to be 80 K (Ruffle & Herbst, 2001) in our models, while Noble et al. (2011) concluded that the reaction is likely to have a higher barrier based on their experiments. If we adopt a higher value, the CO_2 ice dominated region should become smaller.

In our fiducial model with $N_{\rm p} = 2$, we artificially switch off the $D_{ice} + OH_{ice}$

branch of HDO ice photodissociation (see Section 3.3.2). When we assume $N_{\rm p} = N_{\rm layer}$, there is no reason to switch off the branch; here, we assume that the branches to produce OH ice and OD ice are equally weighted. We found that the $\rm HDO_{ice}/H_2O_{ice}$ ratios at $t = 10^6$ yr in the model with $\alpha_z = 10^{-2}$ are smaller than those in our fiducial model by up to a factor of five in the regions where water ice is the dominant oxygen reservoir ($r \gtrsim 50$ AU).

3.5.3 Effect of accretion and grain evolution

In the present study, we consider only vertical mixing as the mass transport in PPDs. However, radial mass transport (in the combination with the vertical mixing) could be also important for disk chemistry (e.g., Tscharnuter & Gail, 2007; Nomura et al., 2009; Heinzeller et al., 2011; Semenov & Wiebe, 2011). In Figure 3.16, we compare $\tau^{\rm mix}$ with the timescale of radial accretion in the model with $\alpha_z = 10^{-2}$. The accretion timescale is estimated by

$$\tau_{\rm acc} = r/v_{\rm acc}, \tag{3.36}$$

$$v_{\rm acc} = \dot{M}/2\pi r\Sigma, \tag{3.37}$$

where Σ is the surface density of gases. Note that when we determine the radial distribution of surface density in our disk models, we assume a viscous parameter of $\alpha = 10^{-2}$ as mentioned in Section 3.2. Figure 3.16 shows that the accretion timescale is comparable to $\tau^{\rm mix}$. The radial accretion would increase the water abundance and the $\rm HDO/H_2O$ ratio in our fiducial model with mixing at $r \lesssim 30$ AU, since they are higher at the outer radii.

We also neglect grain evolution in this work. In our chemical models, it is assumed that 0.1 μm dust grains are uniformly distributed in the disk with the dust-to-gas mass ratio of 10^{-2}. In reality, PPDs contain grains as large as 1 mm, and a fraction of them would be settled to the midplane (e.g., Przygodda et al., 2003; Furlan et al., 2006, 2011). While the 0.1 μm grains are well-coupled to the gas, the coupling is less efficient for larger grains. If large grains with ice mantles settle the midplane, but small grains remain in the disk surface to shield UV radiation, destruction of water ice via the combination of vertical mixing and photoreactions would become less efficient, although water vapor is subject to the destruction as long as turbulence exists. A similar situation is considered to account for the weak emission line of water vapor detected towards TW Hya (Hartogh et al., 2011).

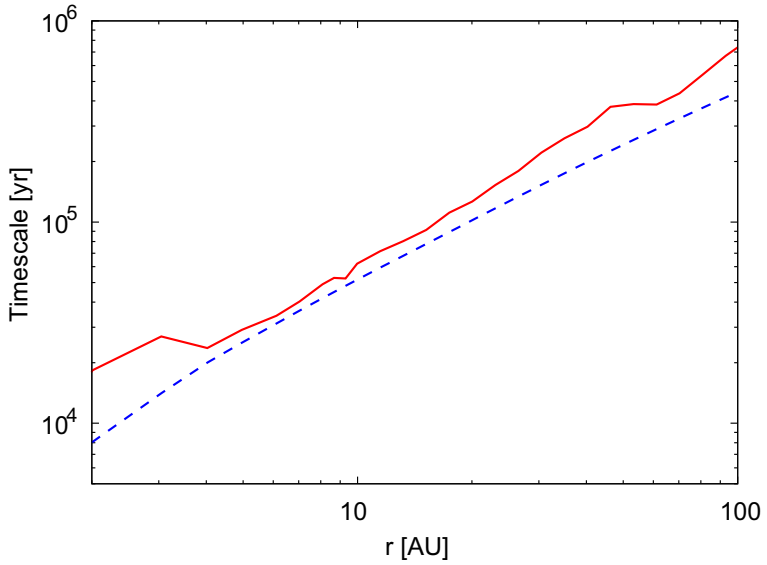

Figure 3.16: Comparisons of mixing timescale ($\tau^{\rm mix}$; solid line) and radial accretion timescale of gas (dashed line).

3.5.4 Effect of dead zone

In our fiducial models, we assume that α_z is constant in space. According to MHD simulations, however, velocity dispersion in a dead zone is smaller than that in a MRI active region by more than one order of magnitude, depending on the strength of the magnetic field (Okuzumi & Hirose, 2011; Gressel et al., 2012). In this subsection, we consider the models, in which α_z is dropped by one order of magnitude in a dead zone. We define a dead zone as the regions with the magnetic Reynolds number, $R_{\rm M}$, is less than 100 (e.g., Fleming et al., 2000). Following Perez-Becker & Chiang (2011), the magnetic Reynolds number is evaluated by

$$R_{\rm M} = c_s h/\eta, \tag{3.38}$$

$$\eta = 234\sqrt{T_{\rm g}}/x'_e, \tag{3.39}$$

where h, η, and $x'_{\rm e}$ are the pressure scale height, electrical resistivity of the gas, and the electron abundance with respect to neutrals, respectively. For example, the threshold values of $x'_{\rm e}$ for the dead zone in our disk model are 9×10^{-13} and 4×10^{-13} at $r = 5$ AU and 10 AU, respectively.

In Figure 3.17, we show a dead zone boundary (solid line), plotted over the distribution of water ice abundance in the model with $\alpha_z = 10^{-2}$ at $t = 10^4$ yr. The dead zone exists near the midplane ($z/r \lesssim 0.1$) at $r \lesssim 10$ AU. The dashed line in Figure 3.17 indicates the height z^*, at which the effective flux of water ice to the

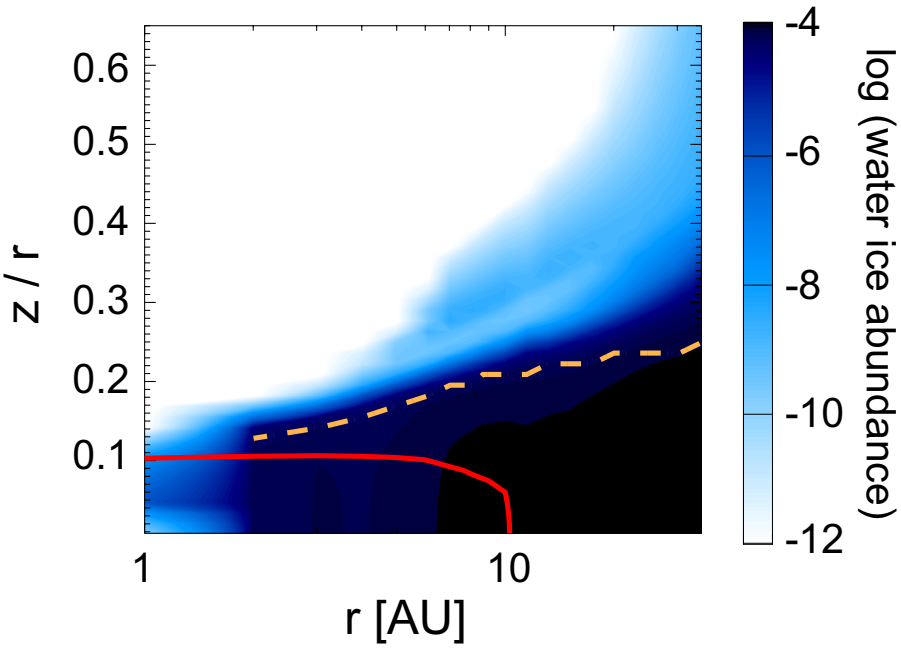

Figure 3.17: The dead zone boundary (solid line) plotted over the distribution of water ice abundance in the model with $\alpha_z = 10^{-2}$ at $t = 10^4$ yr. The dashed line indicates the height z^*.

disk surface is determined (Section 3.4.2). The height z^* is located above the dead zone boundary. In other words, the water ice layer is thicker than the dead zone, and the net upward transport of water ice takes place in the MRI active region in our models. We performed a calculation considering the dead zone, and confirmed that the existence of the dead zone does not significantly change our results on both water ice and vapor.

3.5.5 Cometary water

Comets observed today are believed to be supplied from two distinct reservoirs, the Oort cloud and the Kuiper belt. Until recently, it was widely accepted that the Oort cloud comets (OCCs) formed in and was scattered outward from the giant planet forming region ($r \sim$ 5–30 AU), while Jupiter-family comets (JFCs) formed in the Kuiper belt region ($r \gtrsim 30$ AU) (Brownlee, 2003). However, recent dynamical models of solar system evolution suggest more complicated scenarios; substantial migration of the giant planets occurred and it led to large scale mixing of distributions of planetesimals (Gomes et al., 2005; Walsh et al., 2011). If this is the case, OCCs and JFCs would share their origins at least in part.

So far, the HDO/H_2O abundance ratio has been measured in seven OCCs (e.g.,

Bockelée-Morvan et al., 2012) and two JFCs (Hartogh et al., 2011; Lis et al., 2013). These observations indicate that

1. the HDO/H_2O ratio of cometary water is the order of 10^{-4},
2. the HDO/H_2O ratio observed in the JFCs ($(3–<4) \times 10^{-4}$) is smaller than the average value observed in the OCCs ($\sim 6 \times 10^{-4}$).

In our fiducial models with $\alpha_z = 0$ and 10^{-3}, in which the initial HDO/H_2O ratio is $\sim 2 \times 10^{-2}$, the model D/H ratios in water ice remain much higher than the cometary value even at $t = 10^6$ yr. In the model with $\alpha_z = 10^{-2}$ and $E_{\rm des} = 600$ K for atomic hydrogen, water ice is abundant ($\sim 10^{-4}$) and its D/H ratio is comparable to the cometary value at $r \sim 20$–30 AU as shown in Figure 3.15. Such region with abundant water ice and the preferable D/H ratio can extend to inner radius, if the reformation of water ice is more efficient than that in our models. Then, our model suggests the possibility that the D/H ratio of cometary water could be established (i.e. cometary water could be formed) in the solar nebula, even if the D/H ratio of water ice formed in the parent molecular cloud/core was very high ($\sim 10^{-2}$) as observed in NGC 1333-IRAS2A and NGC 1333-IRAS4A (Taquet et al., 2013a). NGC 1333-IRAS4A and IRAS 16293-2422, on the other hand, show similar HDO/H_2O ratio to that of cometary water (Jørgensen & van Dishoeck, 2010; Persson et al., 2013). Hence, it is not clear at this moment whether cometary water originates in the parent molecular cloud or the solar nebula. Our model predicts that if the HDO/H_2O ratio is significantly changed in the disk, D/H ratios of other ices, such as CH_3OH, in comets would also be different from those in the molecular cloud/core.

Variation of HDO/H_2O ratio is another interesting issue. If cometary water originates in molecular clouds, their HDO/H_2O ratio could be more uniform. Our model predicts that the HDO/H_2O ratio increases with radius in the region where the model HDO/H_2O ratio is comparable to the cometary value. This contradicts with the classical dynamical model in which the OCCs originated in the inner region than the JFCs, and may support the recent dynamical model with migration of giant planets. It should be noted, however, that the radial gradient of HDO/H_2O ratio could be reversed, if grain settling proceeds faster in inner radii. In addition, the radial distribution of the HDO/H_2O ratio can also be affected by the radial transport of low D/H water near the central star, which is not yet considered in our model (Yang et al., 2013). Further studies are needed to constrain the formation regions of JHCs and OCCs from their HDO/H_2O ratios.

3.6 Conclusion

We have investigated water and deuterated water chemistry in protoplanetary disks irradiated by UV and X-ray from a central T Tauri star. We have solved chemical rate equations with the diffusion term, mimicking the turbulent mixing in the vertical direction. Oxygen is mainly in atomic form in the disk atmosphere, while it is in water near the midplane. When turbulence exists, water near the midplane is transported to the disk surface and destroyed by photoreactions, while atomic oxygen is transported to the midplane and reforms water and/or other molecules. We found that this cycle significantly affects water and deuterated water chemistry. Our conclusions are as follows.

1. Beyond the snow line, the cycle decreases the column densities of water ice by more than one order of magnitude within 10^6 yr in the inner disk ($r \lesssim 30$ AU), where dust temperatures are too high to form OH radical on grain surfaces. Once OH radical is formed in the gas phase, it is converted to O_2 via the reaction of OH + O before it is adsorbed onto dust grains to form water ice, because of the high abundance of atomic oxygen near the O/H_2O_{ice} transition. The outer edge of such regions moves to $r = 20$ AU, if the desorption energy of atomic hydrogen is as high as 600 K. Our model indicates that water ice could be deficient even outside the sublimation radius.

2. At $r \gtrsim 30$ AU, the cycle decreases the D/H ratios in water ice from $\sim 2 \times 10^{-2}$, which set by the collapsing core model, to 10^{-3}–10^{-2} within 10^6 yr, without significant decrease of the column densities. The resultant ratio depends on the strength of mixing and the radial distance from the central star. If $E_{\rm des}$ is 600 K for atomic hydrogen, the D/H ratio of water ice decreases to 10^{-4}–10^{-3} at $r \sim 20$–30 AU without significantly decreasing the water ice column density. Our model suggests that the D/H ratio of cometary water could be established (i.e. cometary water could be formed) in the solar nebula, even if the D/H ratio of water ice formed in the parent molecular cloud/core was very high ($\sim 10^{-2}$) as observed in some hot corinos.

3. We confirmed that water vapor has moderately high abundance ($\gtrsim 10^{-8}$) in the three regions: (i) the midplane inside the snowline, (ii) the inner disk surface, and (iii) the outer disk as shown in previous works. We found that this structure conserves in the model with vertical mixing. Inside the snow line, the D/H ratios in water vapor become as low as 10^{-5} in the model with mixing.

4. The D/H ratios of water vapor and ice are different, especially in the inner regions ($r \lesssim 30$ AU), regardless of the strength of vertical mixing. It suggests that it is difficult to constrain the D/H ratios of water ice in the inner regions from the observations of D/H ratios of water vapor toward protoplanetary disks.

Chapter 4

Reprocessing of ices in turbulent protoplanetary disks: carbon and nitrogen chemistry

Abstract

We study the influence of the turbulent transport on ice chemistry in a protoplanetary disk, focusing on carbon and nitrogen bearing molecules. Chemical rate equations are solved with the diffusion term, mimicking the turbulent mixing in the vertical direction. Turbulence can bring ice-coated dust grains from the disk midplane to the warm irradiated surface, and the ice mantles are reprocessed by photoreactions and surface reactions. We show that the upward transport of ices decreases the abundance of saturated molecules, such as methanol and ammonia, at $r \lesssim 30$ AU, because higher dust temperature prohibits their reformation via hydrogenation on grain surfaces, while water ice abundance decreases only at $r \lesssim 20$ AU. We also show the effect of turbulent mixing on the synthesis of complex organic molecules are twofold: (1) transport of ices from the disk midplane to the surface and (2) transport of atomic hydrogen from the surface to the midplane. The former enhances the formation of complex molecules in the disk surface, while the latter enhances the hydrogenation of radicals, and thus suppresses the formation of complex molecules in the midplane. As a result, complex organic molecules are mainly formed in the disk surface when mixing is strong. We discuss the implication of our model results to the origin of cometary molecules. Our model with mixing reproduce the ring-like distribution of gaseous H_2CO, which was recently suggested via radio observations. We also evaluate the timescale for CO to be converted to carbon chains, and thus depleted from the gas phase.

4.1 Background

One of the most intriguing questions in the studies of astrochemistry is whether and how much of the pristine materials in the solar nebula were inherited from interstellar matter (ISM) (see e.g., recent review by Caselli & Ceccarelli, 2012). Comets are thought to be the most pristine objects of the cold ice-bearing regions in the solar nebula (e.g., Brownlee, 2003). When a comet approaches the sun, sublimation of volatile species produces the envelope around the cometary nuclei, which is called coma. Many molecules have been detected in cometary coma, and their abundances with respect to water have been derived (Mumma & Charnley, 2011, and reference therein). All molecules detected in comets have been also detected in prestellar or protostellar cores. This similarity suggests that cometary molecules could originate from the core phase. Öberg et al. (2011) pointed out, however, that cometary abundances of CO, CH_4, and CH_3OH are lower than the median abundances of the ices in low-mass protostellar envelopes, obtained from the *Spitzer* c2d Legacy ice survey. Ootsubo et al. (2012) conducted a spectroscopic survey of cometary molecules using AKARI, and found that CO_2 is depleted in comets, as well. In addition to carbon bearing molecules, NH_3 is also depleted in comets compared to the low-mass protostellar ices (e.g., Öberg et al., 2011; Kawakita & Mumma, 2011; Biver et al., 2012). Recent chemical-dynamical model suggests that the majority of water is delivered from cores to disks as ice (Visser et al., 2011). If this was the case in the solar nebula, CH_3OH and NH_3 would also be delivered to the disk as ice, since CH_3OH and NH_3 are co-desorbed with water as shown by temperature programmed desorption (TPD) experiments (Collings et al., 2004). Then their depletions in comets may imply that some reprocessing of ices occurred in the solar nebula, although it is unclear whether the observed median composition well represents the ice composition in the protosolar envelope.

In this chapter, we investigate the effect of turbulent mixing in the vertical direction on ice chemistry in Class II protoplanetary disks. Most previous disk chemical models have not considered the turbulent mixing. As shown in Chapter 3 (Furuya et al., 2013), combination of upward transport and photochemistry of ices leads to destruction and reformation of ices. This strongly contrasts with disk models without turbulence, where most of the ices survive for $>10^6$ yr, because they are mainly exist in the midplane, shielded from stellar UV and X-ray. In Chapter 3, we focused on water ice and the HDO/H_2O ratio. Here we focus on other simple species, such as NH_3 and CH_3OH.

In addition to simple molecules, we also investigate synthesis of complex organic molecules, such as $HCOOCH_3$, in turbulent disks. One possible formation pathway of complex molecules is the grain surface reaction between heavy radicals formed

via ultraviolet photolysis of simpler molecules (e.g., Herbst & van Dishoeck, 2009, and reference therein). Although formation of complex molecules in the gas phase has been also proposed (e.g., Charnley et al., 1992), recent experiments suggest that some key gas-phase reactions are less efficient than previously thought (Geppert et al., 2006). For grain-surface formation, there are (at least) two important factors: UV photons to form radicals and warm dust temperature (e.g., Öberg et al., 2009c). In the cold temperature ($\sim$10 K), hydrogenation of atoms and molecules is the most efficient surface reaction. When dust temperature is warm ($\gtrsim$30 K), surface chemistry involving heavy radicals becomes important, as they can be mobile on grain surfaces, while hydrogen atoms tend to evaporate rather than react (Garrod & Herbst, 2006; Garrod et al., 2008).

Very recently, Walsh et al. (2014) studied spatial distributions of complex molecules in a disk without turbulent mixing. Their model reasonably reproduces the observed abundance of the complex molecules in comets. Recent theoretical studies suggested that turbulent mixing could increase the formation efficiency of complex organic molecules (Semenov & Wiebe, 2011; Ciesla & Sandford, 2012). Ciesla & Sandford (2012) traced trajectories of dust grains in a turbulent disk, and showed that dust grains move throughout the disk, experiencing irradiation and warming. They found that incident photon number on grain surfaces is sufficient to produce significant amount of complex organic molecules, if they assume the production efficiency of complex molecules per incident photon obtained from laboratory experiments. It is thus important as a next step to calculate rate equations to evaluate the formation of complex organic molecules in the turbulent disk. To the best of our knowledge, Semenov & Wiebe (2011, hereafter SW11) is the only work which investigated chemistry of complex organic molecules in turbulent disks by solving chemical rate equations, so far. SW11 found that complex molecules, HCOOH ice and CH_3CHO ice, are much more abundant in the model with mixing than those in the model without mixing.

This chapter is organized as follows. In Section 4.2, we briefly describe physics and chemistry in our numerical model. In Section 4.3, we present our results, while in Section 4.4, we discuss the implication of our model results on the compositions of comets. We compare our results with SW11, and also discuss the uncertainties of ice photolysis. We summarize our conclusions in Section 4.5.

4.2 Physical and chemical modeling

The physical and chemical models used in this work are almost the same as those in Chapter 3. One dimensional reaction-diffusion equations (Xie et al., 1995; Willacy

et al., 2006) are solved in a disk physical model of Nomura et al. (2007):

$$\frac{\partial n_i}{\partial t} + \frac{\partial \phi_i}{\partial z} = P_i - L_i, \tag{4.1}$$

$$\phi_i = -n_{\rm H} D_z \frac{\partial}{\partial z}\left(\frac{n_i}{n_{\rm H}}\right), \tag{4.2}$$

where n_i, P_i, and L_i represent the number density, production rate, and the loss rate, respectively, of species i. The second term in the left-hand side of Equation (4.1) mimics turbulent mixing in the vertical direction, and D_z is a diffusion coefficient. Equation (4.1) is integrated for 10^6 yr using implicit finite differencing on a linear grid consisting of vertical 60 points at a specific radius. In the rest of this section, we briefly outline our physical and chemical models.

4.2.1 Disk structure

We adopt a disk model of Nomura et al. (2007); it is a steady, axisymmetric Keplerian disk surrounding a typical T Tauri star with the mass $M_* = 0.5\ M_\odot$, radius $R_* = 2\ R_\odot$, and effective temperature $T_* = 4000$ K. The stellar UV and X-ray luminosities are set to be 10^{31} erg s^{-1} and 10^{30} erg s^{-1}, respectively, based on the spectrum observed towards TW Hya (e.g., Herczeg et al., 2002; Kastner et al., 2002). The dust-to-gas mass ratio is set to be 0.01 with the dust size distribution model adequate for dense clouds (Weingartner & Draine, 2001). The gas temperature, dust temperature and density distributions of the disk are calculated self-consistently, considering various heating and cooling mechanisms (see Nomura & Millar, 2005; Nomura et al., 2007, for details). The disk structure adopted in this chapter is shown in Figure 4.1 for convenience.

We assume that the origin of the disk turbulence is the magnetorotational instability (Balbus & Hawley, 1991). The vertical diffusion coefficient is assumed to be

$$D_z = \alpha_z c_s^2 / \Omega, \tag{4.3}$$

where Ω and c_s are the Keplerian orbital frequency and local sound speed, respectively (Fromang & Papaloizou, 2006; Okuzumi & Hirose, 2011). We can safely use the same D_z for gaseous and ice mantle species, since dust radius is assumed to be 0.1 μm in our chemical model and the ratio of gas to dust diffusivity of such a small grain is nearly unity. We assume that the alpha parameter, α_z, is constant for simplicity, and run three models with $\alpha_z = 0$, 10^{-3}, and 10^{-2}.

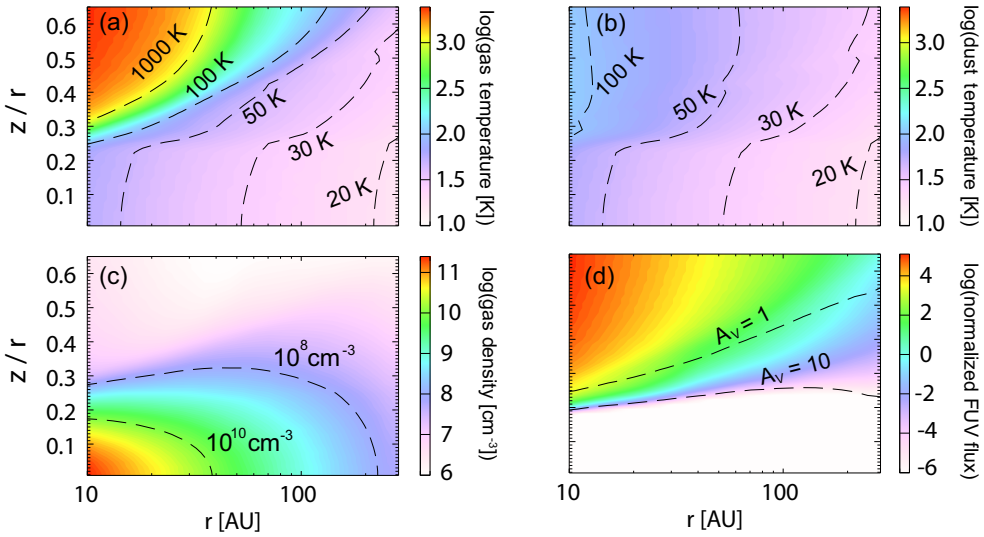

Figure 4.1: Spatial distributions of the gas temperature (a), dust temperature (b), number density of gases (c), and wavelength-integrated FUV flux normalized by Draine field (1.6×10^{-3} erg cm^{-2} s^{-1}; Draine, 1978, (d)). In panel (d), the dashed lines indicate the height at which the vertical visual extinction of interstellar radiation field reaches unity and ten. The vertical axes represent height normalized by the radius.

4.2.2 Chemical model

To compute disk chemistry, a two-phase model, which consists of gas-phase and grain-surface species, is adopted (Hasegawa et al., 1992). Our chemical reaction network is based on Garrod & Herbst (2006), and modified to be applicable to disk chemistry. The species with chlorine and phosphorus, molecules with more than four carbon atoms, and their relevant reactions are excluded from the network to reduce the computational time. As chemical processes, we take into account the gas phase reactions, interaction between gas and grains, and grain surface reactions. Since the detailed explanation of our chemical model can be found Chapter 3, here we only describe updates of our chemical reaction network, photochemistry of ices, and the initial abundance of the disk.

The chemical reaction network and adopted parameters are the same as in a fiducial model of Chapter 3, except for the following three updates. Firstly, desorption energy of atomic hydrogen is set to be 600 K instead of 450 K; the former is adequate for amorphous water ice, while the latter is adequate for crystalline water ice (Al-Halabi & van Dishoeck, 2007). Secondly, the activation energy barrier of CO + OH reaction on grain surfaces are set to be 176 K (Cuppen et al., 2009) instead of 80 K (Ruffle & Herbst, 2001). The value of this barrier is currently controversial;

Noble et al. (2011) concluded that it is ∼400 K from their laboratory experiment, while Oba et al. (2010) concluded that the reaction proceeds with little or no barrier. In this work, we adopt the barrier of the same reaction (CO + OH) in the gas phase. Thirdly, photodissociation branching ratios of methanol ice are updated following the experimental work of Öberg et al. (2009c). CH_3OH is a parent molecule of more complex species, and the photodissociation branching ratio is an important parameter for the formation efficiency of complex organic molecules (Laas et al., 2011). Öberg et al. (2009c) estimated CH_3OH photodissociation branching ratio (CH_2OH+H):(CH_3O+H):(CH_3+OH) of 5:1:<1, based on their experiments. Since we do not discriminate between isomers, CH_2OH and CH_3O, in our network, the branching ratio (CH_3O+H):(CH_3+OH) is set to be 9:1.

UV irradiation experiments have shown that ice molecules can be photodissociated and photodesorbed (e.g., Gerakines et al., 1996; Westley et al., 1995). Photodissociation of ice molecules produces radicals, while photodesorption can keep a fraction of molecules in the gas phase even at low dust temperatures. The photodissociation rates (cm^{-3} s^{-1}) of ice species are calculated as follows:

$$R_{\mathrm{phs},i} = \pi a^2 n_{\mathrm{d}} \int 4\pi J(\lambda)[1 - \exp(-\tau_i(\lambda))]d\lambda, \tag{4.4}$$

$$\tau_i(\lambda) = \frac{N_{\mathrm{p}} \sigma_i(\lambda) n_i}{\sigma_{\mathrm{site}} n_{\mathrm{ice}}}, \tag{4.5}$$

$$N_{\mathrm{p}} = \min(N_{\mathrm{layer}}, 2), \tag{4.6}$$

where a, n_{d}, n_{ice}, σ_{site}, and N_{layer} are the grain radius, the number density of the grain, the total number density of ice mantle species per unit volume of gases, the site area, and the number of monolayer of ice mantles ($n_{\mathrm{ice}}/n_{\mathrm{d}}N_{\mathrm{site}}$, with the number of adsorption sites on a grain $N_{\mathrm{site}} \sim 10^6$), respectively. While τ_i represents the optical depth of ice mantle species i, the term $(1 - \exp(-\tau_i))$ represents the fraction of photon absorbed by species i in the ice. $J(\lambda)$ is the mean intensity of the radiation field measured in units of photons cm^{-2} s^{-1} $Å^{-1}$ str^{-1} at the wavelength of λ. We consider stellar, interstellar, and X-ray-induced and cosmic-ray-induced UV radiation. The cross sections, $\sigma_i(\lambda)$, for water and CO_2 ices are taken from Mason et al. (2006). For the other species, we use the same cross section used for corresponding gaseous species, because data are not available in the literature. Following Chapter 3, we assume that the uppermost monolayers can be dissociated as the outcome of photoabsorption, and that the photoproducts immediately recombine in the deeper layers; the number of active layer for photodissociation, N_{p}, is restricted to less than two for all species, considering surface roughness. We discuss the effect of these assumptions on our results in Section 4.4.3. Equations (4.4–4.6) are essentially the

Table 4.1: Initial Abundances of Assorted Species With Respect To Hydrogen Nuclei for the Disk Chemistry.

Species	Abundance[1]	Species	Abundance
H_2O	1.2(-4)	CO	3.6(-5)
CO_2	3.5(-6)	CH_4	1.5(-5)
H_2CO	1.2(-5)	CH_3OH	6.5(-6)
$HCOOCH_3$	2.4(-9)	CH_3OCH_3	6.4(-11)
N_2	4.5(-6)	NH_3	1.4(-5)

same as Equations (3.9–3.11) when τ_i is much less than unity. This is the case for all species in our fiducial models, since $(\sigma_i/\sigma_{\rm site})$ and/or $(n_i/n_{\rm ice})$ are much less than unity.

The photodesorption rates are calculated as (e.g., Visser et al., 2011)

$$R_{{\rm pd},i}(r,z) = \pi a^2 n_{\rm d} \theta_i F_{\rm FUV}(r,z) Y_i, \tag{4.7}$$

$$\theta_i = \frac{n_i}{\max(n_{\rm ice}, n_{\rm d} N_{\rm site})}, \tag{4.8}$$

where $F_{\rm FUV}$ are the FUV photon number flux integrated in the range of 912–2000 Å. We use photodesorption yields per incident FUV photon, Y_i, derived from experimental work for H_2O, CO_2, CO, O_2, and N_2 ices (Öberg et al., 2009a,b; Fayolle et al., 2011, 2013). While the yields vary among species, and depend on the shape of UV spectrum, typical value is 10^{-3}–10^{-2}. We set the yield for the species without laboratory data to be 10^{-3} for simplicity. We also take into account non-thermal desorption via stochastic heating by high-energy particles (Hasegawa & Herbst, 1993) and reactive desorption (Garrod et al., 2007).

Initial molecular abundance of the disk (see Table 4.1 for selected species) is the same as in Chapter 3, and was obtained by the following. We adopt the so-called low metal values as the elemental abundances (see Table 1 of Aikawa & Herbst, 2001). We integrate the rate equations (similar to Equation (4.1) without the diffusion term, but with Lagrange derivative) along the trajectory of an infalling fluid parcel, which was at the radius of 10^4 AU in the initial prestellar core and reaches 60 AU in the protostellar core of age 9.3×10^4 yr (Aikawa et al., 2008; Masunaga & Inutsuka, 2000). The abundances in this protostellar core model are mostly constant at $r < 100$ AU, where molecules are mainly in the gas phase.

4.3 Result

Here, we describe ice chemistry in turbulent protoplanetary disks. We focus on simple species in Section 4.3.1, while results of complex organic molecules are presented in Section 4.3.2. Upward transport of ices by turbulence also affects the spatial distributions of gas-phase molecules through photodesorption, which will be discussed in Section 4.3.3. CO ans N_2 can be converted to less volatile species and depleted from the gas phase. The mechanism and timescale of such sink effect is analyzed in Section 4.3.4. In the following we discuss the results at 10^6 yr, which is the typical age of T Tauri stars with circumstellar disks, unless otherwise stated.

4.3.1 Simple saturated molecules: CH_3OH and NH_3

The left panels in Figure 4.2 shows the resultant fractional abundances of selected ice-mantle species with respect to hydrogen nucleus in the model without mixing. Although molecules are mostly in the gas phase in our initial abundances, they are adsorbed onto grains in a short timescale ($\sim 10^9/n$ yr) in regions colder than their sublimation temperatures. In the following, we compare the ice abundances at 10^6 yr to the ice abundances right after the initial freeze out, which are essentially the same as the initial gas-phase abundance. H_2CO ice abundance is low compared to the initial value (1.5×10^{-5}) throughout the disk; H_2CO ice is converted to CH_3OH ice via subsequent hydrogenation. In the regions where dust temperature (T_d) is higher than 40 K H_2CO is destroyed by ion-neutral reactions. CH_3OH and NH_3 ices show similar spatial distributions; they are abundant ($\sim 10^{-6}$–10^{-5}) near the midplane, while the abundance is low ($\lesssim 10^{-8}$) in the upper layers because of the strong stellar UV radiation. Solid lines in Figure 4.3 shows the molecular column densities normalized by that of water ice in the model without mixing. Note that water-ice column density stays constant for 10^6 yr in this model, i.e., the water ice abundance near the midplane is $\sim 10^{-4}$ relative to hydrogen nuclei. The column density ratios of CH_3OH and NH_3 ices to water ice are higher than their initial values regardless of a distance from a central star. This is due to their efficient formation in the disk. Once formed, these ices are not destroyed efficiently in the regions where UV photons and X-rays are attenuated. The column density ratio of CH_3OH ice to water ice reaches the maximum at $r \gtrsim 120$ AU, where dust temperatures are less than the sublimation temperature of CO ($\sim$24 K).

Turbulence brings ices to the warm irradiated disk surface, where ices are destroyed via photodissociation and/or photodesorption by the stellar UV photons. On the other hand, gaseous species, such as atomic oxygen, nitrogen, and CO, in the disk surface are transported to the midplane to (re)form the ices and/or other

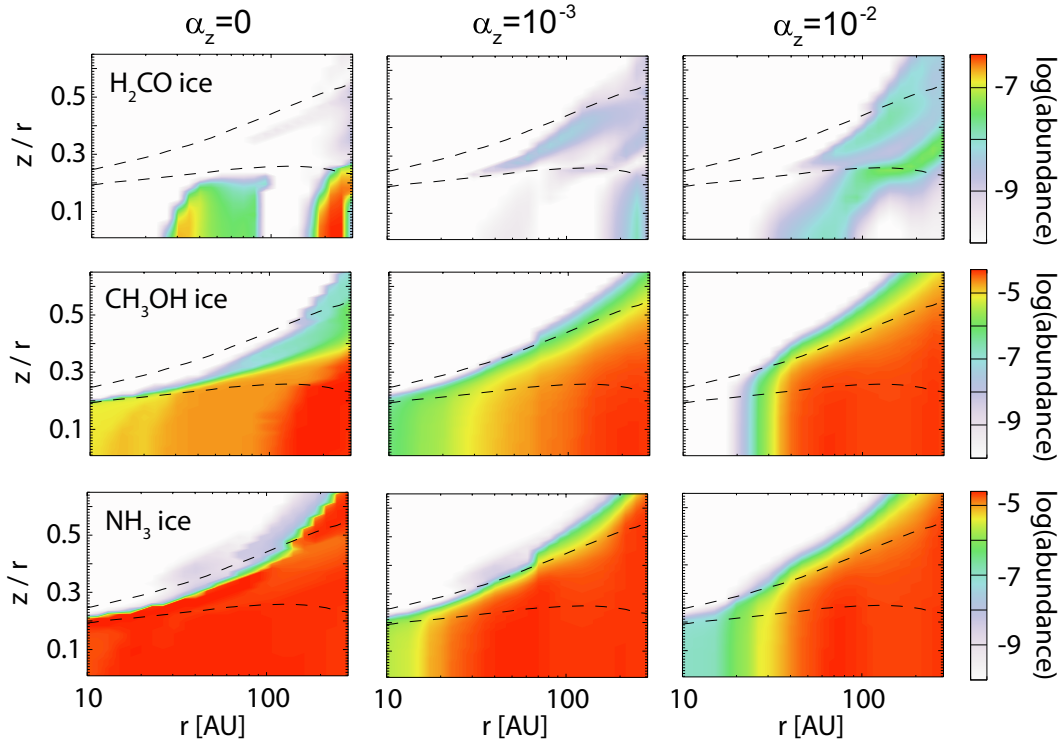

Figure 4.2: Spatial distributions of fractional abundances of selected molecules with respect to hydrogen nuclei. The left, middle and right columns are models with $\alpha_z = 0$, 10^{-3}, and 10^{-2}, respectively. The dashed lines indicate vertical visual extinction of unity and 10.

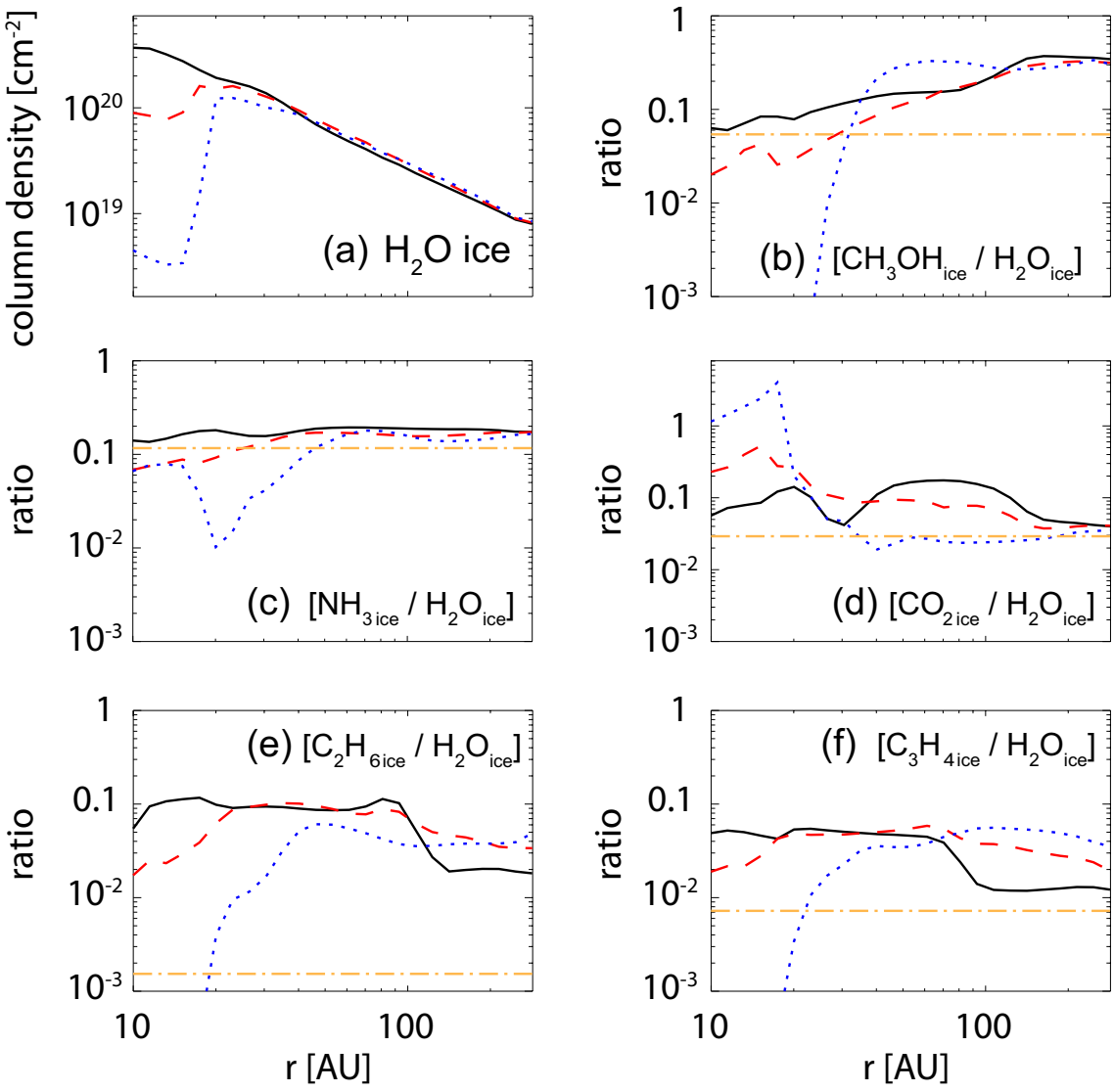

Figure 4.3: Radial profiles of water ice column density (a). Panels (b)-(f) show column densities of selected icy molecules normalized by water ice column density. The solid, dashed, and dotted lines represent the model with $\alpha_z = 0$, 10^{-3}, and 10^{-2}, respectively. The horizontal dash-dotted lines show the initial molecular abundances with respective to water (see Table 4.1).

gaseous species. This cycle changes the ice distributions significantly. The abundances of CH_3OH ice and NH_3 ice decrease with time at $r \lesssim 30$ AU, since hydrogenation on grain surfaces (i.e., reformation of the saturated ices) is prohibited by high dust temperatures. Instead, abundances of CO and N_2 in the gas phase increase with time. At $r \sim$20–30 AU the resultant ice composition is methanol-poor and ammonia-poor compared to the initial composition, because water ice abundance decreases only at $r \lesssim 20$ AU (Figure 4.3). As shown in Chapter 3, the destruction timescale of water ice is limited by their transport timescale in the vertical direction, i.e., $\tau_{\rm ice}^{\rm des} = N_{\rm ice}/\phi_{\rm ice}^{\rm crit}$, where $N_{\rm ice}$ is the ice column density, and $\phi_{\rm ice}^{\rm crit}$ is the flux at a layer above which destruction of a molecule via photoreactions is sufficiently fast. We found destruction timescale of CH_3OH ice and NH_3 ice are similar to that of water ice, e.g., $\tau_{\rm ice}^{\rm des} \sim 6(40) \times 10^4$ yr at $r = 10$ AU, if $\alpha_z = 10^{-2}(10^{-3})$ (Equation 3.33). Note that $\tau_{\rm ice}^{\rm des}$ is comparable to the accretion timescale, $\tau_{\rm acc} = r/v_{\rm acc}$ (see discussions in Section 3.5.3). At $r > 30$ AU, lower dust temperatures allow reformation of CH_3OH and NH_3 ices. Turbulence continuously brings them to the disk surface, where destruction and supply from the midplane of the ices are balanced; the ices are abundant even at $A_V = 1$ mag from the disk surface, if $\alpha_z = 10^{-2}$.

4.3.2 Complex organic molecules

When dust temperature is warm ($\gtrsim$30 K), radical-radical association reactions become important, as radicals can be mobile on grain surfaces, while hydrogen atoms tend to evaporate rather than react with radicals (Garrod & Herbst, 2006; Garrod et al., 2008). We focus on $HCOOCH_3$ and CH_3OCH_3 as representatives of complex organic molecules, since they are often detected in high-mass and low–mass protostellar envelopes (e.g., Nummelin et al., 2000; Cazaux et al., 2003). Regardless of the mixing strength, $HCOOCH_3$ ice and CH_3OCH_3 ice mainly form via the following grain-surface reactions in our models:

$$\mathrm{HCO} + \mathrm{CH_3O} \rightarrow \mathrm{HCOOCH_3}, \tag{4.9}$$

$$\mathrm{CH_3} + \mathrm{CH_3O} \rightarrow \mathrm{CH_3OCH_3}. \tag{4.10}$$

The left panels of Figure 4.4 shows the spatial distributions of abundances of $HCOOCH_3$ ice and CH_3OCH_3 ice in the model without mixing. These complex species are moderately abundant (10^{-8}–10^{-7}) near the midplane in specific radii; $HCOOCH_3$ ice is most abundant in the midplane of $r = 20$–30 AU, while CH_3OCH_3 ice is abundant in the outer regions ($r = 30$–90 AU). At $r \lesssim 20$ AU, even heavy radicals tend to evaporate rather than react, while at $r \gtrsim 90$ AU, hydrogenation of the radicals to form simple molecules becomes more efficient.

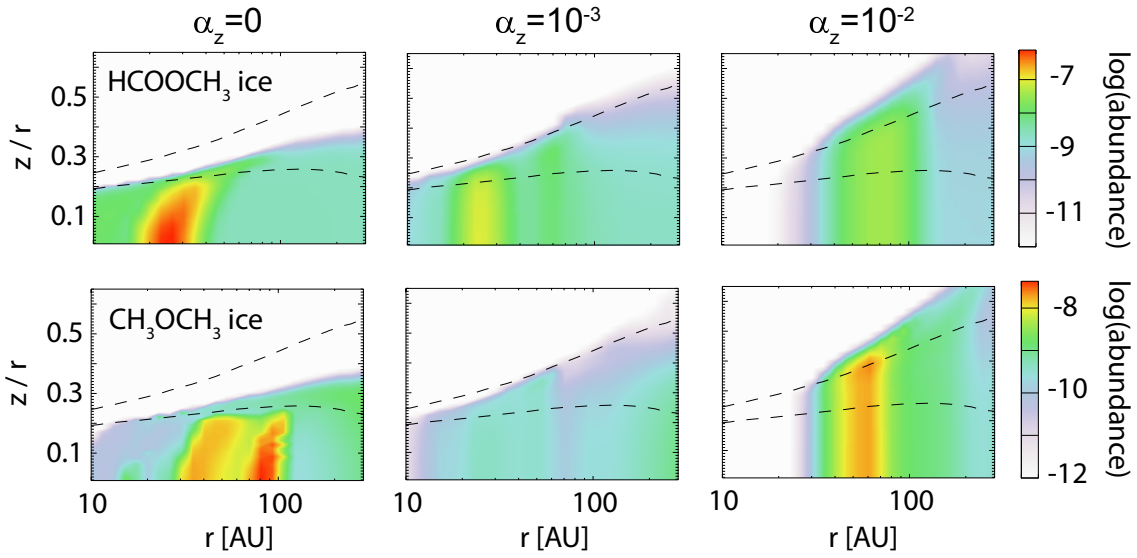

Figure 4.4: Spatial distributions of $HCOOCH_3$ ice (top) and CH_3OCH_3 ice (bottom) abundances. Other details are the same as Figure 4.2.

Figure 4.5 shows the temporal variations of their abundances at $r = 25$ AU and 80 AU in the model without mixing. At $r = 25$ AU, $HCOOCH_3$ ice abundance increases in the timescale of several 10^4 yr. CH_3O radical is mainly formed via the hydrogenation of H_2CO on grain surfaces, while HCO radical is mainly formed by the surface reaction of

$$H_2CO + OH \rightarrow HCO + H_2O. \tag{4.11}$$

OH radical is mainly formed by the following pathway: CO $\xrightarrow{He^+}$ O $\xrightarrow{grain}$ O_{ice} $\xrightarrow{HNO_{ice}}$ OH_{ice}. We note it produces OH more efficiently than photodissociation of water ice by cosmic-ray induced photons, which is the dominant UV source in the midplane, in our fiducial models. If we assume $N_p = N_{layer}$ in Equation (4.5), OH production via water photodissociation becomes as efficient as O + HNO. At $r \gtrsim 30$ AU, hydrogenation of HCO ice suppress the $HCOOCH_3$ ice formation. On the other hand, at $r = 80$ AU, CH_3OCH_3 ice abundance increases at $t = 2 \times 10^5$ yr, when HNO ice abundance falls. Until then, HNO is the main reaction partner of CH_3 (Garrod & Herbst, 2006). At $r \lesssim 30$ AU, the fall of HNO ice abundance does not occur in 10^6 yr, probably because the higher dust temperatures suppress the conversion of HNO to NH_3. These explain the difference in the spatial distributions of $HCOOCH_3$ and CH_3OCH_3 ices; HNO ice enhances the formation of the former, but suppresses the formation of the latter.

Effect of turbulent mixing on the formation of complex organic molecules are twofold: (1) transport of ices from the midplane to the surface and (2) transport of atomic hydrogen from the surface to the midplane. The former enhances the

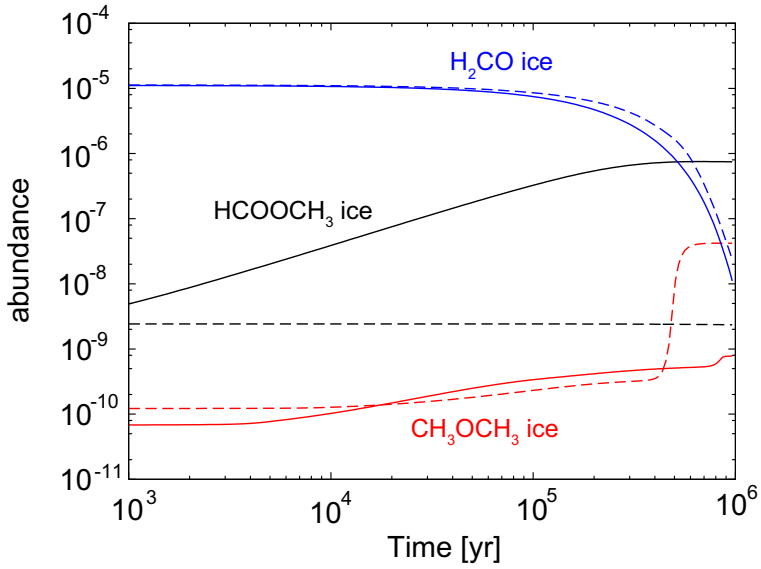

Figure 4.5: Temporal variations of abundances of $HCOOCH_3$ ice (black), CH_3OCH_3 ice (red), and H_2CO ice (blue) in the model without mixing at the midplane of $r = 25$ AU (solid) and $r = 80$ AU (dashed).

formation of complex molecules in the disk surface, while the latter enhances the hydrogenation of radicals in the midplane to suppress the formation of complex molecules (but see Section 4.4.1). As a result, complex organic molecules are mainly formed in the region with A_V = a few mag, and turbulence brings them to the deeper layers into the disk. In the model with $\alpha_z = 10^{-2}$, the abundances of $HCOOCH_3$ ice and CH_3OCH_3 ice reach the maximum at $r = 60$ AU. In the inner disk surface, radicals tend to desorb thermally rather than react, while in the outer disk surface, hydrogenation of radicals becomes more efficient.

Figure 4.6 shows temporal variations of the abundances of the complex species in the model with $\alpha_z = 10^{-2}$ at various disk height at $r = 60$ AU. In the disk surface, CH_3, CH_3O, and OH radicals are mainly formed by the photodissociation of CH_3OH and water on grain surfaces, while HCO ice is mainly formed by Reaction (4.11). In the disk surface, $HCOOCH_3$ ice is temporally abundant ($\sim 10^{-7}$) at $t \lesssim 5 \times 10^3$ yr, when H_2CO ice is still abundant. After $t \sim 10^5$ yr, the abundances of the complex species do not significantly vary with time in the disk surface. The nearly steady-state values of $\sim 3 \times 10^{-8}$ are determined by the the balance between destruction rate by photoreactions and formation rate. The latter is determined by the competition between radical-radical reactions and hydrogenation of radicals, the rates of which are dependent on dust temperature and the abundance of atomic hydrogen. The terminal abundances of complex molecules are not high compared to those in the model without mixing, despite much larger radical formation rates

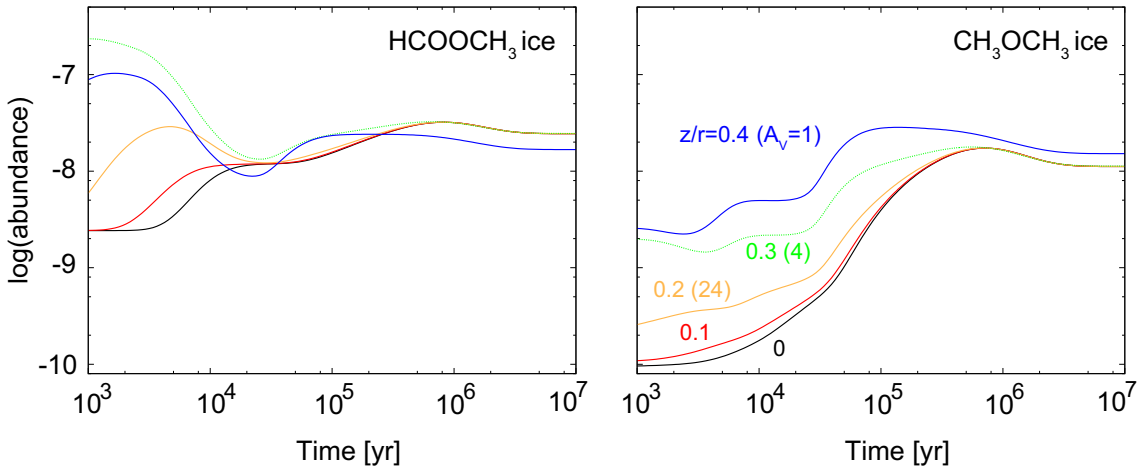

Figure 4.6: Temporal variations of abundances of $HCOOCH_3$ ice (left) and CH_3OCH_3 ice (right) in the model with $\alpha_z = 10^{-2}$ and $r = 60$ AU at various heights from the midplane. The values in bracket are the vertical visual extinction from the surface.

in the disk surface, because the abundance of atomic hydrogen is also high in the disk surface. On the other hand, in the midplane, the abundances of the complex molecules increase with time in the timescale of $\sim 10^5$ yr, which is comparable to the transport timescale of the forming molecules from the surface to the midplane, L^2/D_z, where L is the distance between the disk surface ($A_V \sim 1$ mag) and midplane. After $t \gtrsim 10^6$ yr, the abundances in the midplane and surface are almost the same. In the case of $\alpha_z = 10^{-3}$, in which the transport timescale is longer ($\sim 10^6$ yr at $r = 60$ AU), disk surface is slightly abundant in complex molecules compared to the midplane at $t = 10^6$ yr.

Figure 4.7 shows the column densities of the complex species normalized by that of CH_3OH ice, which is a parent molecule of the complex species. In the model without mixing, the maximum column density ratios for $HCOOCH_3$ ice and CH_3OCH_3 ice are 0.05 and 10^{-3}, respectively, which are much higher than the initial values (4×10^{-4} and 10^{-5}). In the model with mixing, the maximum column density ratios are smaller than in the model without mixing, again because of abundant H atom both in the disk surface and the midplane.

Our results suggest that the main formation site of complex organic molecules in disks depends on the turbulent strength; in the disk with weak turbulence ($\alpha_z \leq 10^{-3}$), they are mainly formed near the midplane, while in the disk with strong turbulence ($\alpha_z = 10^{-2}$), they are mainly formed in the disk surface and transported into the deeper layers. These two cases may be distinguished by deuterium-to-hydrogen (D/H) ratios of the complex molecules. Although we do not show their D/H ratios in the current work, in the former case the D/H ratios should be similar to the molec-

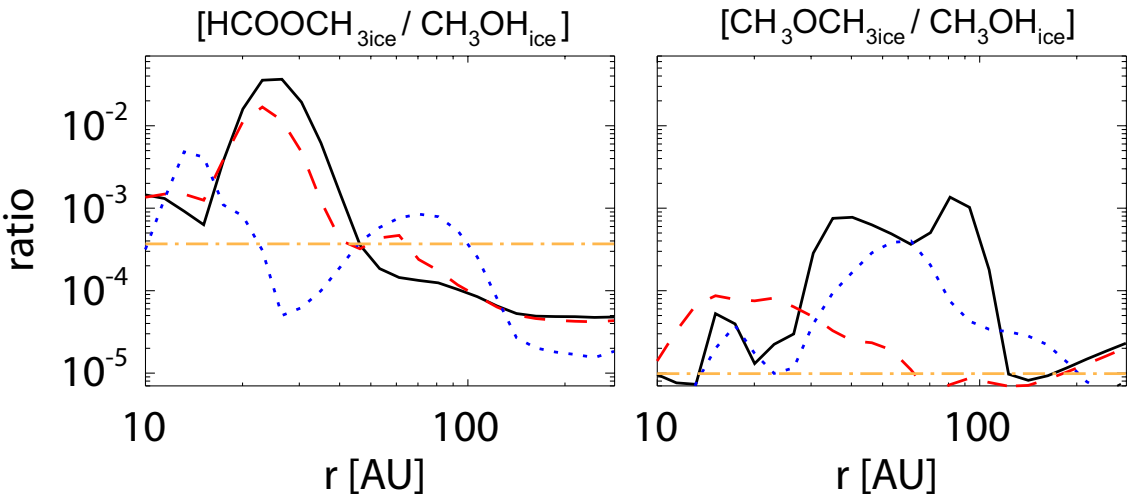

Figure 4.7: Radial profiles of column densities of $HCOOCH_3$ ice (left) and CH_3OCH_3 ice (right), normalized by CH_3OH ice column density. The solid, dashed, and dotted lines represent the model with $\alpha_z = 0$, 10^{-3}, and 10^{-2}, respectively. The horizontal dash-dotted lines show the initial $HCOOCH_3/CH_3OH$ (left) and CH_3OCH_3/CH_3OH (right) abundance ratios (see Table 4.1).

ular D/H ratio in the initial disk; if the initial disk inherits the high molecular D/H ratio of cold cloud cores, the complex molecules formed there would also be highly deuterated. In the case of strong turbulence, on the other hand, their D/H ratios would be lower than the interstellar values, since temperature in the disk surface is higher than that in the cloud core (Chapter 3).

4.3.3 Gas-phase species

Ice mantle species are desorbed to the gas phase thermally and/or non-thermally. It is possible to access the ice chemistry in disks thorough observing emission lines of the gas-phase species (Hogerheijde et al., 2011), while direct observational study of ices in disks is not straightforward because of the contamination of foreground components and geometry of the objects (e.g., Aikawa et al., 2012). In this subsection we analyze the gas phase abundance of H_2CO and CH_3OH. H_2CO is one of the most complex molecules detected in protoplanetary disks. CH_3OH has not yet been detected in the disks, but is obviously an important target in ongoing ALMA observations.

The transport of ices affects the abundances of gaseous species in the disk surface through photodesorption, while transport of the gas from the upper layers keeps a fraction of CH_3OH and H_2CO in the gas phase ($n_i/n_{\rm H} = x_i < 10^{-12}$) in the midplane (see e.g., Semenov et al., 2006; Aikawa, 2007). Figure 4.8 shows that in the model with $\alpha_z = 10^{-2}$, gaseous CH_3OH is abundant in the disk surface ($A_V \sim 2$ mag) of

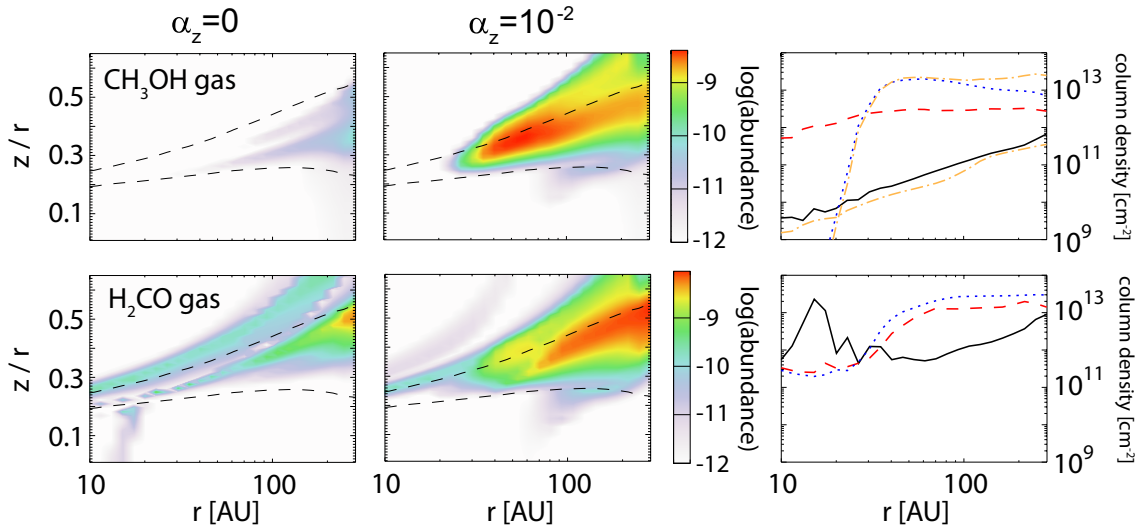

Figure 4.8: Spatial distributions of the abundances (left and middle) and column densities (right) of gaseous CH_3OH and H_2CO.

$r \lesssim 200$ AU. There, CH_3OH abundance is determined by a local balance between photodissociaition and photodesorption:

$$F_{\rm FUV}\sigma_{\rm Ly\alpha}n^{\rm g}_{\rm CH_3OH} = F_{\rm FUV}\pi a^2\frac{n^{\rm s}_{\rm CH_3OH}}{n_{\rm ice}}Y n_{\rm d}, \tag{4.12}$$

if dust grains are covered by more than one monolayer of ice (i.e., $n_{\rm ice} \geq n_{\rm d}N_{\rm site} \sim 10^{-6}n_{\rm H}$, see Equations (4.7) and (4.8)). The parameter $\sigma_{\rm Ly\alpha}$ is the photodissociation cross section of methanol at Lyα wavelength (1.4×10^{-17} cm^2; van Dishoeck et al., 2006), while $n^{\rm g}_{\rm CH_3OH}$ and $n^{\rm s}_{\rm CH_3OH}$ are the number density of methanol in the gas phase and in ice mantles, respectively. We found that the photodesorption rate is about twice higher than the rate of reactive desorption if $\sim$1 % of the (re)produced methanol ice is desorbed. From Equation (4.12), the gaseous CH_3OH abundance is

$$x^{\rm g}_{\rm CH_3OH} = 6\times10^{-9}\left(\frac{n^{\rm s}_{\rm CH_3OH}/n_{\rm ice}}{0.1}\right)\left(\frac{\pi a^2 x_d}{6\times10^{-22}\,{\rm cm}^2}\right)\left(\frac{Y}{10^{-3}}\right)\left(\frac{\sigma_{\rm Ly\alpha}}{10^{-17}\,{\rm cm}^2}\right)^{-1}. \tag{4.13}$$

It is clear that the abundance is independent of UV photon flux and number density of the gas, but is dependent on ice compositions. A similar analysis is previously performed for water vapor in disks (Dominik et al., 2005) and in molecular clouds (Hollenbach et al., 2009). At $r \gtrsim 200$ AU, on the other hand, ion-neutral reactions are the dominant destruction path of gaseous CH_3OH; the abundance is weakly dependent on number density of the gas ($x^{\rm g}_{\rm CH_3OH} \propto n^{-0.5}$).

While CH_3OH is efficiently formed only on grain surfaces, H_2CO is mainly formed

by the gas-phase reaction of CH_3 + O (e.g., Walsh et al., 2014). Nevertheless gas-phase H_2CO abundance is also enhanced in the disk surface (Figure 4.8), because CH_3 ice is formed by the photodissociation of CH_3OH ice and evaporates at $T_d \gtrsim 25$ K.

Radial profiles of the column densities of gaseous H_2CO and CH_3OH are shown in the right panels of Figure 4.8. In the model without mixing, they increase with radius except for H_2CO at $r \lesssim 30$ AU. When mixing is considered, the column densities are greatly enhanced at $r \gtrsim 30$ AU, while they decrease in the inner disks (see Section 4.3.1). Then the radial column density profiles are ring-like in the models with $\alpha_z = 10^{-2}$ as recently suggested by the SMA observations of H_2CO in Herbig Ae star HD 163296 (Qi et al., 2013). In our model, the inner edge of the ring is determined by the efficiency of CO hydrogenation on grain surfaces. We found analytical expression of the column density of gaseous CH_3OH, which is depicted by dot-dashed lines in Figure 4.8. The analytical expression and its derivation are given in Appendix.

As in the case of methanol, photodesorption is the main mechanism to desorp complex organic species into the gas phase in our models. The maximum abundances (10^{-12}–10^{-11}) and column densities ($\sim 10^{10}$ cm^{-2}) are not high even in the model with $\alpha_z = 10^{-2}$, since they are not dominant species in ices. Our model predicts that more complex molecules than CH_3OH in the gas phase, such as CH_3OCH_3, are much less abundant than CH_3OH and H_2CO. This result agrees with Walsh et al. (2014).

4.3.4 Carbon and nitrogen depletion in the gas phase

CO freeze-out in the midplane with $T_d \lesssim 20$–25 K is now established in both theoretical models and observations (Aikawa et al., 1996; Qi et al., 2011, 2013). In theoretical models, however, CO could be depleted from the gas phase at higher dust temperatures; carbon is locked in ices as carbon-chain molecules and CO_2 in the regions where T_d is greater than the sublimation temperature of CO, but lower than that of the latter species. It is called carbon sink (Aikawa et al., 1997). Recently, Favre et al. (2013) found that CO abundance in the warm layer ($T > 20$ K) of TW hya is significantly lower ($(0.1 - 3) \times 10^{-5}$) than the canonical value of 10^{-4}; this may imply that sink mechanism is really working in TW hya. The model of Aikawa et al. (1997) showed that nitrogen is also locked in ices as NH_3 in the regions where $T_d > 25$ K.

Figure 4.9 shows the spatial distributions of abundances of CO and N_2 in our models. In the model without mixing, we can see that CO and N_2 in the gas phase are significantly depleted even at $t = 10^5$ yr in a layer, where stellar UV is heavily attenuated, but ionization rate is high due to X-ray. At $t = 10^6$ yr, carbon and nitrogen are significantly depleted throughout the disk, except for the irradiated disk

surface and warm inner midplane. While carbon and nitrogen depletion is common in previous disk chemical models, to the best of our knowledge, their time scales have not been discussed in detail. To understand carbon and nitrogen chemistry more deeply, we analyze the timescale of the sink mechanisms and the effect of turbulent mixing in this subsection.

Timescale of the carbon sink mechanism is limited by the destruction timescale of CO by helium ion:

$$\mathrm{CO} + \mathrm{He}^+ \rightarrow \mathrm{C}^+ + \mathrm{O}. \tag{4.14}$$

Carbon ion reacts with other carbon-bearing species, such as CH_4, followed by recombination with an electron or a negatively charged grain to form carbon-chain molecules. On the other hand, atomic oxygen is adsorbed onto dust grains and is converted to CO_2 and other O-bearing species (Figure 4.3). Helium ion is produced by the ionization of atomic helium, and destroyed mainly by CO (Reaction (4.14)) as long as $x_{\mathrm{CO}} > 0.5 x_{\mathrm{N_2}}$ and $x_{\mathrm{CO}} > 3 \times 10^{-6}$. Then characteristic timescale of carbon depletion, τ_{CO}, is

$$\tau_{\mathrm{CO}} = \frac{1}{\beta x_{\mathrm{He^+}}} \approx \frac{x_{\mathrm{CO}}}{\xi_{\mathrm{He}} x_{\mathrm{He}}} \approx 5 \times 10^5 \left(\frac{x_{\mathrm{CO}}}{3.5 \times 10^{-5}} \right) \left(\frac{\xi_{\mathrm{He}}}{2.5 \times 10^{-17}\,\mathrm{s^{-1}}} \right)^{-1} \mathrm{yr}, \tag{4.15}$$

where ξ_{He} and β are the ionization rate of He atom and the rate coefficient of Reaction (4.14), respectively. It should be noted that τ_{CO} is proportional to CO abundance. In other words, once CO abundance drops after $t > \tau_{\mathrm{CO}}$, sink effect is accelerated. We can see this behavior in Figure 4.10, which shows temporal variations of fractions of elemental carbon and nitrogen in the form of selected species at the midplane of $r = 25$ AU, where $T_{\mathrm{d}} \sim 40$ K, in the model without mixing. The timescale τ_{CO} is inversely proportional to the ionization rate of He. In our models, cosmic-ray ionization rate of H_2 is 5×10^{-17} s^{-1} referring to Dalgarno (2006). If we set the cosmic-ray ionization rate of H_2 to be 1.3×10^{-17} s^{-1}, which is commonly used value in astrochemical models, τ_{CO} is longer than 10^6 yr. It should also be noted that τ_{CO} is proportional to the initial CO abundance. In our model, less than half of carbon is initially in CO, since considerable part of carbon is in H_2CO and CH_4. Such low CO abundance has been recently observed in the inner envelopes of low-mass protostars, where $T > 25$ K (Yildiz et al., 2012), and thus is indeed possible as an initial condition of the disk. If we start our model with a higher abundance of CO, however, τ_{CO} becomes longer.

In Figure 4.10, we can see the sharp drop of N_2 abundance after CO abundance considerably decreases ($\sim 10^{-6}$). Nitrogen depletion in the gas phase occurs by the following pathway: $\mathrm{N_2} \xrightarrow{\mathrm{H_3^+}} \mathrm{N_2H^+} \xrightarrow{\mathrm{grain,\,e^-}} \mathrm{NH}$. Once NH is formed, it is adsorped onto dust grains, followed by subsequent hydrogenation to form NH_3 (Willacy, 2007).

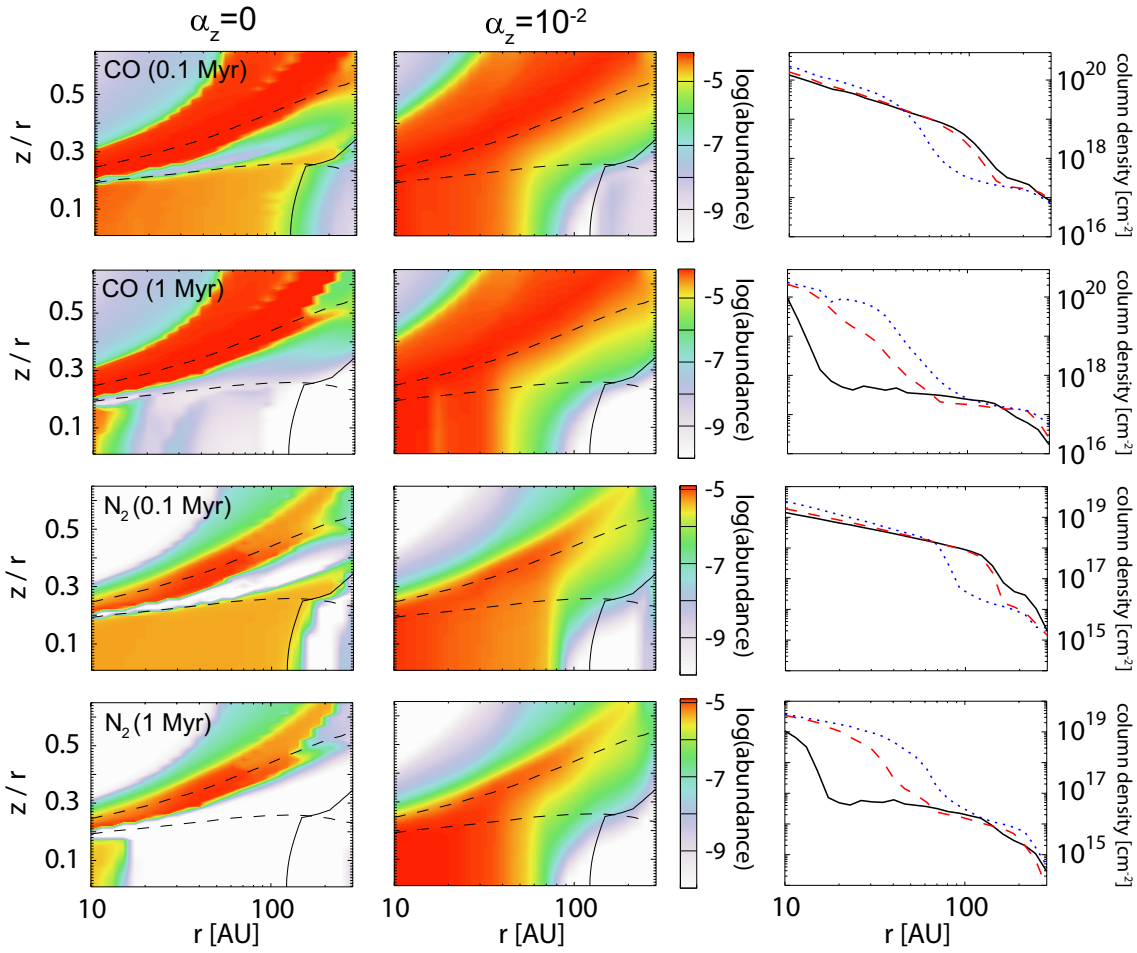

Figure 4.9: Spatial distributions of the abundances (left and middle) and column densities (right) of CO and N_2 at 10^5 yr and 10^6 yr. In left and middle panels, the solid lines indicate dust temperature of 24 K, which nearly corresponds to sublimation temperature of CO. while the dashed lines indicate vertical visual extinction of unity and 10.

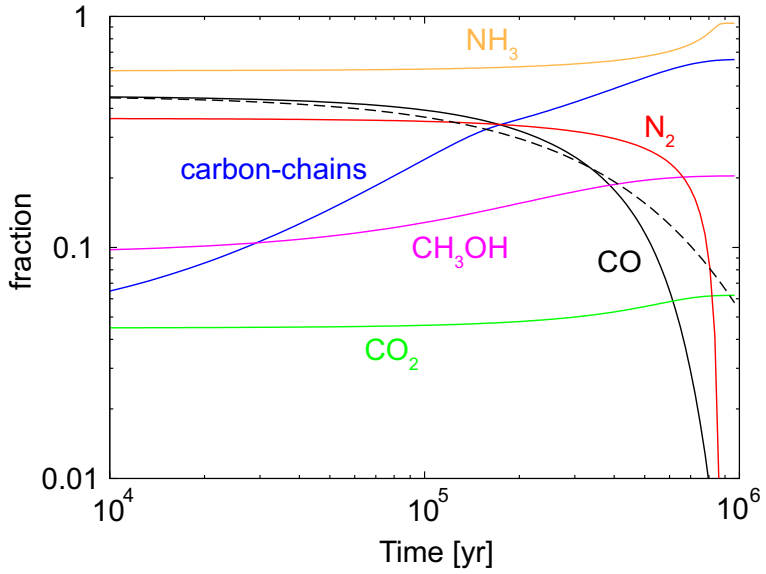

Figure 4.10: Temporal variations of a fraction of elemental carbon and nitrogen in the form of selected species at the midplane of $r = 25$ AU in the model without mixing. Dust temperature is ∼40 K. The dashed line depicts the temporal variation given by $f_{\rm CO}\exp(-t/\tau_{\rm CO})$, where $f_{\rm CO}$ is the initial fraction of carbon in CO.

Note that the above path is not efficient when CO is abundant; most N_2H^+ reacts with CO and reforms N_2, due to higher proton affinity of CO than N_2. Although N_2 is also destroyed by He^+, the products, N atom and N^+, mainly cycle back to N_2.

Effect of turbulent mixing on carbon depletion in the gas phase varies with disk radius. In the inner disks, where $\tau_{\rm CO} > \tau_{\rm ice}^{\rm des}$, transport of ices from the midplane to the surface and photoreactions suppress the carbon depletion in the gas phase; in the model with $\alpha_z = 10^{-2}$, significant carbon depletion does not occur at $r \lesssim 50$ AU in 10^6 yr. In the midplane of the outer regions, on the other hand, vertical mixing increases atomic H abundance and enhances hydrogenation of CO on grain surfaces; in the model with $\alpha_z = 10^{-2}$, conversion of CO into CH_3OH occurs in the timescale of only several 10^4 yr at the midplane of $r \sim 50$–100 AU, which is much shorter than $\tau_{\rm CO}$. In the upper layers, where stellar UV is heavily attenuated, but Reaction (4.14) is enhanced by X-ray ionization, the sink mechanism is effective, but CO distribution is smoothed out by mixing, since the transport timescale over such layer is shorter than the depletion timescale.

4.4 Discussion

4.4.1 Cometary molecules

Table 4.2 summarizes observed abundances of selected species with respect to water in cometary coma (Mumma & Charnley, 2011, and reference therein) and low-mass protostellar envelopes (Öberg et al., 2011). Table 4.2 also lists the column density ratio of icy molecules to water ice in the models with $\alpha_z = 0$ and 10^{-2}, and our initial abundances for disk chemistry (core). We restrict our data to $r = 20$–30 AU, where our model with $\alpha_z = 10^{-2}$ reproduce the cometary HDO/H_2O ratio of 10^{-3}–10^{-4}, regardless of the initial HDO/H_2O ratio (Chapter 3). We do not discuss CO and CH_4 here, because they are mostly in the gas phase in our model at $r = 20$–30 AU, where $T_d > 25$ K. In reality, H_2O ice matrix can trap these highly volatile species and prevent them from sublimating entirely at their sublimation temperatures (e.g, Collings et al., 2004). Our current model does not consider such trapping by water ice.

As mentioned in the introduction, observed abundances of CH_3OH, NH_3 and CO_2 in comets are lower than the median abundances in the low-mass protostellar envelopes. The model with $\alpha_z = 10^{-2}$ reasonably reproduces abundances of NH_3 and CH_3OH in comets, while the model without mixing fails. Although our initial abundances of NH_3 and CH_3OH are larger than those observed in ptorostellar envelopes by a factor of around two, this discrepancy would not affect the result. Then, our model suggests the possibility that the lower NH_3 and CH_3OH abundance in comets could be established in the solar nebula via the destruction and reformation of the interstellar ices. Note, however, that we can not rule out the possibility that the ice composition in the parental core of the Solar nebula was methanol-poor and ammonia-poor compared to the median abundances in the low-mass protostellar envelopes. The model with mixing also better reproduces the cometary C_2H_6 abundance. On the other hand, our disk model both with and without mixing reasonably reproduce cometary CO_2 abundance. One caution is that our initial composition is significantly CO_2-poor compared to that observed in ptorostellar envelopes. The CO_2 abundance of the disk could be higher, if we start with higher CO_2 abundances.

Let us move on to complex organic molecules. Complex molecules, such as $HCOOCH_3$, have been detected only in comet Hale-Bopp, which is the brightest comet in the past several decades. The model without mixing reasonably reproduces the abundances of $HCOOCH_3$, CH_3CHO, and NH_2CHO, while the model abundance of HCOOH (and possibly CH_3OCH_3) is lower than observations. On the other hand, the model with mixing has significantly lower abundances than those in comets except for HCOOH; as mentioned in Section 4.3.2, dust temperatures at disk surfaces of

Table 4.2: Molecular Abundances of Cometary Coma and Low-Mass Protostellar Envelopes

Species	Comet[1]	Protostar[2]	Model[3]		
			($\alpha_z = 0$)	($\alpha_z = 10^{-2}$)	Core
H_2O	100	100	100	100	100
CO_2	2–30	29	4–14	4–19	3
NH_3	0.2–1.4	5	16–18	1–4	12
CH_3OH	0.2-7	3	8–12	0.004–4	6
C_2H_6	0.1-1.7	...	9–10	0.4–1.6	0.2
$HCOOCH_3$	0.08	...	0.1–0.2	$(0.04–4) \times 10^{-4}$	0.002
CH_3OCH_3	< 0.5	...	$(0.1–3) \times 10^{-3}$	$(0.007–4) \times 10^{-4}$	5×10^{-5}
HCOOH	0.09	...	$(0.8–3) \times 10^{-3}$	0.1–0.2	8×10^{-4}
CH_3CHO	0.02	...	0.04	$< 10^{-5}$	0.05
NH_2CHO	0.015	...	0.07–0.1	$(0.2–3) \times 10^{-3}$	0.08

$r \lesssim 60$ AU are too high to form complex molecules efficiently, while in the midplane, higher abundance of atomic hydrogen than in the model without mixing suppress the formation of complex molecules. Then, it is difficult to reproduce cometary abundances of both simple and complex molecules in a single model.

We note here that out model might overestimate the hydrogenation rate of radicals, and thus underestimate formation rate of complex molecules. Fuchs et al. (2009) showed that hydrogen atoms can penetrate into top four monolayers of a CO ice matrix at maximum at the ice temperature of 12 K, although the penetration depth slightly increase with temperature. On the other hand, Öberg et al. (2009c) estimated that surface reactions are at most twice as efficient as bulk reactions in producing complex molecules. These laboratory experiments suggests that radical-radical reaction could occur even in bulk ice layers, but hydrogenation by H atom accreting onto the grain surface is effective only in the surface several layers. In this study, we adopt a two-phase model, in which a layered structure of ice mantles is not considered, and the bulk of ices is chemically active, i.e., adsorbed atomic hydrogen onto grain surfaces can react with all species in the bulk of ice, which hampers the formation of complex organic molecules. Consideration of layered structure of ice and discrimination of the surface chemistry from bulk ice chemistry (Garrod, 2013) are important to simulate synthesis of complex molecules in disks more accurately.

4.4.2 Comparisons with previous models

SW11 studied effect of radial and vertical mixing on disk chemistry. Here we briefly compare our results with SW11. The comparison is not straightforward, however, because both chemical and physical models are different between the two models. Although SW11 utilized a reaction network based on Garrod & Herbst (2006) with various modifications like this work, adopted parameters, such as the diffusion-to-desorption energy ratio for grain surface reactions, are different; we assume the ratio of 0.5, while SW11 assumed the ratio of 0.77. The adopted disk physical model in SW11 is colder than that we use in this work; a maximum dust temperature in the midplane is less than 40 K in SW11. Thus they do not report depletion of ice (e,g., H_2O and CH_3OH) found in the inner disks of our models. In the following, we compare the effect of mixing on radial column density profiles in the regions where midplane dust temperature is less than 40 K ($r \gtrsim 40$ AU in our model) between the two models.

SW11 found that the column densities of gaseous CH_3OH is enhanced by up to two orders of magnitude, while that of gaseous H_2CO is not strongly affected by mixing. Our model predicts that the abundances of both species are enhanced through upward transport of ices containing CH_3OH, followed by photochemisty. Although we do not have reasonable explanation for this discrepancy, we note that regardless of mixing strength the gas-phase H_2CO column density in SW11 is comparable to that in our model with $\alpha_z = 10^{-2}$. Abundant H_2CO in SW11 may have hidden the enhancement by mixing. SW11 also found complex organic species, HCOOH ice and CH_3CHO ice, are more abundant in the model with mixing than in the model without mixing. Our models confirm their results.

4.4.3 Photodissociation rates of icy molecules

Interaction between UV photons and ices is the essential process for chemistry in star-forming regions; however, details of ice photolysisy are poorly understood in the current stage. In this subsection, we briefly discuss the effect of our assumptions in the calculations of photodissociation rates of ices on the results presented in Section 4.3.

In our fiducial models, we assumed that only the uppermost monolayer of the ice mantles can be dissociated as an outcome of photoabsorption, while photofragments immediately recombine in the deeper layers. This assumption may lead to an underestimate of the photodissociation rates of ices, if the recombination probability of photofragments in the deeper layers is much less than unity. As the opposite extreme, we have run the calculations with $N_{\rm p} = N_{\rm layer}$ instead of Equation (4.6), assuming

that photofragments do not recombine even in the deepest layers. If all oxygen is in water ice, $N_{\rm layer}$ is $\sim$50 monolayers in our models. We found that the column densities of the molecules presented in Section 4.3 are not sensitive to the assumption in $N_{\rm p}$; the difference of the column densities is mostly within a factor of three, regardless of the mixing strength. CH_3OCH_3 ice in the model without mixing is most sensitive to $N_{\rm p}$; the column density increases by about one order of magnitude relative to the fiducial model, due to the increased formation rate of CH_3 radical. In the model with $\alpha_z = 10^{-2}$, on the other hand, the column densities of $HCOOCH_3$ and CH_3OCH_3 ices slightly decrease relative to the fiducial model, because the abundances of the simpler ices decrease in the disk surface due to the efficient photodissociation.

We also assumed that the photodissociation cross sections of icy molecules are the same as those of corresponding gaseous molecules, except for water and CO_2 ices, in our fiducial models. We have preformed a calculation in which the adopted cross sections of icy molecules are lowered by a factor of ten; it also corresponds to the case that most of the photofragments recombine even in the uppermost monolayer. We confirmed that this does not affect the results of the simple molecules significantly. On the other hand, in the model with $\alpha_z = 10^{-2}$, column densities of $HCOOCH_3$ and CH_3OCH_3 ices decrease by up to a factor of five relative to the fiducial model, due to the decreased radical formation rates in the disk surface.

4.5 Conclusion

We have investigated ice chemistry in turbulent protoplanetary disks surrounding a T Tauri star, focusing on carbon and nitrogen bearing molecules. We have solved chemical rate equations with the diffusion term, mimicking the turbulent mixing in the vertical direction. Turbulence brings ice-coated dust grains from the midplane to the surface, where the strong UV radiation field and higher dust temperature activate ice chemistry. Transport of atomic hydrogen from the disk surface to the midplane also plays an important role of determine ice chemistry. Our main conclusions are as follows.

1. Upward transport of ices decreases the abundance of saturated ice molecules, CH_3OH and NH_3, in the inner disks ($r \lesssim 30$ AU), because warm dust temperatures prohibit their reformation via the hydrogenation on grain surfaces. At $r \sim$20–30 AU the resultant ice composition is methanol-poor and ammonia-poor compared to the initial composition, because water ice abundance decreases only at $r \lesssim 20$ AU. This contrasts with the model without mixing, where the ice composition is methanol-rich and ammonia-rich compared to the initial composition.

2. We found that turbulent mixing affects synthesis of complex organic molecules in the two ways: (1) transport of ices from the midplane to the surface and (2) transport of atomic hydrogen from the surface to the midplane. The former enhances the formation of complex molecules in the disk surface, while the latter enhances the hydrogenation of radicals and thus suppresses the formation of complex molecules in the midplane. As a result, complex molecules are mainly formed in the disk surface in the model with strong mixing ($\alpha_z = 10^{-2}$). In the model with $\alpha_z \lesssim 10^{-3}$, on the other hand, the complex molecules are mainly formed in the midplane. We also found that the terminal abundances of the complex molecules, $HCOOCH_3$ and CH_3OCH_3, in the model with $\alpha_z = 10^{-2}$ are not high compared to those in the model with $\alpha_z \lesssim 10^{-3}$, despite much larger radical formation rates in the disk surface, because of abundant H atom both in the disk surface and the midplane (but see Section 4.4.1).

3. It is known that comets are depleted in simple saturated species relative to water compared the median abundances of the ices in low-mass protostellar envelopes. The model with $\alpha_z = 10^{-2}$ reasonably reproduces the abundances of simple molecules in comets, while the model without mixing fails. Our results suggest that the observed deficiency of simple saturated species in comets might imply the destruction and reformation of the interstellar ices in the solar nebula. However, the model without mixing better reproduces the abundances of complex molecules in comets. Then, it is difficult to reproduce cometary abundances of both simple and complex molecules in a single model. To resolve this issue, we need to introduce layered structure of ice mantles in our model, considering that atomic hydrogen cannot penetrate deeply in ice mantles, according to laboratory experiments.

4. Upward transport of ices enriches icy molecules in the disk surface, where destruction by photoreactions and supply from the deeper layers are balanced. It also affects the abundances of gaseous species through photodesorption. In the model with $\alpha_z = 10^{-2}$, radial profiles of column densities of H_2CO and CH_3OH in the gas phase are ring-like. The inner edge of the ring is determined by the efficiency of CO hydrogenation on grain surfaces. The analytical expression of radial profiles of CH_3OH column density is given in Appendix, which would be useful for analyzing (near) future radio observations by ALMA.

5. In the disk chemical models, it often occurs that carbon and nitrogen are locked in ices even in the regions where dust temperature is greater than the sublimation temperatures of CO and N_2 ($\sim$25 K). Recent observation by Favre et al. (2013) suggests that such chemistry is really working in TW hya. We

found that characteristic timescale of carbon depletion in the gas phase ($\tau_{\rm CO}$) is given by Equation (4.15), and once CO abundance considerably drops after $t > \tau_{\rm CO}$, depletion is accelerated. Nitrogen depletion occurs only after CO abundance considerably decreases ($\sim 10^{-6}$). Effect of turbulent mixing varies with disk radius and height.

Appendix A

Three body association and collisional dissociation reactions

Table A.1 lists the three body association reactions, while Table A.2 lists the collisional dissociation reactions used in Chapter 2.

Table A.1: Three body association reactions in the reaction network, which are taken from Willacy et al. (1998). The rate is calculated as $k = \alpha(T/300)^{\beta} \exp(-\gamma/T)$.

Reaction									α	β	γ
CH_3	+	H	+	M	→	CH_4	+	M	9.62(-31)	-1.80	3.23(3)
C	+	O	+	M	→	CO	+	M	2.14(-29)	-3.08	2.11(3)
CO	+	O	+	M	→	CO_2	+	M	9.56(-34)	0.00	1.06(3)
H	+	CO	+	M	→	HCO	+	M	5.30(-34)	0.00	3.70(2)
N	+	N	+	M	→	N_2	+	M	9.53(-34)	-0.50	0.00(0)
N	+	H	+	M	→	NH	+	M	3.09(-32)	-0.50	0.00(0)
NH	+	H	+	M	→	NH_2	+	M	3.18(-33)	-0.50	0.00(0)
NH_2	+	H	+	M	→	NH_3	+	M	1.32(-33)	0.00	4.37(3)
N	+	O	+	M	→	NO	+	M	3.86(-34)	0.00	2.57(3)
O	+	O	+	M	→	O_2	+	M	5.25(-35)	0.00	9.02(2)
O	+	H	+	M	→	OH	+	M	6.32(-34)	0.00	1.96(3)
OH	+	H	+	M	→	H_2O	+	M	6.86(-31)	-2.00	0.00(0)
S	+	S	+	M	→	S_2	+	M	2.76(-33)	-0.50	0.00(0)
SO	+	O	+	M	→	SO_2	+	M	1.86(-31)	-0.50	0.00(0)
H	+	H	+	H_2	→	H_2	+	H_2	8.72(-33)	-0.60	0.00(0)
H	+	H	+	H	→	H_2	+	H	1.83(-31)	-1.00	0.00(0)

Table A.2: Collisional dissociation reactions in the reaction network. The rate is calculated as $k = \alpha(T/300)^{\beta}\exp(-\gamma/T)$. At the end of the row, W and H indicate that the rate is taken from Willacy et al. (1998) and Harada et al. (2010), respectively. WE also refers Willacy et al., but γ is replaced by the difference between the formation enthalpy of the products and the reactants at 300 K. E indicates that the rate is estimated. The rates of the collisional dissociation reactions, which are not listed here, are calculated as $k = 10^{-10}\exp(-50000/T)$.

Reaction									α	β	γ	Reference
C_2	+	M	→	C	+	C	+	M	6.17(-10)	0.00	7.17(4)	WE
C_3	+	M	→	C_2	+	C	+	M	6.17(-10)	0.00	8.83(4)	WE
C_4	+	M	→	C_3	+	C	+	M	1.00(-10)	0.00	6.81(4)	E
C_5	+	M	→	C_4	+	C	+	M	1.00(-10)	0.00	8.52(4)	E
CH	+	M	→	C	+	H	+	M	3.16(-10)	0.00	4.10(4)	WE
CH_2	+	M	→	CH	+	H	+	M	6.64(-9)	0.00	5.12(4)	WE
CH_2	+	M	→	C	+	H_2	+	M	2.16(-10)	0.00	3.97(4)	WE
CH_3	+	M	→	CH	+	H_2	+	M	1.15(-9)	0.00	5.40(4)	WE
CH_3	+	M	→	CH_2	+	H	+	M	1.70(-8)	0.00	5.52(4)	WE
CH_4	+	M	→	CH_3	+	H	+	M	1.20(-6)	0.00	5.28(4)	WE
C_2H	+	M	→	C_2	+	H	+	M	3.74(-10)	0.00	6.96(4)	WE
C_2H_2	+	M	→	C_2	+	H_2	+	M	7.59(-17)	0.00	7.35(4)	WE
C_2H_2	+	M	→	C_2H	+	H	+	M	6.97(-8)	0.00	5.63(4)	WE
C_2H_3	+	M	→	C_2H_2	+	H	+	M	5.07(-20)	-7.50	2.29(4)	W
C_2H_4	+	M	→	C_2H_3	+	H	+	M	1.00(-10)	0.00	5.59(4)	E
C_2H_5	+	M	→	C_2H_4	+	H	+	M	1.00(-10)	0.00	1.67(4)	E
C_3H_4	+	M	→	C_3H_3	+	H	+	M	1.66(-7)	0.00	4.47(4)	WE
C_4H_2	+	M	→	C_4H	+	H	+	M	5.91(-7)	0.00	4.03(4)	W
CO	+	M	→	C	+	O	+	M	1.93(-6)	0.00	1.29(5)	WE
CO_2	+	M	→	CO	+	O	+	M	8.01(-11)	0.00	6.40(4)	WE
HCO	+	M	→	CO	+	H	+	M	2.39(-10)	0.00	8.13(3)	W
H_2CO	+	M	→	HCO	+	H	+	M	2.10(-8)	0.00	4.54(4)	WE
H_2CO	+	M	→	H_2	+	CO	+	M	3.95(-9)	0.00	1.75(4)	W
C_2O	+	M	→	C	+	CO	+	M	1.00(-10)	0.00	3.84(4)	E
CS	+	M	→	C	+	S	+	M	1.00(-10)	0.00	8.58(4)	E
HCS	+	M	→	CS	+	H	+	M	1.00(-10)	0.00	2.39(4)	E
H_2CS	+	M	→	HCS	+	H	+	M	1.00(-10)	0.00	4.85(4)	E
CN	+	M	→	C	+	N	+	M	3.32(-10)	0.00	9.07(4)	WE
HCN	+	M	→	CN	+	H	+	M	2.08(-8)	0.00	6.23(4)	WE
HNC	+	M	→	CN	+	H	+	M	1.00(-10)	0.00	5.52(4)	E
HNCO	+	M	→	NH	+	CO	+	M	1.00(-10)	0.00	4.42(4)	E
C_2N	+	M	→	C	+	CN	+	M	1.00(-10)	0.00	7.16(4)	E
S_2	+	M	→	S	+	S	+	M	7.95(-11)	0.00	5.12(4)	WE
HS	+	M	→	H	+	S	+	M	1.00(-10)	0.00	4.28(4)	E
H_2S	+	M	→	HS	+	H	+	M	7.70(-10)	0.00	4.55(4)	WE
SO	+	M	→	S	+	O	+	M	6.61(-10)	0.00	6.27(4)	WE
SO_2	+	M	→	SO	+	O	+	M	6.60(-9)	0.00	6.63(4)	WE
H_2S_2	+	M	→	H_2S	+	S	+	M	1.00(-10)	0.00	2.90(4)	E

Table A.2: continue

Reaction									α	β	γ	Reference
N_2	+	M	→	N	+	N	+	M	9.21(-5)	-2.50	1.14(5)	WE
NH	+	M	→	N	+	H	+	M	4.40(-10)	0.00	3.80(4)	W
NH_2	+	M	→	NH	+	H	+	M	1.00(-36)	0.50	4.91(4)	WE
NH_3	+	M	→	NH_2	+	H	+	M	3.46(-8)	0.00	5.42(4)	WE
NH_3	+	M	→	NH	+	H_2	+	M	1.05(-9)	0.00	5.08(4)	WE
NS	+	M	→	N	+	S	+	M	1.00(-10)	0.00	5.85(4)	E
NO	+	M	→	N	+	O	+	M	4.10(-9)	0.00	7.60(4)	WE
HNO	+	M	→	H	+	NO	+	M	1.00(-10)	0.00	2.36(4)	E
N_2O	+	M	→	N	+	NO	+	M	1.00(-10)	0.00	5.79(4)	E
SiH	+	M	→	Si	+	H	+	M	1.00(-10)	0.00	3.51(4)	E
SiH_2	+	M	→	SiH	+	H	+	M	7.60(-8)	-1.80	3.87(4)	WE
SiH_2	+	M	→	Si	+	H_2	+	M	7.60(-8)	-1.76	2.13(4)	WE
SiH_3	+	M	→	SiH	+	H_2	+	M	4.98(-10)	0.00	2.12(4)	WE
SiH_4	+	M	→	SiH_3	+	H	+	M	5.00(-11)	0.00	4.62(4)	WE
SiH_4	+	M	→	SiH_2	+	H_2	+	M	5.00(-11)	0.00	2.90(4)	WE
SiC	+	M	→	Si	+	C	+	M	1.00(-10)	0.00	5.38(4)	E
SiS	+	M	→	Si	+	S	+	M	1.00(-10)	0.00	7.47(4)	E
SiN	+	M	→	Si	+	N	+	M	1.00(-10)	0.00	6.62(4)	E
SiO	+	M	→	Si	+	O	+	M	1.00(-10)	0.00	9.62(4)	E
SiO_2	+	M	→	SIO	+	O	+	M	1.00(-10)	0.00	5.46(4)	E
SiC_2	+	M	→	SiC	+	C	+	M	1.00(-10)	0.00	9.95(4)	E
OH	+	M	→	O	+	H	+	M	4.00(-9)	0.00	5.15(4)	WE
H_2O	+	M	→	OH	+	H	+	M	5.80(-9)	0.00	6.00(4)	WE
OCS	+	M	→	CO	+	S	+	M	4.82(-10)	0.00	3.71(4)	WE
HCl	+	M	→	H	+	CL	+	M	1.00(-10)	0.00	5.19(4)	E
CCl	+	M	→	C	+	Cl	+	M	1.00(-10)	0.00	4.04(4)	E
ClO	+	M	→	Cl	+	O	+	M	1.00(-10)	0.00	3.24(4)	E
CP	+	M	→	C	+	P	+	M	1.00(-10)	0.00	7.02(4)	E
HCP	+	M	→	H	+	CP	+	M	1.00(-10)	0.00	6.23(4)	E
CH_2PH	+	M	→	CH_2	+	PH	+	M	1.00(-10)	0.00	1.11(5)	E
MgH	+	M	→	Mg	+	H	+	M	1.00(-10)	0.00	2.36(4)	E
NaH	+	M	→	Na	+	H	+	M	1.00(-10)	0.00	2.42(4)	E
PH	+	M	→	P	+	H	+	M	1.00(-10)	0.00	3.38(4)	E
PH_2	+	M	→	PH	+	H	+	M	1.00(-10)	0.00	4.13(4)	E
PN	+	M	→	P	+	N	+	M	1.00(-10)	0.00	8.23(4)	E
PO	+	M	→	P	+	O	+	M	1.00(-10)	0.00	7.09(4)	E
HPO	+	M	→	H	+	PO	+	M	1.00(-10)	0.00	3.02(4)	E
O_2	+	M	→	O	+	O	+	M	5.16(-10)	0.00	6.00(4)	WE
O_2H	+	M	→	O_2	+	H	+	M	1.00(-10)	0.00	2.47(4)	E
H_2O_2	+	M	→	H_2O	+	O	+	M	1.00(-10)	0.00	1.73(4)	E
O_3	+	M	→	O_2	+	O	+	M	1.00(-10)	0.00	1.28(4)	E
CH_3N	+	M	→	CH_3	+	N	+	M	1.00(-10)	0.00	6.34(4)	E
CH_3NH_2	+	M	→	CH_3	+	NH_2	+	M	1.00(-10)	0.00	4.26(4)	E
CH_2CN	+	M	→	C_2N	+	H_2	+	M	1.00(-10)	0.00	6.00(4)	E
CH_3CN	+	M	→	CH_3	+	CN	+	M	1.00(-10)	0.00	6.21(4)	E
HCOOH	+	M	→	HCO	+	OH	+	M	1.00(-10)	0.00	5.55(4)	E

Table A.2: continue

Reaction									α	β	γ	Reference
CH_2CO	+	M	→	CH_2	+	CO	+	M	5.97(-9)	0.00	3.86(4)	WE
CH_3OH	+	M	→	CH_3	+	OH	+	M	3.32(-7)	0.00	4.64(4)	WE
CH_3CHO	+	M	→	CH_3	+	HCO	+	M	1.00(-10)	0.00	4.20(4)	E
H_2	+	e^-	→	H	+	H	+	e^-	2.00(-9)	0.50	1.20(5)	H
H_2	+	H	→	H	+	H	+	H	1.00(-10)	0.00	5.20(4)	H
H_2	+	He	→	H	+	H	+	He	1.00(-11)	0.00	5.20(4)	H
H_2	+	H_2	→	H	+	H	+	H_2	1.30(-11)	0.00	5.20(4)	H

Appendix B

Column density profiles of gaseous methanol in protoplanetary disks

In this appendix, we give analytical expressions of the column density profile of gaseous CH_3OH in protoplanetary disks, which reasonably reproduce our numerical results both in the model with $\alpha_z = 0$ and 10^{-2} as shown in Figure 4.8. We focus on CH_3OH, since no efficient formation pathway is known for CH_3OH in the gas phase. However, the following description can be easily extended and applied to other molecules.

In the model without mixing, CH_3OH ice predominantly exists near the midplane (Figure 4.2). In that case, the number density of gaseous CH_3OH near the midplane is evaluated from the balance between the photodesorption by cosmic-ray induced photons and adsorption onto dust grains:

$$n^{\rm g}_{\rm CH_3OH} = 10^{-4} \left(\frac{n^{\rm s}_{\rm CH_3OH}/n_{\rm ice}}{0.1} \right) \left(\frac{F_{\rm CRUV}}{10^4\,{\rm cm^2\,s^{-1}}} \right) \left(\frac{Y}{10^{-3}} \right) \left(\frac{v_{\rm th}}{10^4\,{\rm cm\,s^{-1}}} \right)^{-1}, \quad \text{(B.1)}$$

where $v_{\rm th}$ is the thermal velocity of methanol. The number density of gaseous CH_3OH is independent of the number density of gas. Since CH_3OH ice is abundant only at $z/r \lesssim 0.3$ in the model without mixing, the radial column density profile of gaseous CH_3OH is evaluated by

$$N^{\rm g}_i \approx n^{\rm g}_{\rm CH_3OH} \times 0.3r \quad \text{(B.2)}$$

$$\approx 10^{11} \left(\frac{n^{\rm s}_{\rm CH_3OH}/n_{\rm ice}}{0.1} \right) \left(\frac{F_{\rm CRUV}}{10^4\,{\rm cm^2\,s^{-1}}} \right) \left(\frac{Y}{10^{-3}} \right) \quad \text{(B.3)}$$

$$\times \left(\frac{v_{\rm th}}{10^4\,{\rm cm\,s^{-1}}} \right)^{-1} \left(\frac{r}{300\,{\rm AU}} \right) \left(\frac{z/r}{0.3} \right)\ {\rm cm^{-2}}. \quad \text{(B.4)}$$

Equation (B.4) shows that the column density is proportional to radius. The radial

dependence can be steeper, if $n^{\rm s}_{\rm CH_3OH}/n_{\rm ice}$ increases with radius. The dot-dashed line in Figure 4.8 shows the analytical value with $n^{s}_{\rm CH_3OH}/n_{\rm ice}$ adopted from our numerical model.

On the other hand, in the model with mixing, CH_3OH ice exists even in the disk surface. As an extreme case, let us assume that CH_3OH ice exits in the whole disk, and photodissociation is the main destruction path of gaseous CH_3OH in the disk surface. As mentioned in Section 4.3.3, the latter assumption is not valid at $r \gtrsim 200$ AU in our model. But errors introduced by the latter assumption is not so large as seen in Figure 4.8. Considering Equation (4.13), the radial column density profile of gaseous CH_3OH is evaluated by $N^{\rm g}_{\rm CH_3OH} \approx x^{\rm g}_{\rm CH_3OH} \times N^{\rm crit}_{\rm H}$, where $N^{\rm crit}_{\rm H}$ is the column density of hydrogen nuclei measured from the disk surface to the height ($\sim 4 \times 10^{21}$ $\rm cm^{-2}$ in our model), below which ion-neutral reactions or adsorption onto dust grains becomes dominant destruction path of gaseous CH_3OH instead of photodissociation:

$$N^{\rm g}_{\rm CH_3OH} \approx 2 \times 10^{13} \left(\frac{n^{\rm s}_{\rm CH_3OH}/n_{\rm ice}}{0.1} \right) \left(\frac{\pi a^2 x_d N^{\rm crit}_{\rm H}}{2} \right) \left(\frac{Y}{10^{-3}} \right) \left(\frac{\sigma_{{\rm Ly}\alpha}}{10^{-17}\,{\rm cm}^2} \right)^{-1} \ {\rm cm}^{-2}. \tag{B.5}$$

Equation (B.5) shows that the column density is dependent on radius only through $n^{\rm s}_{\rm CH_3OH}/n_{\rm ice}$. Then the radial profile in the model with mixing is flattened compared to that in the model without mixing. Equations (B.4) and (B.5) also explain the order-of-magnitude enhancement of the column density via the vertical ice transport.

Acknowledgement

First of all, I wish to thank my supervisor, Prof. Yuri Aikawa, for a lot of helpful advice and fruitful discussions during my postgraduate study. I would also like to thank my collaborators, Prof. Tomoaki Matsumoto, Prof. Kohji Tomisaka, Prof. Satoshi Yamamoto, Prof. Hideko Nomura, Dr. Franck Hersant, Dr. Kazuya Saigo, Dr. Nami Sakai, Dr. Kengo Tomida, and Dr. Valentine Wakelam for their help. I also thank Prof. Yoshitsugu Nakagawa, Prof. Keiji Ohtsuki and other members of Planetary Astrophysics Group at Kobe University for their discussion.

Numerical computations presented in Chapter 2 were partly carried out on NEC SX-9 at the Japan Aerospace Exploration Agency (JAXA) and at the Center for Computational Astrophysics (CfCA) of the National Astronomical Observatory of Japan. I greatly appreciate the Research Fellowship from the Japan Society for the Promotion of Science (JSPS) for Young Scientists.

Bibliography

Ádámkovics, M., Glassgold, A. E., & Meijerink, R. 2011, ApJ, 736, 143

Agúndez, M., Cernicharo, J., Guélin, M., Gerin, M., McCarthy, M. C., & Thaddeus, P. 2008, A&A, 478, L19

Agúndez, M., Goicoechea, J. R., Cernicharo, J., et al. 2010, ApJ, 713, 662

Aikawa, Y 2007, ApJL, 656, L93

Aikawa, Y., & Herbst, E., 1999, ApJ, 526, 314

Aikawa, Y., & Herbst, E., 2001, A&A, 371, 1107

Aikawa, Y., Miyama, S. M., Nakano, T., & Umebayashi, T. 1996, ApJ, 467, 684

Aikawa, Y., Umebayashi, T., Nakano, T., & Miyama, S. M. 1997, ApJL, 486, L51

Aikawa, Y., van Zadelhoff, G. J., van Dishoeck, E. F., & Herbst, E. 2002, A&A, 386, 622

Aikawa, Y., Wakelam, V., Garrod, R. T., & Herbst, E. 2008, ApJ, 674, 984

Aikawa, Y., Wakelam, V., Hersant, F., Garrod, R., & Herbst, E. 2012, ApJ, 760, 40

Alves, J. F., Lada, C. J., & Lada, E. A. 2001, Nature, 409, 159

Al-Halabi, A., & van Dishoeck, E. F. 2007, MNRAS, 382, 1648

Andersson, S., Al Halabi, A., Kroes, G.-J., & van Dishoeck, E. F. 2006, J. Chem. Phys., 124, 4715

Andersson, S., & van Dishoeck, E. F. 2008, A&A, 491, 907

André, P., Di Francesco, J., Ward-Thompson, D., Inutsuka, S., Pudritz, R. E., Pineda, J. 2013, arXiv:1312.6232

Balbus, S. A., & Hawley, J. F. 1991, ApJ, 376, 214

Bate, M. R., 2010, MNRAS, 404, L79

Bate, M. R., 2011, MNRAS, 417, 2036

Bate, M. R., Tricco, T. S., & Price, D. J. 2014, MNRAS, 437, 77

Bergin, E. A., Aikawa, Y., Blake, G. A., & van Dishoeck, E. F. 2007, in Protostars and Planets V, ed. B. Reipurth, D. Jewitt, & K. Keil (Tuscon, AZ: Univ. Arizona Press), 751

Bergin, E. A., Neufeld, D. A., & Melnick, G. J., 1999, ApJ, 510, L145

Bethell, T. J., & Bergin, E. A. 2011, ApJ, 739, 78

Biver, N., Crovisier, J., Bockelée-Morvan, D., et al. 2012, A&A, 539, 68

Black, J. H., & Dalgarno, A. 1976, ApJ, 203, 132

Bockelée-Morvan, D., Biver, N., Swinyard, B., et al. 2012, A&A, 544, L15

Bohlin, R. C., Savage, B. D, & Drake, J. F. 1978, ApJ, 224, 132

Boogert, A. C. A., Pontoppidan, K. M., Knez, C., et al. 2008, ApJ, 678, 985

Bottinelli, S., et al. 2004. ApJ, 615, 354

Brownlee, D. E. 2003, In Meteorites, Comets, and Planets (ed. Davis, A. M.), Elsevier-Pergamon, Oxford

Brünken, S., Gupta, H., Gottlieb, C. A., McCarthy, M. C., & Thaddeus, P. 2007, ApJ, 664, L43

Cardelli, J. A., Clayton, G. C., & Mathis. J. S. 1989, ApJ, 345, 245

Carr, J. S., & Najita, J. R. 2008, Science, 319, 1504

Caselli, P., Hasegawa, T. I., & Herbst, E. 1998, ApJ, 495, 309

Caselli, P., & Ceccarelli, C. 2012, ARAA, 20, 56

Caselli, P., Keto, E., Bergin, E. A., et al. 2012, ApJL, 759, L37

Caselli, P., Stantcheva, T., Shalabia, O., Shematovich, V. I., & Herbst, E. 2002, Planet. Space Sci., 50, 1257

Cazaux, S., et al. 2003, ApJ, 593, L51

Cazaux, S., Caselli, P., Cobut, V., & Le Bourlot, J. 2008, A&A, 483, 495

Cazaux, S., & Tielens, A. G. G. M. 2004, ApJ, 604, 222

Cazaux, S., & Tielens, A. G. G. M. 2010, ApJ, 715, 698

Ceccarelli, C., Castets, A., Caux, E., et al. 2000, A&A, 355, 1129

Ceccarelli, C., & Dominik, C. 2005, A&A, 440, 583

Ceccarelli, C., Dominik, C., Caux, E., Lefloch, B., & Caselli, P. 2005, ApJ, 631, L81

Chandler, C. J., Brogan, C. L., Shirley, Y. L., & Loinard, L. 2005, ApJ, 632, 371

Charnley, S. B., Tielens, A. G. G. M., & Millar, T. J. 1992, ApJ, 399, L71

Chen, X., Arce, H. G., Zhang, Q., Bourke, T. L., Launhardt, R., Schmalzl, M., & Henning, T. 2010, ApJ, 715, 1344

Ciesla, F. J., & Sandford, S. A. 2012, Science, 336, 452

Codella, C., Ceccarelli, C., Lefloch, B., et al. 2012, ApJ, 757, L9

Collings, M. P., Anderson, M. A., Chen, R., et al. 2004, MNRAS, 354, 1133

Commerçon, B., Audit, E., Chabrier, G., & Chièze, J. -P. 2011, A&A, 530, 13

Commerçon, B., Hennebelle, P., Audit, E., Chabrier, G., & Teyssier, R. 2010, A&A, 510, L3

Coutens, A., Vastel, C., & Caux, E., et al. 2012, A&A, 539, 132

Crimier, N., et al. 2010, A&A, 519, 65

Cuppen, H. M., van Dishoeck, E. F., Herbst, E., & Tielens, A. G. G. M. 2009, A&A, 508, 275

Dalgarno, A. 2006, Proc. Natl Acad. Sci., 103, 12269

Dalgarno, A., Yan, M., & Weihong, L. 1999, ApJS, 125, 237

Dominik, C., Ceccarelli, C., Hollenbach, D., & Kaufman, M. J. 2005, ApJ, 635, L85

Draine, B. T. 1978, ApJS, 36, 595

Draine, B. T., & Bertoldi, F. 1996, ApJ, 468, 269

Draine, B. T., & Sutin, B., 1987, ApJ, 320, 803

Drouart, A., Dubrulle, B., Gautier, D., Robert, F. 1999, Icarus, 140, 129

Dunham, M, M., Chen, X., Arce, H. G., Bourke, T. L., Schnee, S., & Enoch, M, L. 2011, ApJ, 742, 1

Dutrey, A., Guilloteau, S., & Guélin, M. 1997, A&A, 317, L55

Enoch, M. L., Lee, J., Harvey, P., Dunham, M. M., & Schnee, S. 2010, ApJ, 722, L33

Favre, C., Cleeves, L. I., Bergin, E. A., Qi, C., & Blake, G. A. 2013, ApJL, 776, L38

Fayolle, E. C., Bertin, M., Romanzin, C., et al. 2011, ApJ, 739, L36

Fayolle, E. C., Bertin, M., Romanzin, C., et al. 2013, A&A, 556, 122

Field, G. B., Goldsmith, D. W., & Habing, H. J. 1969, ApJL, 155, 149L

Fleming, T. P., Stone, J. M., & Hawley, J. F. 2000, ApJ, 530, 464

Fromang, S., & Papaloizou, J. 2006, A&A, 452, 751

Fuchs, G. W., Cuppen, H. M., Ioppolo, S., et al. 2009, A&A, 505, 629

Furlan, E., Hartmann, L., Calvet, N., et al. 2006, ApJS, 165, 568

Furlan, E., Luhman, K. L., Espaillat, C., et al. 2011, ApJS, 195, 3

Furuya, K., Aikawa, Y., Tomida, K., et al. 2012, ApJ, 758, 869

Furuya, K., Aikawa, Y., Nomura, H., Hersant, F., & Wakelam, V. 2013, ApJ, 779, 11

Gammie, C. F. 1996, ApJ, 457, 355

Garrod, R. T. 2013, ApJ, 765, 60

Garrod, R. T. 2008, A&A, 491, 239

Garrod, R. T., & Herbst, E. 2006, A&A, 457, 927

Garrod, R. T., Vasyunin, A. I., Semenov, D. A., Wiebe, D. S., & Henning, Th. 2009, ApJ, 700, L43

Garrod, R. T., Wakelam, V., & Herbst, E. 2007, A&A, 467, 1103

Garrod, R. T., Weaver, S. L. W., & Herbst, E. 2008, ApJ, 682, 283

Geppert, W. D., et al. 2006, Faraday Discuss. 133, Chemical Evolution of the Universe (Cambridge: RSC Pub.), 177

Gerakines, P, A., Schutte, W. A., & Ehrenfreund, P. 1996, A&A, 312, 289

Glassgold, A. E., Meijerink, R., & Najita, J. R. 2009, ApJ, 701, 142

Gomes, R., Levison, H. F., Tsiganis, K., & Morbidelli, A. 2005. Nature, 435, 466

Goodman, A. A., Benson, P. J., Fuller, G. A., & Myers, P. C. 1993, ApJ, 406, 528

Graedel, T. E., Langer, W. D., & Frerking, M. A. 1982, ApJS, 48, 321

Gredel, R., Lepp, S., Dalgrano, A., & Herbst, E. 1989, ApJ, 347, 289

Gressel, O., Nelson, R. P., & Turner, N. J. 2012, MNRAS, 422, 1240

Guilloteau, S., Di Folco, E., Dutrey, A., Simon, M., Grosso, N., & Piétu, V. 2013, A&A, 549, 92

Guilloteau, S., Pietu, V., Dutrey, A., & Guelin, M. 2006, A&A, 448, L5

Hama, T., Kuwahata, K., Watanabe, N., et al. 2012, ApJ, 757, 185

Hamberg, M., et al. 2010, A&A, 514, 83

Harada, N., Herbst, R., & Wakelam, V. 2010, ApJ, 721, 1570

Hartogh, P., Lis, D. C, Bockelée-Morvan, D., et al. 2011, Nature, 478, 218

Hasegawa, T. I., & Herbst, E. 1993, MNRAS, 261, 83

Hasegawa, T. I., Herbst, E., & Leung, C. M. 1992, ApJS, 82, 167

Hashimoto, J., Dong, R., Kudo, T., et al. 2012, ApJL, 758, L19

Hassel, G. E., Herbst, E., & Garrod, R. T. 2008, ApJ, 681, 1385

Heinzeller, D., Nomura, H., Walsh, C., & Millar, T. J. 2011, ApJ, 731, 115

Herbst, E. & Klemperer, W. 1973, ApJ, 185, 505

Herbst, E, & van Dishoeck, E. F. 2009, ARAA, 47, 427

Herczeg, G. J., Linsky, J. L., Valenti, J. A., Johns-Krull, C. M., & Wood, B. E. 2002, ApJ, 572, 310

Herczeg, G. J., Wood, B. E., Linsky, J. L., Valenti, J. A., & Johns-Krull, C. M. 2004, ApJ, 607, 369

Hersant, F., Gautier, D., & Huré, J.-M. 2001, ApJ, 554, 391

Hersant, F., Wakelam, V., Dutrey, A., Guilloteau, S., & Herbst, E. 2009, A&A, 493, L49

Herbst, E, & van Dishoeck, E. F. 2009, ARAA, 47, 427

Hildebrand, R. H. 1983, QJRAS, 24, 267

Hincelin, U., Wakelam, V., Commerçon, B., Hersant, F., & Guilloteau, S. 2013, ApJ, 775, 44

Hincelin, U., Wakelam, V., Hersant, F., et al. 2011, A&A, 530, A61

Hogerheijde, M. R., Bergin, E. A., Brinch, C., et al. 2011, Science, 334, 338

Hollenbach, D., Kaufman, M. J., Bergin, E. A., & Melnick, G. J. 2009, ApJ, 690, 1497

Hollenbach, D., & McKee, C. F. 1979, ApJS, 41, 555

Hollenbach, D., & Salpeter, E. E. 1971, ApJ, 163, 155

Honda, M., Inoue, A. K., Fukagawa, M., et al. ApJ, 690, L110

Inutsuka, S., & Sano, T. 2005, ApJ, 628, L155

Ioppolo, S., Cuppen, H. M., Romanzin, C., van Dishoeck, E. F., & Linnartz, H. 2008, ApJ, 686, 1474

Jansen, D. J., Spaans, M., Hogerheijde, M. R., & van Dishoeck, E. F. 1995a, A&A, 303, 541

Jansen, D. J., van Dishoeck, E. F., Black, J. H., Spaans, M., & Sosin, C. 1995b, A&A, 302, 223

Jensen, M. J., Bilodeau, R. C., Safvan, C. P., et al. 2000, ApJ, 543, 764

Jørgensen, J. K., & van Dishoeck, E. F. 2010, ApJ, 725, L172

Kastner, J. H., Huenemoerder, D. P., Schulz, N. S., Canizares, C. R., & Weintraub, D. A. 2002, ApJ, 567, 434

Kawakita, H., & Mumma, M. J. 2011, ApJ, 727, 91

Kenyon, S. J., & Hartmann, L. 1995, ApJS, 101, 117

Kuan, Y.-J., et al. 2004, ApJ, 616, L27

Laas, J., Garrod, R. T., Herbst, E., & Widicus-Weaver, S. 2011, ApJ, 728, 71

Langer, W. D., & Penzias, A. A. 1993, ApJ, 408, 539

Larson, R. B., 1969, MNRAS, 145, 271

Lécluse C. & Robert F. 1994, Geochimica et Cosmochimica Acta, 58, 2297

Lee, H.-H., Herbst, E., Pineau des Forêts, G., Roueff, E., & Le Bourlot, J. 1996, A&A, 311, 690

Lennon, M. A., Bell, K. L., Gilbody, H. B., et al. 1988, J. Phys. Chem. Reference Data, 17, 1285

Levermore, C. D., & Pomraning, G. C. 1981, ApJ, 248, 321

Linsky, J. L. 2003, Space Sci. Rev., 106, 49

Lis, D.C., Biver, N., Bockelée-Morvan, D., et al. 2013, arXiv:1307.6869

Liu, F.-C., Parise, B., Kristensen, L., Visser, R., van Dishoeck, E. F., & Güsten, R, 2011, A&A, 527, 19

London, R. 1978, ApJ, 225, 405

Lucas, R., & Liszt, H. 1998, A&A, 337, 246

Machida, M. N., Inutsuka, S., & Matsumoto, T. 2008, ApJ, 676, 1088

Machida, M. N., Inutsuka, S., & Matsumoto, T. 2010, ApJ, 724, 1006

Machida, M. N., & Matsumoto, T. 2011, MNRAS, 413, 2767

Maloney, P. R., Hollenbach, D. J., & Tielens, A. G. G. M. 1996, ApJ, 466, 561

Maret, S., et al. 2005, A&A, 442, 527

Mason, N. J., Dawes, A, Holtom, P. D., et al. 2006, Faraday Discuss., 133, 311

Masunaga, H., & Inutsuka, S. 2000, ApJ, 531, 350

Masunaga, H., Miyama, S. M., & Inutsuka, S. 1998, ApJ, 495, 346

Matsumoto, T., & Hanawa, T. 2003, ApJ, 595, 913

McKee, C. F. & Ostriker, J. P. 1977, ApJ, 218, 148

Meijerink, R., Aresu, G., Kamp, I., Spaans, M., Thi, W.-F., & Woitke, P. 2012, A&A, 547, 68

Meijerink, R., Cazaux, S., & Spaans, M. 2012, A&A, 537, 102

Meijerink, R., & Spaans, M. 2005, A&A, 436, 397

Millar, T. J., Herbst, E., & Herbst, E. 1989, ApJ, 340, 906

Miyauchi, N., Hidaka, H., Chigai, T., et al. 2008, Chem. Phys. Lett., 456, 27

Mumma, M. J., & Charnley, S. B. 2011, ARAA, 49, 471

Noble, J., Dulieu, F., Congui, E., & Fraser, H. J. 2011, ApJ, 735, 121

Nomura, H., Aikawa,Y., Tsujimoto, M., Nakagawa,Y., & Millar, T. J. 2007, ApJ, 661, 334

Nomura, H., & Millar, T. J. 2005, A&A, 438, 923

Nomura, H., Aikawa, Y., Nakagawa, Y., & Millar, T. J. 2009, A&A, 495, 183

Nummelin, A., Bergman, P., Hjalmarson, A., et al. 2000, ApJS, 128, 213

Oba, Y., Watanabe, N., Hama, T., Kuwahata, K., Hidaka, H., & Kouchi, A. 2012 ApJ, 749, 67

Oba, Y., Watanabe, N., Kouchi, A., Hama, T., & Pirronello, V. 2010, ApJL, 712, L174

Öberg, K. I., Boogert, A. C. A., Pontoppidan, K. M., et al. 2011, ApJ, 740, 109

Öberg, K. I., Fuchs, G. W., Awad, Z., et al. 2007, ApJ, 662, L23

Öberg, K. I., Linnartz, H., Visser, R., & van Dishoeck, E. F. 2009a, ApJ, 693, 1209

Öberg, K. I., van Dishoeck, E. F., & Linnartz, H. 2009b, A&A, 496, 281

Öberg, K. I., Garrod, R. T., van Dishoeck, E. F., & Linnartz, H. 2009c, A&A, 504, 891

Öberg, K. I., Qi, C., Fogel, J. K. J., et al. 2010, ApJ, 720, 480

Okuzumi, S., & Hirose, S. 2011, ApJ, 742, 65

Omukai K., 2007, PASJ, 59, 589

Onishi, T., Mizuno, A., Kawamura, A., et al. 2002, ApJ, 575, 950

Ootsubo, T., Kawakita, H., Hamada, S., et al. 2012, ApJ, 752, 15

Palmeirim, P., André, Ph., Kirk, J. et al. 2013, A&A, 550, 38

Pineda, J. E., et al. 2011, ApJ, 743, 201

Prasad, S. S., & Tarafdar, S. P. 1983, ApJ, 267, 603

Perez-Becker, D. & Chiang, E. 2011, ApJ, 727, 2

Persson, M. V., Jørgensen, J. K., & van Dishoeck, E. F. 2013, A&A. 549, L3

Przygodda, F., van Boekel, R., Abraham, P., et al. 2003, A&A, 412, L43

Qi, C., DÁlessio, P., Öberg, K. I., et al. 2011, ApJ, 740, 84

Qi, C., Öberg, K. I., & Wilner, D. J. 2013, ApJ, 765, 34

Ruffle, D. P., & Herbst, E. 2001, MNRAS, 324, 1054

Roberts, H,. Herbst, E., & Millar, T. J. 2004, A&A, 424, 905

Sakai, N., Sakai, T., Hirota, T., Burton, M., & Yamamoto, S. 2009, ApJ, 697, 769

Sakai, N., Sakai, T., Hirota, T., & Yamamoto, S. 2008, ApJ, 672, 371

Sakai, N., Sakai, T., Osamura, Y., & Yamamoto, S. 2007, ApJ, 667, L65

Saigo, K., Tomisaka, K., & Matsumoto, T. 2008, ApJ, 674, 997

Saigo, K., & Tomisaka, K. 2011, ApJ, 728, 78

Sano, T., Miyama, S. M., Umebayashi, T., & Nakano, T. 2000, ApJ, 543, 486

Semenov, D., et al. 2010, A&A, 522, 42

Semenov, D., & Wiebe, D. 2011, ApJS, 196, 25

Semenov, D., Wiebe, D., & Henning, Th. 2004, A&A, 417, 93

Semenov, D., Wiebe, D., & Henning, Th. 2006, ApJL, 647, L57

Shakura, N. I., & Sunyaev, R. A. 1973, A&A, 24, 337

Stäuber, P., Doty, S. D., van Dishoeck, E. F., & Benz, A. O. 2005, A&A, 440, 949

Talukdar, R. K., Gierczak, T., Goldfarb, L., Rudich, Y., Madhava Rao, & B. S., Ravishankara, A. R. 1996, J. Phys. Chem., 100, 3037

Taquet, V., López-Sepulcre, A., Ceccarelli, C., Neri, R., Kahane, C., Coutens, A., & Vastel, C. 2013, ApJ, 768, L29

Taquet, V., Peters, P. S., Kahane, C., Ceccarelli, C., et al, 2013, A&A, 550, 127

Terada, H., Tokunaga, A. T., Kobayashi, N., et al. 2007, ApJ, 667, 303

Tielens, A. G. G. M. 2005, The Physics and Chemistry of the Interstellar Medium (Cambridge: Cambridge Univ. Press), 219

Tielens, A. G. G. M., & Hagen, W. 1982, A&A, 114, 245

Tielens, A. G. G. M., & Hollenbach, D. 1985, ApJ, 291, 747

Tobin, J. J. Hartmann, L. Chiang, H.-F. Wilner, D. J. Looney, L. W. Loinard, L. Calvet, N. DÁlessio, P. 2012, Nature, 492, 83

Tobin, J. J., Hartmann, L., Chiang, H.-F., et al. 2013, ApJ, 771, 48

Tomida, K., Tomisaka, K., Matsumoto, T., Ohsuga, K., Machida, M. N., & Saigo, K. 2010a, ApJ, 714, L58

Tomida, K., Machida, M. N., Saigo, K., Tomisaka, K., & Matsumoto, T. 2010b, ApJ, 725, L239

Tomida, K., Tomisaka, K., Matsumoto, T., et al. 2013, ApJ, 763, 6

Tomisaka, K. 2002, ApJ, 575, 306

Tomisaka, K. & Tomida, K. 2011, PASJ, 63, 1151

Tscharnuter, W. M., & Gail, H.-P. 2007, A&A, 463, 369

Umebayashi, T. 1983, Prog. Theor. Phys., 69, 480

Umebayashi, T., & Nakano, T. 1980, PASJ, 32, 405

Umebayashi, T., & Nakano, T. 1981, PASJ, 33, 617

Umebayashi, T., & Nakano, T. 2009, ApJ, 690, 69

van Dishoeck, E. F. 1988, in Rate Coefficients in Astrochemistry, ed. T. J. Millar & D. A. Williams (Dordrecht: Kluwer), 49

van Dishoeck, E. F., Jonkheid, B., & van Hemert,M. C. 2006, Faraday Discuss., 133, 231

van Zadelhoff, G.-J., Aikawa, Y., Hogerheijde, M. R., & van Dishoeck, E. F. 2003, A&A, 397, 789

Verner, D. A., & Yakovlev, D. G. 1995, A&AS, 109, 125

Villanueva, G. L., Mumma, M. J., Bonev, B. P., et al. 2009, ApJ, 690, L5

Visser, R. 2009, PhD thesis, Leiden Observatory

Visser, R., Doty, S. D., & van Dishoeck, E. F. 2011, A&A, 534, 132

Voit, G. M. 1991, ApJ, 377, 158

Wakelam, V., Herbst, E., Loison, J.-C., et al. 2012, ApJS, 199, 21

Walsh, C, Millar, T. J., & Nomura, H. 2010, ApJ, 722, 1607

Walsh, C, Millar, T. J., Nomura, H., & Aikawa, Y. 2012, ApJ, 747, 114

Walsh, C., Millar, T., Nomura, H. et al. 2014, A&A, in press

Walsh, K. J., Morbidelli, A., Raymond, S. N., O'Brian, D. P., & Mandell, A. M. 2011, Nature, 475, 206

Watanabe, N., Nagaoka, A., Shiraki, T., & Kouchi, A. 2004, ApJ, 616, 638

Watanabe, N., Kimura, Y., Kouchi, A., et al. 2010, ApJ, 714, L233

Watson, W. D., & Salpeter, E. E. 1972, ApJ, 174, 321

Weingartner, J. C., & Draine, B. T. 2001, ApJ, 548, 296

Westley, M. S., Baragiola, R. A., Johnson, R. E., & Baratta, G. A. 1995, Nature, 373, 405

Whitehouse, S. C., & Bate, M. R. 2006, MNRAS, 367, 32

Whittet, D. C. B. 1993, Dust and Chemistry in Astronomy (Bristol and Philadelphia: Institute of Physics Publishing), 9

Willacy, K. 2007, ApJ, 660, 441

Willacy, K., Klahr, H. H., Millar, T. J., & Henning, Th. 1998, A&A, 338, 995

Willacy, K., Langer, W., Allen, M., & Bryden, G. 2006, ApJ, 644, 1202

Willacy, K., & Woods, P. M. 2009, ApJ, 703, 479

Woitke, P., Kamp, I., & Thi, W. 2009, A&A, 501, 383

Woitke, P., Thi, W.-F., Kamp, I., & Hogerheijde, M. R. 2009b, A&A, 501, L5

Wolcott-Green, J., & Haiman, Z. 2011, MNRAS, 412, 2603

Wolfire, M. G., Hollenbach, D., McKee, C. F., Tielens, A. G. G. M., & Bakes, E. L. O. 1995, ApJ, 443, 152

Woodall J., Agúndez M., Markwick-Kemper A. J., & Millar T. J., 2007, A&A, 466, 1197

Xie, T., Allen, M., & Langer, W. D. 1995, ApJ, 440, 674

Yang, L., Ciesla, F. J., & Alexander, C. M. O. 2013, Icarus, 226, 256

Yen, H. -W. Takakuwa, S. Ohashi, N. Ho, P. T. P. 2013, ApJ, 772, 22

Yildiz, U. A., Kristensen, L. E., van Dishoeck, E. F., et al. 2012, A&A, 542, 86

Yorke, H. W., & Bodenheimer, P. 1999, ApJ, 525, 330

Youdin, A. N., & Lithwick, Y. 2007, Icarus, 192, 588

van Weeren, R. J., Brinch, C., & Hogerheijde, M. R. 2009, A&A, 497, 773

Visser, R., Doty, S. D., & van Dishoeck, E. F. 2011, A&A, 534, 132

Visser, R., van Dishoeck, E. F., Doty, S. D., & Dullemond, C. P. 2009, A&A, 495, 881

Wakelam, V., et al. 2012, ApJS, 199, 21